First Principles Investigations of Novel Condensed Matter Materials

A dissertation submitted to the
College of Graduate and Postdoctoral Studies
in partial fulfillment of the requirements
for the degree of Doctor of Philosophy
in the Department of Physics and Engineering Physics
University of Saskatchewan
Saskatoon

By
Adebayo O. Adeniyi

Permission to Use

In presenting this dissertation in partial fulfillment of the requirements for a Postgraduate degree from the University of Saskatchewan, I agree that the Libraries of this University may make it freely available for inspection. I further agree that permission for copying of this dissertation in any manner, in whole or in part, for scholarly purposes may be granted by the professor or professors who supervised my dissertation work or, in their absence, by the Head of the Department or the Dean of the College in which my dissertation work was done. It is understood that any copying or publication or use of this dissertation or parts thereof for financial gain shall not be allowed without my written permission. It is also understood that due recognition shall be given to me and to the University of Saskatchewan in any scholarly use which may be made of any material in my dissertation.

Disclaimer

Reference in this dissertation to any specific commercial products, process, or service by trade name, trademark, manufacturer, or otherwise, does not constitute or imply its endorsement, recommendation, or favoring by the University of Saskatchewan. The views and opinions of the author expressed herein do not state or reflect those of the University of Saskatchewan, and shall not be used for advertising or product endorsement purposes.

Requests for permission to copy or to make other uses of materials in this dissertation in whole or part should be addressed to:

Head of the Department of Physics and Engineering Physics
116 Science Place
University of Saskatchewan
Saskatoon,Saskatchewan S7N 5E2
Canada
OR
Dean College of Graduate and Postdoctoral Studies

University of Saskatchewan
116 Thorvaldson Building, 110 Science Place
Saskatoon, Saskatchewan S7N 5C9
Canada

Abstract

The advent of very fast computing power has led to the positioning of theoretical investigations of condensed matter materials as a core part of research in this area. Often the results of such numerical and computational investigations serve as reliable guide for future experimental exploration of new materials and has led to the discovery of numerous materials. In this thesis, state-of-the-art first principles calculations have been applied to investigate the structural, electronic and dynamical properties of some novel condensed matter materials. The novelty of these compounds stems from the fact that they challenge our previous knowledge of the chemistry of chemical reactions that support the formation and stability of chemical compounds and can therefore expand our frontier of knowledge in the quest for scientific understanding of new atypical compounds in high pressure physics.

In the first project, the long sought post-Cmcm phase of the cadmium telluride is characterized with the application of first principles metadynamics method. It has a monoclinic unit cell and the $P2_1/m$ space group. Enthalpy calculation confirms this phase transition sequence and further predicts a $P2_1/m$ to P4/nmm transition near 68 GPa. Interestingly, the enthalpies of CdTe compounds are found to be higher than the enthalpy sum of its constituents Cd and Te at pressures higher than 34 GPa which is an indication that the compound should decompose above this pressure point. However, dynamical stability revealed in the phonon dispersion relations prevents the decomposition of CdTe at high pressure. This suggests that CdTe becomes a high-enthalpy compound at high pressure.

The second project is directed towards the prediction of stable helium-hydrogen compound. In spite of extensive experimental and theoretical work, a general agreement on the crystal structure and stability of the helium-hydrogen system is lacking. In this study, the possibility of helium forming stable compound with hydrogen is investigated by using first principles structure search method. A stable helium hydrogen compound formed at ambient conditions is found. It belongs to the triclinic P-1 space group, having $He(H_2)_3$ stoichiometry. Topological analysis of electron density at the bond critical points shows there exists a quantifiable

level of bonding interaction between helium and hydrogen in the P-1 structure. At ambient pressure, the compound is characterized and stabilized by interactions with strength typical of van der Waals interaction that increases with pressure. This current results provide a case of weak interaction in a mixed hydrogen-helium system, offering insights for the evolution of interiors of giant planets such as Jupiter and Saturn.

In the final project, a machine learning potential is successfully created for sodium based on the Gaussian process regression method and weighted atom-centered symmetry functions representation of the potential energy surface. Here, sodium potential energy surface is described using different relevant data sets that represent several regions of the potential energy surface with each data set consisting of three element groups which are total energies, interatomic forces, and stress tensors of the cell, which were constructed from density functional theory calculations. It is demonstrated that by learning from the underlying density functional theory results, the trained machine learning potential is able to reproduce important properties of all available sodium phases with an exceptional accuracy in comparison to those computed using density functional theory. In combination with the metadynamics methods, this well trained machine learning potential is applied to large simulation boxes containing 1024 and 3456 sodium atoms in the cI16 phase. These large-scale simulations reveal a notable phase transition at 150 K and 120 GPa with an impressive capturing of the rearrangements of atomic configurations involved in the transition process that may not be evident in a small-scale simulation. Without a doubt, this work shows that applying machine learning methods to condensed matter systems will lead to significant increase in our understanding of important processes such as atomic rearrangements, growth and nucleation process in crystal formation and phase transition.

Statement of Co-authorship

In this thesis, I present my contribution to this work. However, the published research papers are as a result of collaborations between the author, Adebayo Oluseun Adeniyi, thesis supervisor Prof. Yansun Yao of the Department of Physics and Engineering Physics at the University of Saskatchewan, Saskatoon, Dr. Elissaios Stavrou, of Lawrence Livermore National Laboratory, California and Dr. Hanyu Liu of the International Center for Computational Method and Software and State Key Laboratory of Superhard Materials, College of Physics, Jilin University, Changchun 130012, China. The contributions are described below.

Chapter 1 is the description of the fundamental first-principles theory applied in this thesis and it is solely written by Adebayo O. Adeniyi.

Chapter 2 presents a detailed explanation of important structure prediction methods that are mostly used in this research area with important case study to illustrate successful applications where possible and it is completely written by Adebayo O. Adeniyi.

Chapter 3 is based on the paper "High-enthalpy crystalline phases of cadmium telluride" published in Physical Review Research. Experimental data for this cadmium telluride project was supplied by Dr. Elissaios Stavrou and theoretical calculations and theoretical analyses were carried out by Adebayo O. Adeniyi and Prof. Yansun Yao. The manuscript was drafted by all authors.

Chapter 4 is based on the paper "Prediction of a stable helium-hydrogen compound: First-principles simulations" published in Physical Review B. Theoretical calculations and theoretical analyses were carried out by Adebayo O. Adeniyi and results were interpreted by Adebayo O. Adeniyi and Prof. Yansun Yao. The equations of state were repeated using QUANTUM ESPRESSO with tight norm-conserving PBE pseudopotentials by Dr. Hanyu Liu and molecular dynamics simulation was checked by Adebayo A. Adeleke. The manuscript was drafted by Adebayo O. Adeniyi and improved by all authors.

Chapter 5 presents a machine learning potential for sodium based on the Gaussian process regression method and weighted atom-centered symmetry functions representation of the potential energy surface. This chapter is the "manuscript in progress" version of the research work and it is completely written by Adebayo O. Adeniyi

Chapter 6 is a general summary of the research projects in this thesis and it is written completely by Adebayo O. Adeniyi.

Acknowledgements

I will begin by expressing my gratitude to the University of Saskatchewan, located on Treaty 6 Territory and the Homeland of the Métis.

I would like to express my profound appreciation to Prof. Yansun Yao, for his support and encouragement as my thesis advisor; thank you for your patience and for sharing your expertise. I also appreciate the supportive role of my advisory committee members: Prof. Gap Soo Chang, Prof. John Tse, Prof. Chijin Xiao and Prof Yuanming Pan: their constant and enormous support made my PhD program successful.

I am thankful to Dr. Gerhard Herzberg Memorial Scholarship. I also appreciate the financial support of Canadian Natural Sciences and Engineering Research Council (NSERC) and the Department of Physics and Engineering Physics. I acknowledge access to high performance computers: Compute Canada (Westgrid), Plato at the University of Saskatchewan on which most of the research reported in this thesis were performed.

Without the ceaseless support, magnificent patience and unconditional love of my wife and my family none of these would have been possible thank you all for your unwavering love. I cannot forget to say a big thanks to my friends Nnanna Ukoji, Hammed Ejalonibu and Adebayo Adeleke for being available when the going was very tough. Finally, I will also like to express gratitude to everyone that I have met in the course of my program. You are all part of this success.

Dedication

To God and family.

Contents

List of Tables

List of Figures

List of Abbreviations

2D	Two Dimension
3D	Three Dimension
ASE	Atomic Simulation Environment
ACSFs	Atom Centered Symmetry Functions
AIRSS	Ab initio Random Structure Search
ANN	Artificial Neural Network
BCC	Body Centered Cubic
BCP	Bond Critical Points
BH	Basin Hopping
BZ	Brillouin Zone
CALYPSO	Crystal structure prediction Analysis by Particle Swarm Optimization
CBM	Conduction Band Minimum
CCP	Cage Critical Point
CNT	Carbon Nano-Tube
DAC	Diamond Anvil Cell
DFT	Density Functional Theory
DFPT	Density Functional Perturbation Theory
DOS	Density of States
EOS	Equation of States
ELF	Electron Localization Function
FCC	Face Centered Cubic
GA	Genetic Algorithm
GGA	Generalized Gradient Approximation
GPR	Gaussian Process Regression
KS	Kohn Sham
LDA	Local Density Approximation
MD	Molecular Dynamics

ML	Machine Learning
MLP	Machine Learning Potential
NCP	Nuclear Critical Point
PAW	Projector Augmented Wave
PBE	Perdew-Burke-Ernzerhof
PBC	Periodic Boundary Conditions
PES	Potential Energy Surface
PIMD	Path-Integral Molecular Dynamics
PIMC	Path-Integral Monte Carlo
PW	Plane Wave
PV	PhotoVoltaic
PSO	Particle Swarm Optimization
QE	Quantum ESPRESSO
QTAIM	Quantum Theory of Atom in Molecule
RCP	Ring Critical Point
SA	Simulated Annealing
STM	Scanning Tunnelling Microscopy
VASP	Vienna Ab-initio Simulation Package
VBM	Valence Band Maximum
wACSFs	Weighted Atom Centered Symmetry Functions
WZ	Wurzite
XRD	X-ray Diffraction Pattern
vdW	van der Waals
ZB	Zincblende

Chapter 1

INTRODUCTION

Interesting properties of condensed matter materials that may not be accessible at ambient conditions could be triggered at extreme conditions such as high pressure and temperature. At high pressure in particular, they could undergo pressure induced structural transformation that is often accompanied with a change in electronic, mechanical or optical properties. An explicit understanding of the physical and chemical properties of these numerous materials is the fundamental underpin to their potential applications. For this reason, condensed matter research area has received huge attention from both experimentalists and theorists for several decades, leading to an overwhelmingly large number of novel discoveries [1]. These discoveries were unraveled due to the advancement of experimental high-pressure techniques including laser-heated diamond anvil cell (DAC), as well as improved computational efficiency through the state-of-the-art first principles calculations. Despite the notable improvements in high pressure experimental techniques in recent years, these extreme conditions may not be easily attained. Meanwhile in theory, with the application of first principles methods and numerical simulations, the behaviour and properties of materials at extreme conditions can easily be investigated. In the last few decades, the amazing improvements in computational power has further contributed to the significant role of theory to the field of high pressure physics. Nowadays, results from theoretical investigations often serve as dependable guide to experiments and vice versa.

Condensed matter materials contain large number of electrons and nuclei with characteristics behaviour that can be understood with the principles of quantum mechanics. In principle, one should explore the properties of these materials by solving the many body Schrödinger equation. At best this can be solved completely for simplest systems such as mono-atomic or

diatomic systems. In a solid system for instance, there are about an order of 10^{23} particles and for this reason, it is not possible to solve such system quantum mechanically. Therefore, to reduce the complexity of these many body problems, several approximations have been developed over the years. For instance, in the Born-Oppenheimer approximation [2], the motion of the light mass electron is separated from that of the heavier mass of nucleus with the argument that the speed of the electron would be much higher than that of the nucleus so that relative to the electron, it can be considered fixed thereby reducing the complexity of the problem. Furthermore, in a crystalline solid, the periodic boundary conditions (PBC) and Bloch theorem help to reduce the infinitely large system to the simplest repeatable unit cell so that one can explain all the physics of the material with the properties observed from this unit cell [3]. In the density functional theory (DFT), the physical observables of the many-body system are expressed as a functional (function of a function) of a spatial dependent electron density [4]. Meanwhile, in the pseudopotential method, an effective potential is used to replace the complex motion of the core electrons and the nucleus in which case the pseudowavefunctions that corresponds to the new potential do not display the fast oscillation of the true wavefunctions and therefore reduces the number of basis sets required to represent them [5, 6, 7]. With planewave basis sets, the complex electronic wavefunction is replaced with a more tractable mathematical representation. In first principles techniques within the density functional theory frame work, upon which the works in this thesis are based, all of the aforementioned approximations have been implemented.

1.1 Schrödinger and Born-Oppenheimer Approximation

The understanding of electronic structure of matter is based on the theoretical methods of quantum mechanics and statistical mechanics. The motion of atoms and subatomic particles is govern by the Schrödinger equation [8]:

$$\hat{H}(\mathbf{r},\mathbf{R})\Psi(\mathbf{r},\mathbf{R},t) = i\hbar\frac{\partial\Psi(\mathbf{r},\mathbf{R},t)}{\partial t} \tag{1.1}$$

where $\hat{H}(\mathbf{r},\mathbf{R})$ is the Hamiltonian, $\Psi(\mathbf{r},\mathbf{R})$ is the wavefunction of the system, $\mathbf{r}$ and $\mathbf{R}$ are the positions of the electrons and the positions of the nuclei respectively, $\hbar = \frac{h}{2\pi}$ is the reduced Planck constant, and t is the time. If the Hamiltonian is time independent, then the equation becomes:

$$\hat{H}(\mathbf{r},\mathbf{R})\Psi(\mathbf{r},\mathbf{R}) = E\Psi(\mathbf{r},\mathbf{R}) \tag{1.2}$$

where E is the energy level of the system. $\mid \Psi \mid^2$ gives the probability density for finding electrons at positions $\mathbf{r} = r_1, r_2, r_3 \ldots, r_N$ and nuclei at positions $\mathbf{R} = R_1, R_2, R_3 \ldots, R_M$. The Hamiltonian, $\hat{H}$ contains the following (in atomic units):

electronic kinetic energy

$$T_e = -\frac{1}{2}\sum_{j=1}^{N} \nabla_j^2 \tag{1.3}$$

nuclear kinetic energy

$$T_M = -\frac{1}{2}\sum_{j=1}^{M} \nabla_j^2 \tag{1.4}$$

electron-nuclei Columbic potentials

$$V_{eM} = -\sum_{j=1}^{M} Z_j \sum_{i=1}^{N} \frac{1}{\mid \mathbf{r}_i - \mathbf{R}_j \mid} \tag{1.5}$$

nuclei-nuclei Coulomb repulsion

$$V_{MM} = +\sum_{j<i=1}^{M} Z_j Z_i \frac{1}{\mid \mathbf{R}_i - \mathbf{R}_j \mid} \tag{1.6}$$

and the electron-electron Coulomb repulsion

$$V_{ee} = \sum_{j<i=1}^{N} \frac{1}{\mid \mathbf{r}_i - \mathbf{r}_j \mid} \tag{1.7}$$

Z is the atomic number, N is the total number of electrons and M is the total number of nuclei.

This Schrödinger equation is a second order differential equation in $3M$ and $3N$ coordinates

and for this reason difficult to solve exactly, hence certain approximations have to be made in order to solve it for a system of N electrons and M nuclei. The first of these approximations is the Born-Oppenheimer approximation [2]. In this approximation, we first ignore the kinetic energy T_M motion of the nuclei (i.e. we assume the nuclei are fixed at specified locations $\mathbf{R}$ because their motion is much lesser than that of the electrons since the mass of the nucleus is much greater than the mass of an electron) and solve the electronic Schrödinger equation which can be written as:

$$\hat{H}^0\Psi_k(\mathbf{r},\mathbf{R}) = E_k\Psi_k(\mathbf{r},\mathbf{R}). \tag{1.8}$$

The Hamiltonian $\hat{H}^0$ contains all of $\hat{H}$ except T_M. $\hat{H}^0$ is Hermitian so its eigenfunctions form a complete and orthonormal set of functions of $\mathbf{r}$. Thus Ψ can be expanded in terms of the linear combination of Ψ_k:

$$\Psi(\mathbf{r},\mathbf{R}) = \sum_k \Psi_k(\mathbf{r},\mathbf{R})\chi_k(\mathbf{R}) \tag{1.9}$$

The wavefunctions $\Psi_k(\mathbf{r},\mathbf{R})$ and expansion coefficient χ_k depend on $\mathbf{R}$ because H^0 depends on $\mathbf{R}$ through V_{eM} and V_{MM}. We can now use the expansion in the full wave equation so that

$$\hat{H}(\mathbf{r},\mathbf{R})\Psi(\mathbf{r},\mathbf{R}) = E\Psi(\mathbf{r},\mathbf{R}) \tag{1.10}$$

becomes

$$\left(\hat{H}^0 - \frac{1}{2}\sum_{j=1}^{M}\nabla_j^2 - E\right)\sum_k \Psi_k(\mathbf{r},\mathbf{R})\chi_k(\mathbf{R}) = 0. \tag{1.11}$$

Now if one multiply on the left by Ψ_l^* and integrate over the position of the electrons, noting that $\langle\Psi_l|\Psi_k\rangle = \delta_{lk}$, we have:

$$\left(E_l(\mathbf{R}) - \frac{1}{2}\sum_{j=1}^{M}\nabla_j^2 - E\right)\chi_l(\mathbf{R}) + \sum_k \left\langle\Psi_l(\mathbf{r},\mathbf{R})\right| - \frac{1}{2}\sum_{j=1}^{M}\nabla_j^2\Psi_k(\mathbf{r},\mathbf{R})\rangle\,\chi_k(\mathbf{R})$$
$$+ \sum_k \left\langle\Psi_l(\mathbf{r},\mathbf{R})\right| - \sum_{j=1}^{M}\nabla_j\Psi_k(\mathbf{r},\mathbf{R})\rangle\,\nabla_j\chi_k(\mathbf{R}) = 0 \tag{1.12}$$

Equation (1.12) is the coupled-channel equations and the last two terms are called the non-adiabatic terms [9]. Furthermore, these non-adiabatic terms make negligible contributions and if they are ignored, we obtain a Schrödinger equation for the vibrational, rotational or

translational motion on the l^{th} energy surface $E_l(R)$:

$$\left(E_l(\mathbf{R}) - \frac{1}{2}\sum_{j=1}^{M}\nabla_j^2 - E\right)\chi_l(\mathbf{R}) = 0 \tag{1.13}$$

This new equation gives the concept of potential energy surface. In other words, the equation shows that nuclear moves with some kinetic energy (the middle term) on a potential energy surface $E_l(R)$ (the first term), i.e., it shows how the energy of the l^{th} electronic state varies with the position of the nuclei, where $E_l(R)$ $(l = 0, 1, 2\dots)$ are the solutions of the Born-Oppenheimer electronic Schrödinger equations. This can be written properly as

$$\left(E_l(\mathbf{R}) - \frac{1}{2}\sum_{j=1}^{M}\nabla_j^2 - E_{L,J,M,v}\right)\chi_{L,J,M,v}(\mathbf{R}) = 0 \tag{1.14}$$

This implies that nuclei move with kinetic energy given by the middle term, they have a potential energy $E_l(\mathbf{R})$ and they have energy levels given by the third term where v is the vibrational quantum number, J and M are the rotational quantum numbers and $\chi_{L,J,M,v}$ are the vibration and rotation wavefunction [9].

Now, to solve the electronic Schrödinger equation is also difficult because the term V_{ee} prevents us from using separation of variable since it is not one electron additive. We then introduced the mean field approximation in which V_{ee} is replaced by a one-electron additive potential

$$V_{MF} = \sum_{j=1}^{N} V_{MF}(\mathbf{r}_j), \tag{1.15}$$

called the mean field potential and the solutions of each Ψ_l can now be written as a product (slater determinant) of functions of individual electron coordinates called spin orbitals $\Phi_j(r)$:

$$\Psi_j(\mathbf{r}) = \mid \Phi_1\Phi_2\Phi_3\dots\rangle \tag{1.16}$$

This concept of having orbitals and making slater determinants from them is a starting point for most of the approximations used in solving electronic structure equations [9].

1.2 Density Functional Theory (DFT)

In density functional theory, the properties of an atom or molecule are expressed in terms of the electron density which is a much simpler object than wavefunction. The equations for determining the orbitals are called the Kohn-Sham equations [4, 10]:

$$\left[-\frac{1}{2}\nabla^2 - \sum_j Z_j \frac{1}{\mid \mathbf{r} - \mathbf{R}_j \mid} + \int \rho(r') \frac{1}{\mid \mathbf{r} - \mathbf{r}' \mid} dr' + U(\mathbf{r})\right] \phi_i = \varepsilon_i \phi_i \tag{1.17}$$

in which the Coulomb potential is written as $\int \rho(\mathbf{r}') \frac{1}{|\mathbf{r}-\mathbf{r}'|} dr'$, and the exchange potential as well as the electron correlation are embedded in $U(\mathbf{r})$. The theorem of Hohenberg-Kohn is a fundamental underpin of the density functional theory [4].

1.2.1 Hohenberg-Kohn Theorem

The theorem states that the ground-state electron density $\rho(\mathbf{r})$ describing any N-electron system uniquely determines the potential V($\mathbf{r}$) (the nuclear attraction potential) in the Hamiltonian

$$\hat{H} = \sum_j \left(-\frac{1}{2}\nabla_j^2 + V(\mathbf{r}_j) + \frac{1}{2}\sum_k \frac{1}{\mid \mathbf{r}_j - \mathbf{r}_k \mid}\right). \tag{1.18}$$

Hence, since $\hat{H}$ determines the energies and wavefunctions of the system, the ground-state density $\rho(\mathbf{r})$ determines all the properties of the system. The theorem can be proved as follows:

suppose one knows the electron density $\rho(\mathbf{r})$ at all points r so that one can determine the total number of electron $N = \int \rho(\mathbf{r}) d^3r$. Then, one can write the kinetic energy and the electron-electron repulsion part of the Hamiltonian as:

$$\hat{H} = \sum_j \left(-\frac{1}{2}\nabla_j^2 + \frac{1}{2}\sum_k \frac{1}{\mid \mathbf{r}_j - \mathbf{r}_k \mid}\right). \tag{1.19}$$

Assume there are two distinct potential V($\mathbf{r}$) and V'($\mathbf{r}$) that form two distinct Hamiltonians $\hat{H}$ and $\hat{H}'$ but having the same electron density, with ground-state energies and wavefunctions E_0, $\Psi(\mathbf{r})$ and E_0', $\Psi'(\mathbf{r})$ respectively. If one applies Ψ' as a wave function of the Hamiltonian

$\hat{H}$, then :

$$E_0 < \langle \Psi' | \hat{H} | \Psi' \rangle = \langle \Psi' | \hat{H}' | \Psi' \rangle + \int \rho(\mathbf{r})[V(\mathbf{r}) - V'(\mathbf{r})]d^3r = E_0' + \int \rho(r)[V(\mathbf{r}) - V'(\mathbf{r})]d^3r \tag{1.20}$$

similarly

$$E_0' < \langle \Psi | \hat{H}' | \Psi \rangle = \langle \Psi | \hat{H} | \Psi \rangle + \int \rho(\mathbf{r})[V'(\mathbf{r}) - V(\mathbf{r})]d^3r = E_0 + \int \rho(\mathbf{r})[V'(\mathbf{r}) - V(\mathbf{r})]d^3r \tag{1.21}$$

Adding these two equations gives:

$$E_0 + E_0' < E_0 + E_0' \tag{1.22}$$

which is a contradiction. Thus, two distinct potentials cannot give the same electron density and the same number of electrons. This implies that $\rho(r)$ determines N and a unique V and hence determines the Hamiltonian and therefore all the wavefunctions and all the energies [4, 9].

1.2.2 Kohn-Sham Formalism

The K-S process allows us to solve the equation :

$$\left[-\frac{1}{2}\nabla^2 - \sum_j Z_j \frac{1}{\mid \mathbf{r} - \mathbf{R}_j \mid} + \int \rho(\mathbf{r}') \frac{1}{\mid \mathbf{r} - \mathbf{r}' \mid} dr' + U_{xc}(\mathbf{r}) \right] \phi_i = \varepsilon_i \phi_i \tag{1.23}$$

to get $\phi_j' s$ whose density $\sum_{j=occ}^{N} \mid \phi_j(\mathbf{r}) \mid^2$ gives the correct density where N is the total number of electrons in the system. Here, the total energy is expressed as a functional of the density:

$$E[\rho] = T_s[\rho] + \int v_{ext}\rho(\mathbf{r})dr + E_H[\rho] + E_{xc}[\rho] \tag{1.24}$$

where T_s is the kinetic energy that can be written in terms of the Kohn-Sham orbitals as:

$$T_s[\rho] = \sum_{i=1}^{N} \int dr \phi_i^* (-\frac{1}{2}\nabla^2)\phi_i(\mathbf{r}) \tag{1.25}$$

and v_{ext} is the external potential on the system and E_H is the Coulumb (or Hartree) energy:

$$E_H = \frac{1}{2}\int dr \int dr' \frac{\rho(\mathbf{r})\rho(\mathbf{r}')}{\mid \mathbf{r} - \mathbf{r}' \mid} \tag{1.26}$$

E_{xc} is the exchange-correlation energy. Kohn-Sham equations are obtained by the variation of the total energy with respect to a set of orbitals, with some constraints on those orbitals to give the Kohn-Sham potential [10], which can be written as

$$v_{eff}(\mathbf{r}) = v_{ext}(\mathbf{r}) + \int \frac{\rho(\mathbf{r}')}{\mid \mathbf{r} - \mathbf{r}' \mid} dr' + v_{xc}(\mathbf{r}) \tag{1.27}$$

where

$$v_{xc}(r) = \frac{\delta E_{xc}[\rho]}{\delta \rho(\mathbf{r})} \tag{1.28}$$

is the exchange-correlation potential. Thus the equation satisfied by the system can be written as:

$$\left(-\frac{1}{2}\nabla^2 + v_{eff}(\mathbf{r})\right)\phi_i(\mathbf{r}) = \varepsilon_i \phi_i(\mathbf{r}). \tag{1.29}$$

In contrast to the first three terms on the right hand side of equation (1.24) for which the exact analytic dependence on ρ could be determined, the analytic form of the ρ dependence of $E_{xc}[\rho]$ is not known. In practice, certain approximations are used for the expression of $E_{xc}[\rho]$.

1.2.3 Exchange-Correlation Approximations

As mentioned earlier, the major challenge in the application of DFT is that we do not know the exact value of the exchange-correlation functional. In this section, a brief discussion of the most widely used approximations is given.

Local Density Approximation (LDA)

It is the simplest approach used in density functional approximation for the exchange-correlation energy. In this approximation, the homogeneous density ρ_0 in the exchange-correlation energy density of the homogeneous electron gas $\epsilon_{xc}^{hom}(\rho_0)$ is replaced by the inho-

mogeneous density $\rho(r)$ [4]:

$$\epsilon_{xc}^{LDA}(\rho(\mathbf{r})) = \epsilon_{xc}^{hom}(\rho_0) \mid_{\rho_0=\rho(\mathbf{r})} \tag{1.30}$$

Thus the exchange-correlation energy functional is

$$E_{xc}^{LDA}[\rho(\mathbf{r})] = \int \epsilon_{xc}^{LDA}\rho(\mathbf{r})d^3r \tag{1.31}$$

Generalized Gradient Approximation (GGA)

Rather than having a uniform electron density, real materials have a slowly varying density. For this reason, GGA functional is written as a combination of the local electron density and the spatial variation in the electron density which is expressed as the density gradient [11]. The general form of the functional is:

$$E_{xc}^{GGA}[\rho(\mathbf{r})] = \int \epsilon_{xc}^{GGA}[\rho(\mathbf{r}), \nabla(\rho(\mathbf{r})]d^3r \tag{1.32}$$

1.2.4 Periodic Boundary Conditions

Crystalline solids are made from repeated groups of identical atoms called basis. The set of mathematical points in which a basis could sit are referred to as the lattice. The periodicity of the lattice is defined in 3 dimension using the 3 translation vectors that permit the crystal to be the same when view from a point $\vec{T}$ and another point $\vec{T'}$ give by:

$$\vec{T'} = \vec{T} + n_1\vec{b_1} + n_2\vec{b_2} + n_3\vec{b_3}, \tag{1.33}$$

where n_1, n_2 and n_3 are integers and $\vec{b}_1$, $\vec{b}_2$ and $\vec{b}_3$ are noncoplanar vectors [12]. This allows the application of periodic boundary conditions (PBC) through the Bloch theorem [3] in a periodic potential of a general form

$$V(\vec{r} + \vec{T}) = V(\vec{r}). \tag{1.34}$$

Indeed the periodicity of the potential permits one to write the potential in terms of Fourier series as:

$$V(\vec{r}) = \sum_G V_G e^{i\vec{G}\cdot\vec{r}}, \tag{1.35}$$

where $\vec{G}$ are sets of vectors and V_G are coefficients. Thus, equations (1.34) and (1.35) imply that

$$e^{i\vec{G}\cdot\vec{T}} = 1, \tag{1.36}$$

so that

$$\vec{G}\cdot\vec{T} = 2l\pi, \tag{1.37}$$

where l is an integer. Following equation (1.33), one can write

$$\vec{G} = m_1\vec{B_1} + m_2\vec{B_2} + m_3\vec{B_3}, \tag{1.38}$$

where m_1, m_2 and m_3 are integers and $\vec{B_1}$, $\vec{B_2}$ and $\vec{B_3}$ are vectors defined as

$$\vec{b_i}\cdot\vec{B_j} = 2\pi\delta_{ij} \tag{1.39}$$

Invariably, it implies that the existence of lattice vector in real space connote the existence of lattice vector in k-space in which the vectors $\vec{G}$ define the reciprocal lattice with primitive translation vectors $\vec{B_j}$. This periodicity in the k-space is an indication that all information about the crystal can be contained in the primitive unit cell of the reciprocal lattice referred to as the first Brillouin zone. Now according to Bloch theorem [3], the eigenstates of a one-electron Hamiltonian such as equation (1.29), for a periodic potential (i.e V($\vec{r}$+$\vec{T}$)=V($\vec{r}$)) for all Bravais lattice translation vectors $\vec{T}$ can be a written as the product of the plane wave and a function with the periodicity of the Bravais lattice i.e.

$$\psi_i(\vec{k},\vec{r}) = e^{i\vec{k}\cdot\vec{r}}u_i(\vec{k},\vec{r}), \tag{1.40}$$

where $u_i(\vec{k},\vec{r})$ represents a periodic function with the periodicity of the lattice ($u_i(\vec{k},\vec{r}) = u_i(\vec{k},\vec{r}+\vec{T})$), $\vec{k}$ is the wave vector of the electron in the first Brillouin zone. Therefore, one

can write

$$\psi_i(\vec{k}, \vec{r} + \vec{T}) = e^{i\vec{k}\cdot\vec{r}}\psi_i(\vec{k}, \vec{r}) \tag{1.41}$$

Now using equation (1.41) in the KS equation of (1.29), one will obtain a set of eigen-equations for each $\vec{k}$. By doing so, the problem had been transformed from that of solving for infinite number of electrons in the system to that of a finite number of electronic bands at an infinite number of k-points in the reciprocal unit cell [12]. However, the wavefunction at the k-points that are around each other would be identical so that one can represent the wavefunctions over a small region of reciprocal space around a particular k-point by the wave function in this k-point. That way, only a discrete but densely packed k-point mesh is needed to completely determine the ground state of the crystalline solid. Meanwhile the permitted k-points is proportional to the volume of the solid [12].

1.2.5 The Plane Wave Basis Sets

There are several basis sets that can be used to represent the KS wave function. Examples include atomic orbitals, Gaussians and plane waves(PW) basis set [13, 14]. The primary advantages of the plane wave basis set are the simplicity of the function with no preconception about the form of the solution, no basis set superposition error as well as good efficiency in computing the forces on atoms. To express any wavefunction in terms of the PW basis, one would need a continuous and infinite basis set. Be that as it may, the application of periodic boundary conditions permit the use of Bloch theorem so that one can write the KS wavefunction as:

$$\psi_i(\vec{k}, \vec{r}) = e^{i\vec{k}\cdot\vec{r}}u_i(\vec{k}, \vec{r}) = \frac{1}{\sqrt{V}}\sum_G C_{i,\vec{k}+\vec{G}}e^{i(\vec{k}+\vec{G})\cdot\vec{r}} \tag{1.42}$$

where $\vec{G}$ is the reciprocal lattice vector, k is a symmetry label that lies in the first Brillouin zone and $C_{i,\vec{k}+\vec{G}}$ are the coefficients. The basis set for any give k will be discrete and infinite as expected but in practice, only the plane waves with energy less than a predefined cutoff energy (E_{cut}) are included, where E_{cut} is defined as:

$$\frac{1}{2} \mid \vec{k} + \vec{G} \mid^2 \leq E_{cut}. \tag{1.43}$$

Therefore, the convergence of the calculation can be checked and ascertained by varying only the cutoff energy.

1.2.6 Pseudopotential approximation

The core electrons are very closely bound to the nucleus so that the chemical properties of an atom will be mostly affected by the valence electrons which are relatively loosely bound. Therefore it is safe to assume that the contribution of the core electrons to the binding energy will not change when isolated atoms are combined to form a molecule or crystal. Thus, the important energy difference will be from the valence electrons which will result in a relatively easy computation. Also, an accurate computational representation of the strong nuclear Coulombic potential and the localized core electrons wavefunctions is not trivial. It must be noted that the atomic wavefunctions are eigenstates of the Hamiltonian so they must be mutually orthogonal. Also the core states are localized around the nucleus, therefore the valance state must oscillate rapidly in the core region in order to fulfil the orthogonality condition [15]. This fast oscillation give rise to a large kinetic energy for the valence electrons in the core region that somewhat cancels the large potential energy of the strong Coulomb potential so that the valence electrons becomes weakly bound than the core electrons. For this reason, it is convenient to represent the strong Coulomb potential and core electrons by a pseudopotential and replace the valence electron wavefunctions that oscillate rapidly in the core region by a pseudo wave functions that vary smoothly in the core region [6, 7]. A sketch of the concept is given in Figure 1.1. The pseudopotential and pseudo wavefunction are expected to be the same beyond a cutoff radius r_c from the nucleus. The value of the cutoff radius is usually obtained by ensuring that the core regions of neighboring atoms do not overlap.

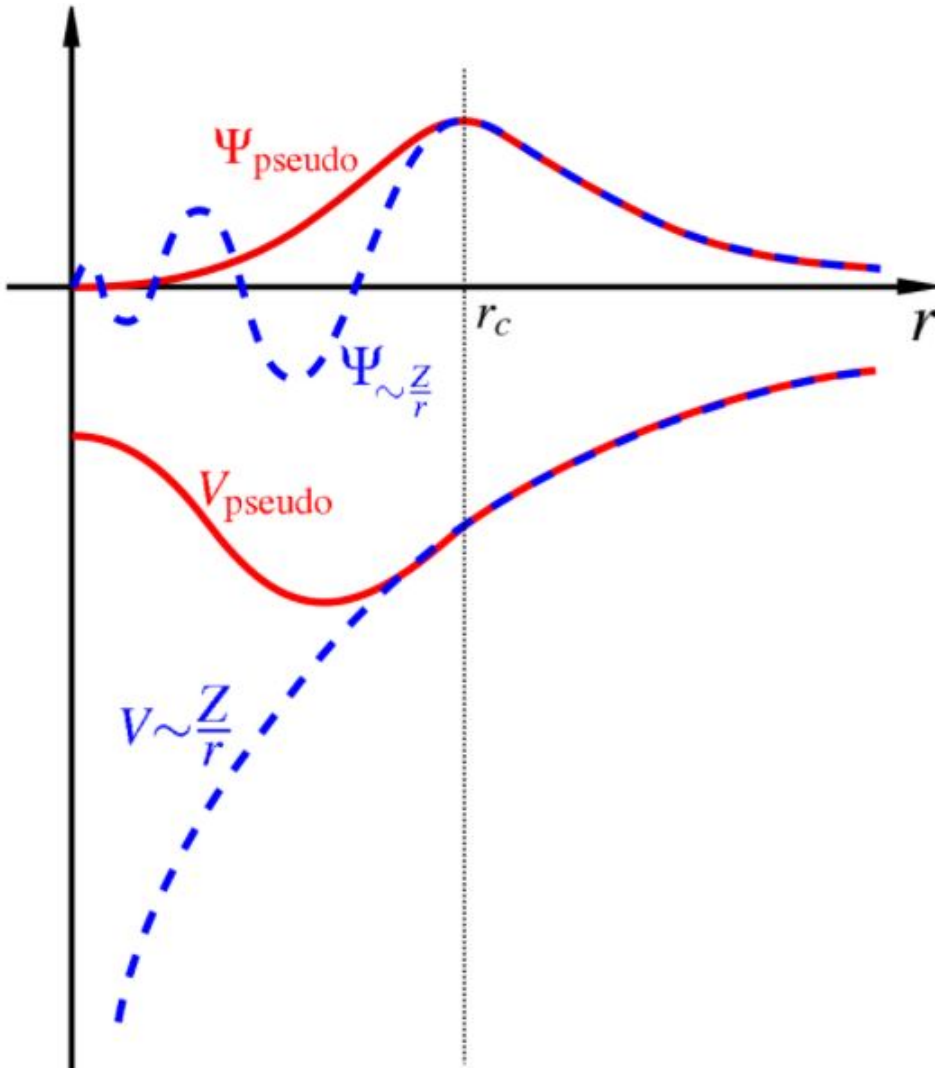

Figure 1.1: All-electron valence wavefunction and electronic potential (dashed blue lines) plotted against distance, r, from the atomic nucleus. The corresponding pseudo-wave function and potential is plotted (solid red lines). This figure was taken from http://en.wikipedia.org/wiki/Pseudopotential.

1.2.7 Projector Augmented Wave (PAW) Method

One significant advantage of the application of plane-wave basis sets and pseudopotential approximation is that they have a simple form that is easy to track [16]. However, a huge price must be paid for such simplicity in that transition metals and rare-earth metals are difficult and computationally tedious to explore with a standard pseudopotential [17, 18]. Therefore, several other methods have been proposed including the ultrasoft pseudopotential method of Vanderbilt [19] and the projector augmented-wave (PAW) method of Blöchl [20]. The PAW method is an approach that permits the construction of an all electron wave function by summing the pseudo-wave function in the region outside the core around which the pseudo-wave function takes the same form as the all electron wave function (as shown in Figure 1.1), and the partial wavefunction inside the core minus the pseudo partial wavefunction in the core area. Ideally, the wavefunction of material systems has various underlying properties at distinct locality. In the valence area where bonding takes place, it is somewhat smooth whereas around the nucleus, it has a rapid oscillation because of the nuclear attraction [16]. For this reason, it is very problematic for electronic structure methods to capture bonding area precisely when taking care of the huge fluctuation in the core. In an attempt to tackle this problem, Blöchl proposed the PAW method in which an all electron wavefunction is obtained from the pseudo wavefunction. Precisely, in the PAW approach, the one electron wavefunctions ψ_{nk} are derived from the pseudo wavefunctions $\tilde{\psi}_{nk}$ by using a linear transformation shown below:

$$|\psi_{nk}\rangle = |\tilde{\psi}_{nk}\rangle + \sum_i \left(|\phi_i\rangle - |\tilde{\phi}_i\rangle\right) \langle \tilde{p}_i \mid \tilde{\psi}_{nk}\rangle \tag{1.44}$$

where nk is the band and k-point index, $|\phi_i\rangle$ and $|\tilde{\phi}_i\rangle$ are the partial waves of the all electron potential and the corresponding pseudo potential respectively. $\tilde{p}_i$ are the projector functions which are orthonormal to the partial waves, i.e.

$$\langle \tilde{p}_i \mid \tilde{\phi}\rangle = \delta_{ij}. \tag{1.45}$$

In principle, the PAW method can be implemented as an all-electron method [20] but in practice, all implementations so far are within the frozen core approximation of the core electrons in which case the core of an atom is assumed frozen [21]. Primarily, PAW method demonstrates notable benefits of pseudopotential methods as well as retaining most of the physics of an all-electron calculation.

1.2.8 van der Waals Density Functional

Dispersion interactions such as van der Waals (vdW) forces which are not readily captured by the LDA and GGA approximations are essential contributors to the binding of biomolecules such as DNA, molecular crystals and molecules on surfaces. Describing dispersion (which in many cases occur together with hydrogen bonds) accurately has been a major problem in electronic structure theory. Meanwhile conventional DFT calculations within GGA and LDA approximations are well known to be insufficient in accounting for dispersion interactions. Therefore, many notable methods have been developed to account for dispersion within DFT [22, 23, 24]. Among these methods, the non-local van der Waals density functional (vdW-DF) of Dion et al. [22] has become very popular.

In vdW-DF, the non-local correlation is obtained in a way that permits the exchange-correlation energy to be expressible as

$$E_{xc} = E_x^{GGA} + E_c^{LDA} + E_c^{nl} \tag{1.46}$$

where E_x^{GGA} is the GGA exchange energy, E_c^{LDA} takes care of the local correlation energy and E_c^{nl} is the non-local correlation energy [25]. In addition to the original vdW-DF method [22], other versions such as optPBE-vdW, optB88-vdW, and optB86-vdW have been proposed in which cases the exchange functionals are optimised [25, 26].

1.2.9 Self Consistency and ground state total energy

Now that we have all the required technique, the KS equation can be solved in a self consistent approach to obtain the ground state electron density and the ground state total energy. The

flow chart in Figure 1.2 illustrate the procedure.

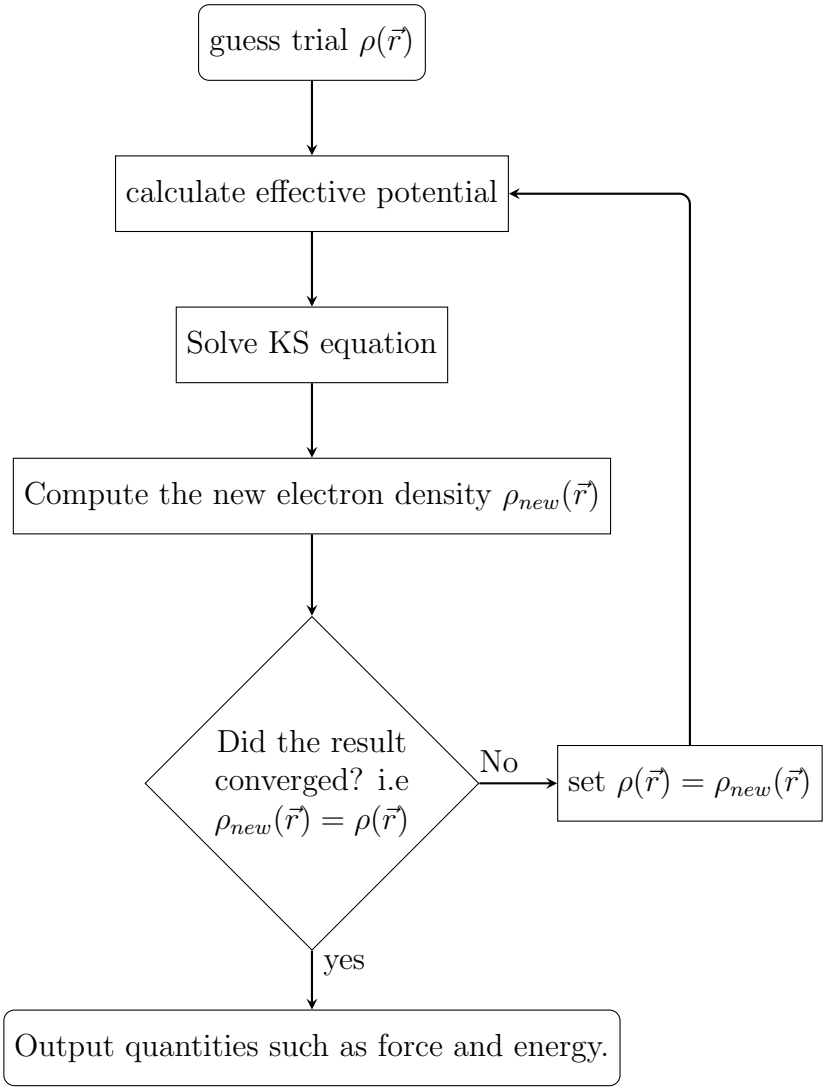

Figure 1.2: The flow chart of self consistent calculations

The procedure begins by guessing an initial electron density usually from the non-interacting atoms of the system in consideration. This charge density is then applied to construct an effective potential which then make KS equation solvable. The KS orbitals are represented by the pseudo wavefunctions that will be expanded using a set of plane waves truncated by the energy cut off. Often, the solutions of KS equations for each k-point give rise to several orbitals that can be used to build a new electron density. A comparison between the initial guess and the new density is used to ascertain they agree within a tolerance after which

the calculation is said to have converged. If they do not agree within the tolerance, one reconstruct a new set of potential with the new electron density and redo the calculation. This process will be repeated until convergence is achieved after which, the electron density will be applied to calculate the ground-state total energy and other quantities as needed [9].

1.3 Quantum Theory of Atoms in Molecules

In this model, atoms and bonds are expressed in terms of the electron density distribution function which is a probability distribution that describes the average spread of the electron charge throughout the real space in the attractive field created by the nuclei. Essential information about the molecular structure are revealed by the turning points of the electron density with the gradient of its path that originates and terminates at these critical point [27]. In addition, chemical bonding and structure of a chemical system can be defined from the topology of the electron density. Indeed the topology of the electron density is influenced by the attractive force of the nucleus so that there exists a local maximum at the position of the nucleus. This maximum point is called the nuclear critical point (NCP). Other critical points are bond critical point (BCP), cage critical point (CCP) and ring critical point (RCP). At critical points, the gradient of the electron density is zero. i.e.

$$\nabla\rho = \hat{i}\frac{\partial\rho}{\partial x} + \hat{j}\frac{\partial\rho}{\partial y} + \hat{k}\frac{\partial\rho}{\partial z} \rightarrow \begin{cases} = 0 \ (at\ C.P) \\ \\ \neq 0 \ (generally\ at\ other\ points) \end{cases} \tag{1.47}$$

Gradient vector field lines that belongs to an atomic basin converge to one nucleus which is as an attractor to them and by so doing, these gradient vector lines sweep a portion of space associated with one nucleus identified as the basin of an atom in a molecule. Thus an atom in a molecule is the union of a nucleus and its associated basin and each basin is bounded by one "zero flux surface" [28].

The second derivative tensor arranged as Hessian Matrix reveals the kind of stationary point

(minumum, maxima or inflexion)

$$H(r_c) = \begin{bmatrix} \frac{\partial^2\rho}{\partial x^2} & \frac{\partial^2\rho}{\partial x\partial y} & \frac{\partial^2\rho}{\partial x\partial z} \\ \frac{\partial^2\rho}{\partial y\partial x} & \frac{\partial^2\rho}{\partial y^2} & \frac{\partial^2\rho}{\partial y\partial z} \\ \frac{\partial^2\rho}{\partial z\partial x} & \frac{\partial^2\rho}{\partial z\partial y} & \frac{\partial^2\rho}{\partial z^2} \end{bmatrix}_{r=r_c} \tag{1.48}$$

H is real and symmetric matrix and can therefore be diagonalized. Hence,

$$U^{-1}HU = Q \tag{1.49}$$

reduces H to its diagonal form (where U is built from the eigenvector of $H(r_c)$)

$$Q = \begin{bmatrix} \frac{\partial^2\rho}{\partial x^2} & 0 & 0 \\ 0 & \frac{\partial^2\rho}{\partial y^2} & 0 \\ 0 & 0 & \frac{\partial^2\rho}{\partial z^2} \end{bmatrix}_{r=r_c} = \begin{bmatrix} \lambda_1 & 0 & 0 \\ 0 & \lambda_2 & 0 \\ 0 & 0 & \lambda_3 \end{bmatrix} \tag{1.50}$$

where λ_1, λ_2 and λ_3 are the curvature of density and the trace of H is referred to as the Laplacian of density ($\nabla^2(\rho)$). Critical points are classified with the rank and signature (i.e (rank, signature)) where the rank is the total number of non zero curvature (which is 3 for a stable system) and the signature is the algebraic sum of the signs of the curvatures [29]. There are 4 stable critical points:

- (3,-3) : ρ is local maximum $\rightarrow$ NCP
- (3,-1) : ρ is maximum on the plane formed by corresponding eigenvectors but minimum on the third axis perpendicular to the plane $\rightarrow$ BCP
- (3,+1) : ρ is minimum on the plane and maximum at the perpendicular $\rightarrow$ RCP
- (3,+3) : ρ is local minimum $\rightarrow$ CCP

The number and type of critical points that can coexist in a molecule or crystal obeys a strict topological relationship:

$$n_{NCP} - n_{BCP} + n_{RCP} - n_{CCP} = \begin{cases} 1\ (isolated\ molecule) \\ \\ 0\ (crystal\ structure) \end{cases} \tag{1.51}$$

Topology of the electron density determines the form of atoms in a molecule, leading to a natural partitioning of the molecular space into separate mononuclear regions identified as atoms in molecules [29]. The surface bounding an atom in a molecule is one of zero flux in the gradient vector field of the electron density, i.e. it is not crossed by any of the gradient vectors $[\nabla\rho]$ at any point:

$$\nabla\rho(r) \cdot \hat{n}(r) = 0. \tag{1.52}$$

The magnitude of the charge density at the bond critical point indicates the relative strength of the bond and its Laplacian determines the characteristics of atomic interaction. A negative Laplacian is associated with covalent bonding whereas a positive Laplacian can be attributed to closed shell interactions such as dihydrogen, hydrogen bonds and vdW interactions. This method was developed by Richard Bader [28] and has been very successful in identifying and classifying covalent and non covalent bonds.

1.4 Role of Pressure

The application of external pressure can trigger several interesting phenomena that may not be evident at ambient pressure. Remarkably, high pressure can alter the chemistry of materials leading to the formation of unprecedented species as well as resulting into amazing phenomena. The exploration of how matter changes under pressure can be investigated in the laboratories and through implementation of theoretical principles in numerical simulations. From the time Bridgeman proposed the use of pressure sealing in 1905 [30, 31], high pressure in laboratories can nowadays reach several hundreds gigapascal particularly with the advent of diamond anvil cell (DAC), laser heating as well as numerous methods such as neutron and x-ray scattering, infrared and Raman spectroscopy, that can be applied to characterize the new species [32, 33]. On the contrary to experiment, computational simulation is fast and affordable with the ability to go far beyond the pressure limit of currently applied experimental techniques. For this reason, they often serve as an important guide and front runner for material investigations at high pressure. In recent times, crystal structure prediction methods predicated on first principles approach have become very popular and successful due to a remarkable advances in computer power and impressive development in algorithms which

have provided scientists with fascinating tools to probe and classify unprecedented chemical behaviours under pressure. In the best part of last two decades, several structures and thermodynamically stable compounds have been predicted with no input from experiment and some of these predicted structures have been synthesized in the laboratories at high pressure. Diverse unique phenomena have emerged at high pressure and consequently there have been a huge progress in high pressure research in time. The early part of the investigations was tailored to the study of structural transformation, changes in physical properties like superconductivity [34, 35], magnetism [36, 37] and metal-insulator transitions [38], and good metal alloys forming a semiconductor [39]. Despite the fact that such research works are still being investigated, the enormous prospect of high pressure leading to novel discoveries has ensured that other areas could be explored. For instance, sizable amount of interest has nowadays been directed to understanding the formation mechanism, as well as synthesizing several unconventional compounds such as LaH_{10} [40], LiN_5 [41, 42], Na_2He [43, 44] and so on. Interestingly, a lot of these compounds display very astonishing physical and chemical properties. For instance, a compound containing hydrogen and sulphur with stoichiometry H_3S has been reported to be superconducting with critical temperature of about 203 K [45]. Recently, it was reported that compressing a mixture of carbon, sulphur and hydrogen to a pressure above 260 GPa produced a material that is able to transmit electricity without resistance at about room temperature [46]. Discovering these sorts of unconventional compounds and the exceptional variation in their structures clearly indicate that pressure can make a significant change to as well as elevate material discovery.

At high pressure, the structures of solid materials are known to become relatively homogeneous as a result of the compression of the longer and weaker bonds, possessing higher symmetry [47, 48], taking close-packed structures [49] and taking more delocalized electronic states that can trigger insulator-metal transition [47, 48]. A lot of the observation from experiment and theory follows the presumption of homogeneity and close packing. As expected, the proclivity of electron charge density to reach homogeneous state is inched on the fact that the kinetic energy of the electrons grows faster then the Coulomb energy as the electron density increase [50]. Thus, the kinetic energy can be minimized by assuming a ho-

mogeneous density distribution making electron delocalization and metallization attainable for matter at extreme pressures. Nevertheless, many unprecedented phenomena can occur at high pressure. The reality is that not all matter becomes more homogeneous as a result of pressure increase and a deviation from close-packing shape could be employed to reach high density [48]. Recent progress in experiment and computer simulations have resulted in more insight into our understanding of how the properties of matter change at high pressure. Particularly, experiment and theory are now showing that pressure plays a significant role in the formation, geometries and properties of unconventional compounds with unusual bonding and structures. For example, in some compounds, electrons could become very localized and even detach from the atoms to occupy the interstitial site [51, 52]. Also, the phases of crystals seen at elevated pressure are mostly not homogeneous where the stable geometries are made of many molecular or polymeric species [47, 53] with a notable reduction in the coordination number [54, 55]. Moreover, repopulating the atomic orbitals as a result of increasing pressure could influence how the atoms in the system behave chemically. Therefore at high pressure, the behaviour of materials can become very complex, with an unlimited variation in compositions as well as structures attainable, often with unprecedented and novel properties such as the appearance of compound from chemical reactions that do not result in the formation of local chemical bonds [56].

1.5 Thesis Description

The objective of this work is to explore the properties of novel condensed matter materials with the use of first principles methods and computer simulations. Structure properties, electronic properties, dynamical properties and bonding parameters of selected materials were investigated. The tools employed are based on density functional theory (DFT), density functional perturbation theory (DFPT) and projector augmented wave (PAW) method. All the DFT based calculations were performed using VASP [21] and Quantum-ESPRESSO [57, 58] while the topological analysis was performed with CRITIC2 code [59]. A brief description of the applied codes is included below:

1. VASP

VASP is an acronym for Vienna Ab-initio Simulation Package. Based on first principles method, this code can be used to perform quantum-mechanical molecular dynamics (MD) simulations with the use of pseudopotential or projector augmented wave (PAW) which ensure a significant reduction in the size of the basis set. The procedure applied in VASP is that of finite-temperature LDA with an exact calculation of the instantaneous electronic ground state at each MD step by implementing an efficient matrix diagonalization schemes and an efficient Pulay mixing. The implementation of PAW method of Blöchl [20] for electronic structure calculations provides significant access to full wave potential. In principle, this permits the calculation of all-electron properties from pseudopotential-based schemes through the reconstruction of all-electron wavefunctions from the pseudo wavefunctions and allows the core orbitals to adjust under extreme pressure [21].

2. QUANTUM ESPRESSO

   This is an integrated suite of Open-Source code for electronic structure calculations and material modelling that is based on DFT, planewave and pseudopotential. Among other applications, it can be used to perform ground state calculations as well as investigate response properties, spectroscopy properties and quantum transport. Implemented potentials include norm-conserving [60], and ultrasoft [19] pseudopotentials in addition to PAW potential [20].

3. CRITIC2

   This code is used to analyze results from a quantum mechanical calculations performed on either molecules or crystalline solids. It has the capability to analyze and transform data such as structure, electron density, one-electron wavefunction and other scalar fields produced by many quantum chemistry related programs including VASP and Quantum ESPRESSO. Among other significant applications such as structure format manipulation and calculation of quantities like scanning tunnelling microscopy (STM) images, Bader's Quantum Theory of Atoms in Molecules (QTAIM) [28] has been implemented [59].

4. PHONOPY

This is a python-based open-source code that can be used to post-process phonon calculation results from ab initio programs such as VASP and Quantum ESPRESSO [61]. The calculations in this package require a supercell built from a well relaxed crystal structure. Indeed, the accuracy of phonon dispersion result scales positively with the size of the supercell. Typically, one begins by relaxing the unit cell of the crystal structure to a desired equilibrium and then create supercells with displacements and then apply an ab initio code such as VASP to calculate the forces on the atoms in each supercell after which the results are collected and post-processed in phonopy to obtain desired properties such as phonon band structure and phonon dispersion curve [61]. The forces can be obtained using two methods which are finite difference in which each ion is displaced in each independent direction, and the density functional perturbation theory [21].

Chapter 2 of this thesis gives an elaborate description of the important theoretical and computational methods that are commonly applied in the field. Crystal structure prediction methods are nowadays serving as a great guide to experimental investigations of materials. Many of the theoretical techniques in use could successfully identify ground state structure of a compound without any experimental input or any prior information other than a possible stoichiometry. In cases where the ground states are known, molecular dynamics or metadynamics methods could be used to explore possible phase transition in the compound at desired temperature-pressure conditions. Random crystal structure search, genetic algorithm, Particle Swarm Optimization, metadynamics, basin hopping, data mining are some of the important techniques that will be explained in this chapter. To conclude the chapter, three published research papers from our group led by Yansun Yao in which I contributed as coauthor are used to illustrate successful applications of some of the methods above. The published papers are:

- Cheng, X., Guan, J., Jiang, L., Zhang, H., Wang, P.,**Adeniyi, A. O.**, Yao, Y. ... Song, Y. Pressure-induced structural transformations and new polymorphs in $BiVO_4$. Physical Chemistry Chemical Physics, 22(18), 10238-10246 (2020).

- Adeleke, A. A., **Adeniyi, A. O.,** Tang, H., Gou, H., Yao, Y. o-C_{240}: a new sp3-dominated allotrope of carbon. Journal of Physics: Condensed Matter, 32(39), 395401 (2020).

- Adeleke, A. A., Stavrou, E., **Adeniyi, A. O.,** Wan, B., Gou, H., Yao, Y. Two good metals make a semiconductor: A potassium-nickel compound under pressure. Physical Review B, 102(13), 134120 (2020).

Chapter 3 presents the high enthalpy crystalline phases of cadmium telluride (CdTe). The long-sought post-Cmcm phase of the compound is successfully characterised with the application of first principles metadynamics simulations This chapter is a slight modification of the original manuscript that had been published in Physical Review Research:

- **Adeniyi, A. O.,** Kunz, M., Stavrou, E., Yao, Y. High-enthalpy crystalline phases of cadmium telluride. Physical Review Research, 2(3), 033072. (2020)

Chapter 4 is about the prediction of a stable compound of helium and hydrogen. This study reveals that helium although known to be inert at ambient pressure can form a stable compound with hydrogen. Topological analysis of the compound reveal the presence of bond critical points between helium and hydrogen at 0 GPa with strength of charge density and it's Laplacian comparable to those of van der Waals interaction. It was found that these quantities increased significantly to the level associable to those of conventional hydrogen interaction. This chapter is a slight modification to the paper published in Physical Review B:

- **Adeniyi, A. O.**, Adeleke, A. A., Li, X., Liu, H., Yao, Y. Prediction of a stable helium-hydrogen compound:first-principles simulations. Physical Review B, 104(2), 024101 (2021).

Chapter 5 presents a machine learning potential for sodium based on the Gaussian process regression method and weighted atom-centered symmetry functions representation of the potential energy surface. The PES was described by several relevant data sets that represent

different regions of the PES with each data set consisting of three distinct elements namely total energies, interatomic forces, and stress tensors of the cell, which were obtained from DFT-based calculations. It was demonstrated that by learning from these data, the MLP was able to reproduce important properties of sodium crystals.

Chapter 6 is a summary of my research projects and important conclusions as well as possible future work.

Chapter 2
CRYSTAL STRUCTURE PREDICTION METHODS

2.1 Introduction

Theoretical structure prediction using state-of-the-art techniques has done a lot in guiding the synthesis of numerous materials with novel scientific applications. The discovery of new materials is often the fundamental underpin to crucial innovative development in the industry. In particular, crystal structure search techniques have contributed immensely to our understanding of condensed matter systems, from predicting reliable ground state and metastable structures of new materials with little or no prior structure information, to simulating extreme conditions that are unattainable by experiments. For instance, several polymeric nitrogen compounds and nitrogen rich materials that are known to be applicable in high energy density physics were only synthesised long after being predicted by theory [62]. Indeed nitrogen and nitrogen-rich compounds are on the brink of fulfilling their huge potential as practically applicable high energy density materials because numerous theoretical investigations have been producing results that serve as dependable guide for experimental investigations. Another significant role of theory is that by identifying promising candidates ahead of experimental investigations, lots of time will be saved.

For any chemical composition, there are infinite atomic arrangements that can fulfill the symmetry requirements at the respective orbitals. These are all the possible local minima of the energy landscape among which at certain thermodynamic conditions such as temperature and pressure, there exists only finite number of lowest energy structures. Thus, by

crystal structure prediction, we refer to finding the most thermodynamically stable structure at any given pressure-temperature conditions from chemical formula or stoichiometry alone [63]. The dimensionality of the energy landscape for any system with N number of atoms in the unit cell is $3N$+3, from which $3N$-3 degrees of freedom are the atomic positions and the remaining six represents the lattice parameters. In other words, a system with 80 atoms in a unit cell has an energy landscape that is 243 dimensional. This is a clear indication that the difficulty of crystal structure prediction increases exponentially with system size. A number of approaches have been proposed including topological in which case one can construct a simple topology based on what is known about the chemistry of the system [64] and those that depends on empirical correlations through structure diagram [65, 66, 67] in which a large database set of stable structures is required. For this reason, predominantly unbiased, non-empirical and therefore most generally applicable approaches nowadays are based on computational optimization with which one can explicitly calculate the free energy and explore its landscape with the aim of finding the most stable arrangement of the atoms [63].

In recent years, the most used methods in structural predictions are random structure search [68, 69, 70], evolutionary algorithm implemented in USPEX [71], and particle swarm optimization (PSO) method implemented in CALYPSO [72]. Random structure search technique has found many uses in the field of crystal structure prediction. For instance, it has been employed to a high degree of success in the prediction of the ground-state and metastable structures of novel materials such as ice at high pressures [73], atomic metallic hydrogen [74], and several other systems [75]. This method begins with the generation of a number of random configurations which are then optimized in a DFT calculation at constant pressure into a local minimum that corresponds to the minimum energy crystal structure even without any prior knowledge of the structure information except for possible chemical stoichiometry. After enough preliminaries, a decent testing of the setup space is obtained, and the ground-state structure(s) can be distinguished. Meanwhile in the evolutionary algorithm, the first generation is obtained from the optimization of randomly generated structures to produce energetically favourable structures. Thereafter, one discards some of the structures in the

first generation with relatively high energy and uses the good structures with relatively low energy as parents to create the next generation through a successive cycle of heredity and mutation operations followed by a DFT optimization at constant pressure [76]. The offspring structures in the second generation can then be used as parents for the creation of the third generation and so on, in a process similar to Darwinian evolution. Although a branch of the evolutionary method, the PSO method is different from the genetic algorithm in that the main evolutionary operator of crossover and mutation are not used. Proposed by Kennedy and Eberhart [77, 78], this stochastic global optimization approach takes inspiration from the movement of a bird flock which can be compared to a distributed behaviour algorithm that execute several-dimensional search. In this method, the behaviour of everyone in the flock is influenced by either the "best local or best global" individual to help it take a good trajectory in the geographical hyperspace [72]. Furthermore, an individual can learn from its past experiences to adjust its flying speed and direction. For this reason, all the individuals in the flock can quickly converge to the global position and near-optimal geographical position by the behaviour of the flock and their flying histories. This algorithm was implemented in the crystal structure prediction analysis by particle swarm optimization (CALYPSO) code [72] and has been successfully applied to predict several novel materials [72]. It is worthy to note that crystal structure predictions at 0 K as well as high temperature have also been performed using several quantum mechanical methods such as data mining [79], metadynamics [80], basin hopping [81], and simulated annealing [82]. In particular, simulated annealing, basin hopping and metadynamics are used in overcoming energy barriers and have been very successful in many areas especially in cases where the start structure is close to the global minimum. The data mining method depends primarily on the existence of large database of good trial structures and is for this reason unable to generate new crystal structure types without reasonable information on similar compounds. In the past few years, thermodynamic stability and structures of several unprecedented compounds have been successfully predicted without any input from experiment because of the significant advancement in computer power and implementation of various algorithms that have enabled scientists to further explore the emergent of various chemical behaviours especially at high pressure. This chapter gives an elaborate description of all the methods that are often applied in high pressure materials

investigations with case study from research works published from our group to exemplify successful applications where possible.

2.2 Random Structure Search

At a thermodynamic equilibrium, materials are known to take the structures with the lowest possible Gibbs free energy, G defined as:

$$G = U - TS + PV \tag{2.1}$$

where U, T, S, P and V represent the internal energy, temperature, entropy, pressure and volume respectively. In practice, the entropy contribution is ignored and we primarily constrain ourselves to zero temperature so that the Gibbs free energy reduces to the enthalpy, H of the system so that one can write:

$$H = U + PV. \tag{2.2}$$

Thus, a thermodynamic stable state of a material at certain pressure P is that in which the atoms are arranged in such a way to produce the lowest enthalpy. For this reason, to obtain physically realizable crystal structures for any material, it is important to search for stable structures with the lowest possible enthalpy. In this way, the problem of finding stable structures is equivalent to that of global optimization. In other words, suppose the energy of the system could be expressed in terms of some parameters like atomic positions, the stable structures will be those in which these parameters have values that minimize the energy function. Simple as this process may seem, it is quite clear that the energy of a real system cannot be written as a simple analytical function of some parameters. Be that as it may, the solution of any optimization related problem could be evaluated by guessing several possible solutions and then ranking their traits before choosing the best possible solution. This form of guess and check is the fundamental underpin of the random structure search method.

The random search method was introduced for the first time in 1953 by Anderson [68] and

later in 1963 by Rastrigin [69] and Karnopp [83]. If a general detail (such as stoichiometry of the crystal solid) of the system in consideration is known, the random search procedure is to generate several random configurations with different arrangements of atomic components which will be subject to local minimization before calculating the energy. This process can be repeated until a good solution has been obtained. A simple illustration of the procedure is shown below:

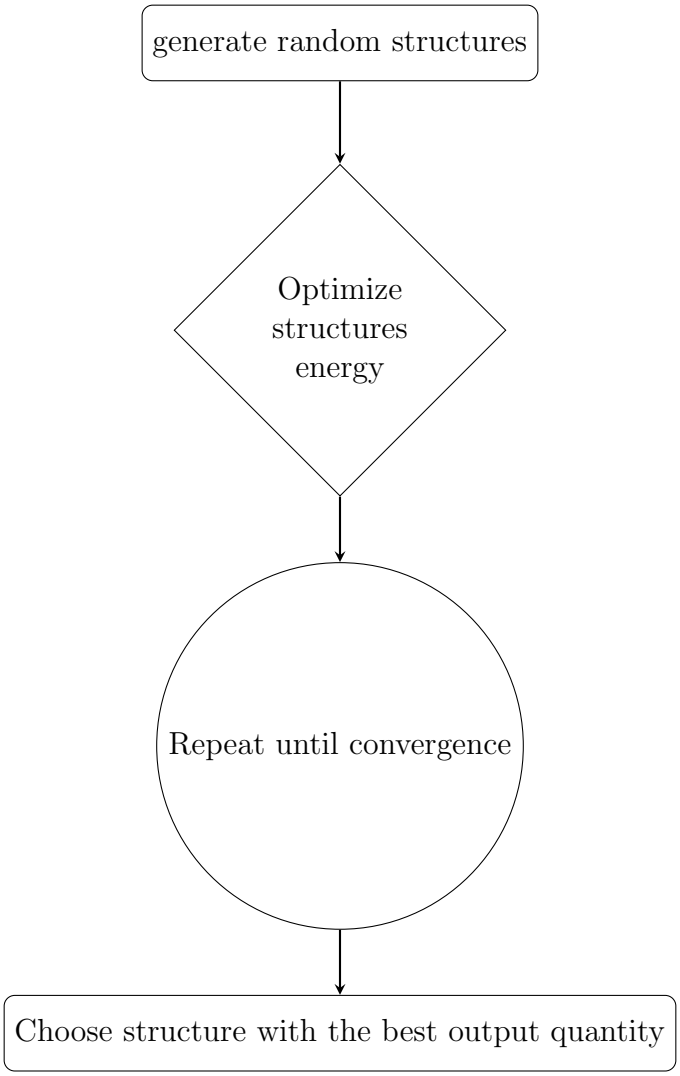

Figure 2.1: A simple random search procedure.

A search is said to have converged when there exist no further improvement to the best trial solution after several iterations and the best solution remains the same for multiple attempts

[84]. To avoid obtaining physically unrealistic solutions, some constraint may be imposed on the parameters of the trail solutions. For example, one could set the minimum and maximum parameters or minimum and maximum interatomic distances in the system to physically reasonable values alone. In recent years, the most significantly used approach to reducing the complexity of the search is performing local relaxation of all trial structures before calculating the energy. Ideally, the energy determines the forces acting on individual atom and moves it down the slope until the system gets to the minimum of the potential energy surface as illustrated in Figure 2.2. In particular, all the commonly used optimization algorithms such as conjugate gradient approach, quasi-Newton method and damped molecular dynamics can easily relax a structure to a nearby local minimum.

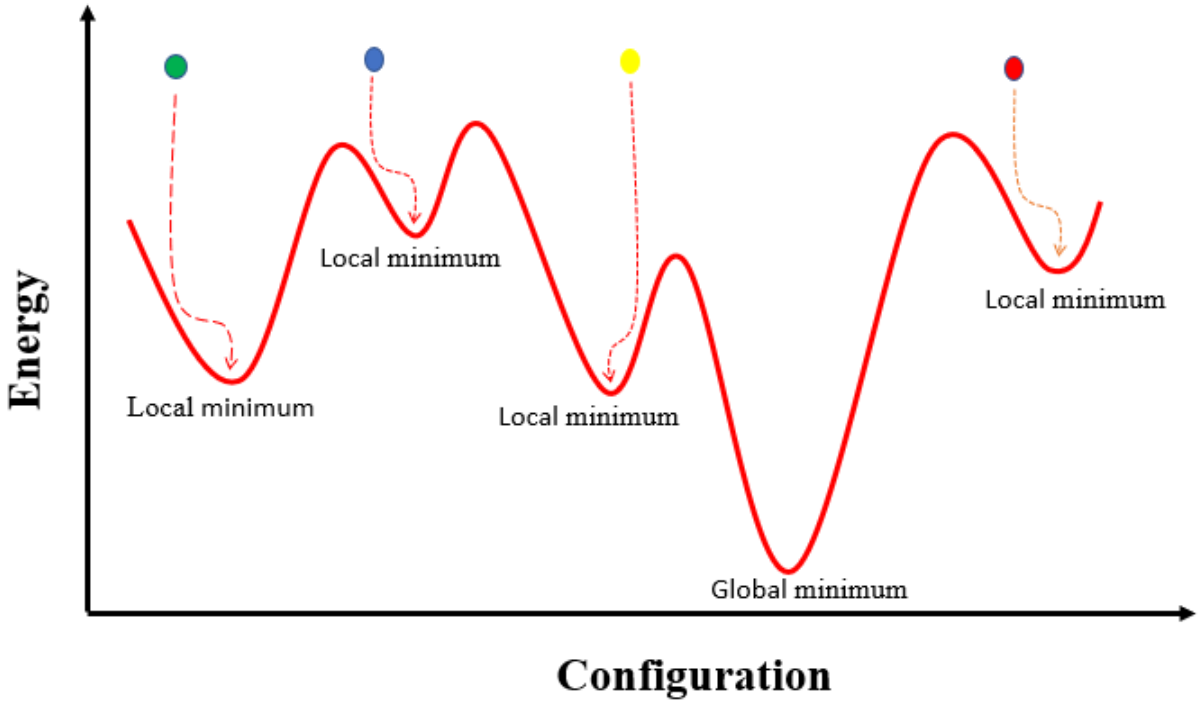

Figure 2.2: Relaxation of structures into local minima in Random Search Method.

In the application of random search procedure to crystal structure prediction, the group of Pickard and Needs have been quite exemplary [85]. Their approach begins as expected with the generation of a number of random configurations which are then optimized in a DFT calculation at constant pressure into a local minimum that corresponds to the minimum energy crystal structure even without any prior knowledge of the structure information except

for possible chemical stoichiometry. After enough preliminaries, a decent testing of the setup space is gotten, and the ground-state structure(s) can be distinguished. By and large, random search based methods have been employed to a high degree of success in the prediction of the ground-state and metastable structures of novel materials such as ice at high pressures [86], atomic metallic hydrogen [87], silane (SiH_4) [88], metal alloys and alloy nanoclusters [89] and several other systems [90, 91, 92, 93].

2.3 Evolutionary/Genetic Algorithm

The evolutionary algorithm takes inspiration from the biological evolution processes which include natural selection, reproduction, mutation and heredity. Solutions to any optimization problem with this method are structures that have gone through these mechanisms within a fitness criteria used to determine the fittest survivors. To begin, one needs to determine an accurate representation of the particular problem, e.g., a correct chemical formula or stoichiometry. Afterwards, the first generation is obtained from optimization of randomly generated structures to produce energetically favourable structures. Thereafter, one discard some of the structures in the first generation with relatively high enthalpy and use the good structures with relatively low enthalpy as parents to create the next generation through a successive cycles of heredity and mutation operations followed by a DFT optimization at constant pressure [94, 95]. The mutation operator often creates a single offspring solution from a single parent whereas the heredity operator produces a single offspring from a few parents solutions. The offspring structures in the second generation can then be used as parents for the creation of the third generation and so on, in a process similar to Darwinian evolution (see Figure 2.3). It is important to point out that at the moment, there is no all in all method that is able to solve a general global minimum problem or locate global optimum solution at all times, and successfully find all exact and accurate ground state at all conditions in all systems. Many of the available methods are for sure able to find several local minima with those solutions often times good enough in most cases. The reasons for this are not far to fetch, for one the potential energy landscape is very complicated and multidimensional and its exact shape or form is somewhat unknown and therefore can only

be approximated at best.

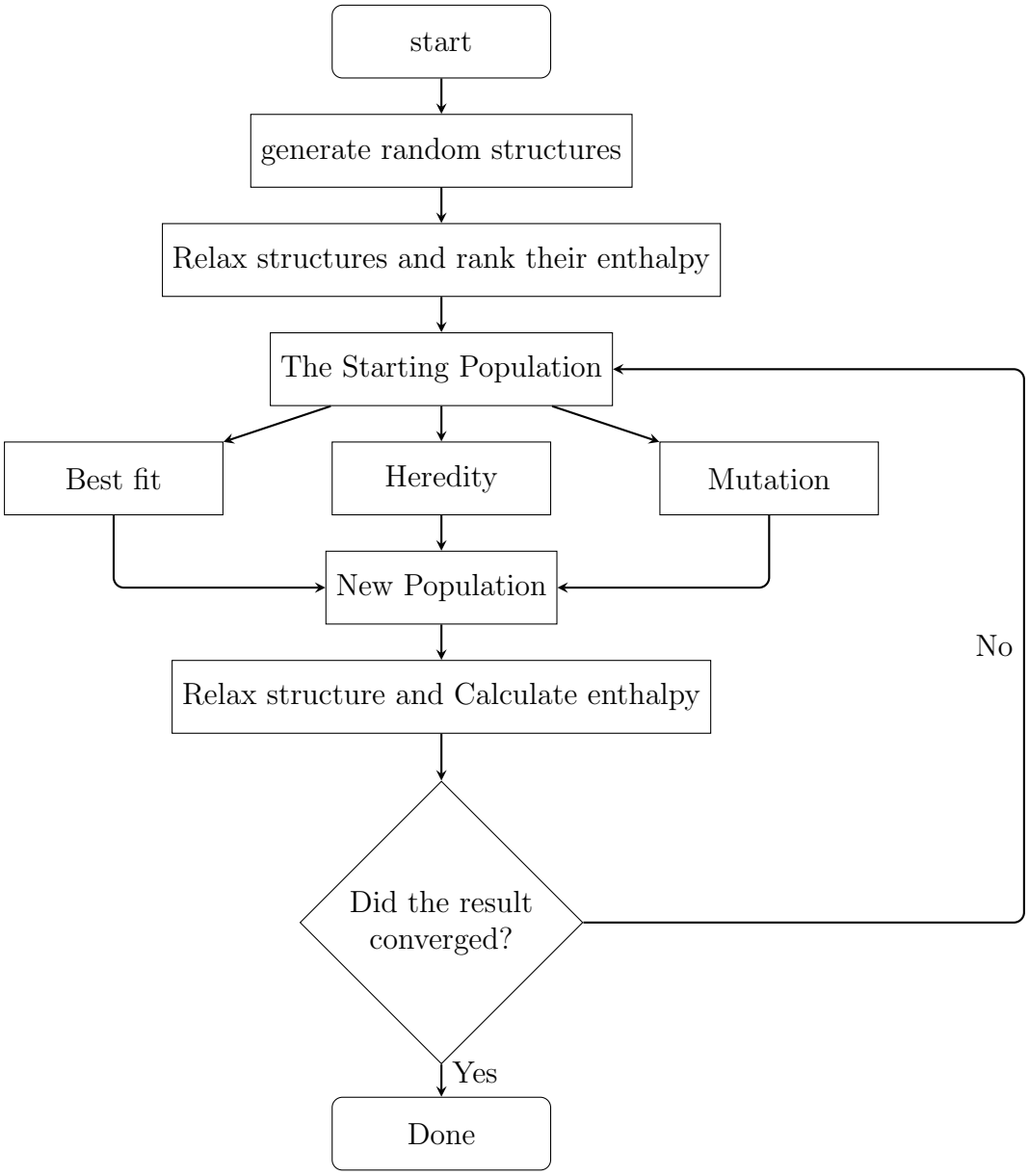

Figure 2.3: The flow chart of a general Evolution Algorithm.

2.3.1 Particle-Swarm Optimization (PSO)

PSO is another kind of evolutionary methods which is quite different from GA. The approach was introduced for the first time by Kennedy and Eberhart [77, 78], and it is motivated by

social behaviour such as bird flocking and fish schooling. An individual in the group relies predominantly on its own experience as well as the experiences of others in the group to know regions in the hyperspace that had been visited and optimum area that may have been explored. Similar to what was done in GA, the system in consideration can begin with a population of randomly generated solutions. However in contrast to GA, each potential solution is given a random velocity $v_{i,j}^t$ and then moved through the configuration space. The velocities and the positions are updated with the following equations:

$$v_{i,j}^{t+1} = \omega v_{i,j}^t + c_1 r_1 (pbest_{i,j}^t - \chi_{i,j}^t) + c_2 r_2 (gbest_i^t, j - \chi_{i,j}^t) \tag{2.3}$$

$$\chi_{i,j}^{t+1} = \chi_{i,j}^t + v_{i,j}^{t+1} \tag{2.4}$$

It must be noted that a potential solution (e.g., a crystal structure) in the phase space of the search is often referred to as a particle in PSO method so that a set of particles can be referred to as a generation. In equation (2.3), the new velocity $v_{i,j}^{t+1}$ of each particle is updated using its own previous velocity $v_{i,j}^t$, previous location ($\chi_{i,j}^t$) as well as the current location where best fitness has been reached ($pbest_{i,j}^t$) and the population global location at which the best fitness has been achieved so far ($gbest_{i,j}^t$). Meanwhile, equation (2.4) is used to bring the position of each particle in the solution hyperspace up to date. The two random numbers r_1 and r_2 are independently generated. The inertia weight ω which takes value between 0.9 to 0.4 has been found very useful in various applications [96]. In predicting stable crystal structures of materials, the implementation of this scheme in crystal structure prediction analysis by particle swarm optimization (CALYPSO) code [72] has led to successful prediction and characterization of numerous materials. The flow chart below illustrate the procedure employed in the CALYPSO code usage.

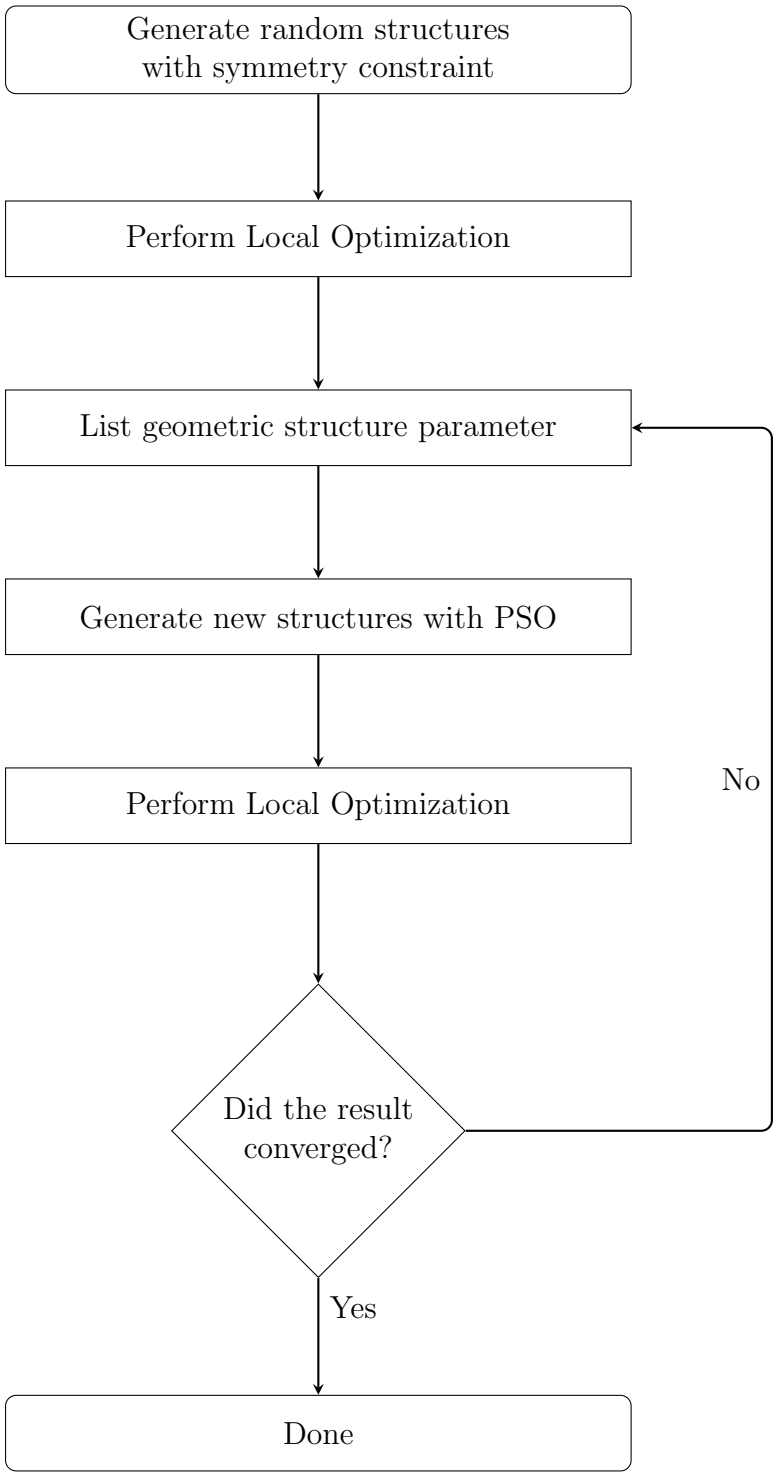

Figure 2.4: A flow chart to illustrate the procedure of CALYPSO code [72].

2.4 Metadynamics

In the transformation of structure from one form to another, crossing a large energy barrier is often required. This has lead to the appearance of several metastable states. This in itself presents a good advantage since structure that otherwise would not form at normal conditions could be created at high pressure and quench recovered at normal conditions. This remarkable procedure has been applied to prepare notable materials with unusual chemical properties. The question of what structure can be formed at a given pressure-temperature conditions can be seen as an optimization problem so that one only need to search for the global minimum of the free energy landscape. It is the underlying approach implemented in various optimization related algorithms such simulated annealing [97], random search [88] and evolutionary search method [94, 95]. After obtaining all candidate structures, one can construct the phase boundaries and thereafter establish a dependable thermodynamic phase diagram. In principle, these optimization techniques attempt to identify the stable structures for a given condition without attempting to elucidate how these structures are formed. Meanwhile metadynamics approach can be very useful in revealing series of microscopic atomistic transformation in the preparation of new materials.

In simulating the structural phase transition in crystals, the metadynamics methods [98, 99, 100] has played a significant role. It is an approach used in escaping free energy minima by exploring free energy surfaces of the Gibbs potential $G(\mathbf{h}) = F(\mathbf{h}) + PV$. Where $\mathbf{h} = (h_{11}, h_{22}, h_{33}, h_{12}, h_{13}, h_{23})$ is the six-dimensional order parameter that define the simulation cell of the crystal structure, $F(\mathbf{h})$ is the Helmholtz free energy, P is the pressure and V is the volume of the system. The free energy is differentiated with respect to the order parameter:

$$-\frac{\partial G}{\partial h_{ij}} = V[\mathbf{h}^{-1}(\mathbf{p} - P)]_{ij} \tag{2.5}$$

where $\mathbf{p}$ is the internal stress tensor that can be calculated at constant h from the microscopic virial tensor [101]. The order parameter is then evolved via a steepest-descent-like discrete

evolution with stepping parameter δh,

$$\mathbf{h}^{t+1} = \mathbf{h}^{t} + \delta h \frac{\phi^{t}}{\mid \phi \mid^{t}}. \tag{2.6}$$

where $\phi^{t} = -\frac{\partial G^{t}}{\partial h}$ is the driving force obtained from a history dependent Gibbs potential G^{t}:

$$G^{t}(\mathbf{h}) = G(\mathbf{h}) + \sum_{t'<t} W e^{-\frac{|h-h^{t'}|^{2}}{2\delta h^{2}}} \tag{2.7}$$

in which a gaussian of width W has been added to $G(\mathbf{h})$ at each visited point $h^{t'}$ to prevent the system from going back to the configurations in the free energy surface that have already been sampled. Thus, ϕ^{t} is the addition of the thermodynamical driving force $\mathbf{F} = -\frac{\partial G}{\partial h}$ and the potential resulting from the superposition of the gaussians. With time, the gaussian fills the initial well of the free energy that represents the starting structure and the system is push from it's local minimum into a new one which represents a new structure [98, 99, 100].

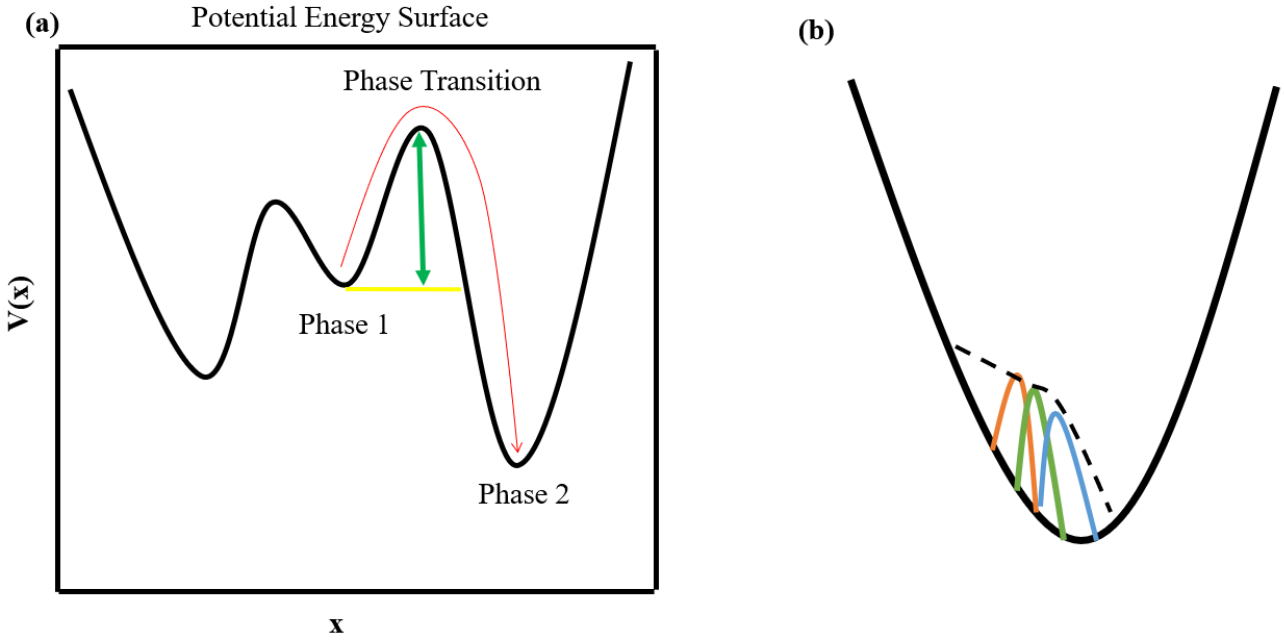

Figure 2.5: (a) An illustration of metadynamics barrier crossing mechanism (b) Gaussians filling the potential well help to overcome the energy barrier.

The metadynamics procedure begins with the calculation of the matrix **h** for the optimized structure at a given temperature and pressure and the evaluation of the stress tensor **p** in

a molecular dynamics run at constant **h** for a period that results in good average of **p**. Equations (2.5) , (2.6) and (2.7) are then used to evolve the box **h** into a new one followed by the equilibration of the particle positions to low energy states to fit the new box using molecular dynamics. In the process of filling the initial free energy well, the box goes through a series of deformations until transition to a new state occurs. The procedure can be repeated to fill the new minimum and move to other available minima.

2.5 Basin Hopping

Structure, dynamics and the thermodynamic properties of materials within Born-Oppenheimer approximation is often described by the potential energy landscape. Finding a stable crystal structure of a particular system is a problem of locating the global minimum on the potential energy landscape describing it. The basin hopping (BH) algorithm described by David Wales and Jonathan Doye is a method tailored to finding the global minimum of a scalar function [81, 102]. In BH, the energy landscape is modified to a group of interconnected staircases with level ground (i.e basin of attraction) that is equivalent to the set of configurations (or set of structures) which lead to a particular minimum after optimization [81]. One should note that despite the transformation, the form of the energy landscape does not change but rather it maps each point to its closest local minimum and therefore essentially depicts the energy landscape in terms of local minima as shown in Figure 2.6. It goes without saying that there exists a reduction in the details between two local minima, albeit, this level of resolution has been observed to work very well particularly in characterizing the structural properties of biological systems such as protein molecules.

The transformed energy is obtained by minimizing the original energy landscape:

$$\widetilde{E}(\mathbf{X}) = min\{E(\mathbf{X})\} \tag{2.8}$$

where $\mathbf{X}$ is the vector of nuclear coordinates in $3N$ dimension with which the energy minimization begins. Previous work have shown that this transformation does not change the

global minimum as well as the relative energies of any local minima [103]. The new form of the energy, $\widetilde{E}(\mathbf{X})$ at a point $\mathbf{X}$ is now the energy of structure produced in minimization so that each local minimum is surrounded by a basin of constant energy which is made from all the nearby configurations from which that specific minimum is derived [104]. It is obvious from Figure 2.6 that the energy barrier has been removed by the new form of the landscape so that the system can now move between these basins in discrete steps. The transformation is now combined with a search mechanisms such as Monte Carlo sampling in which the steps are defined by the perturbation of latest set of coordinates and then performing minimization from the resulting configuration. The condition for a set to be acceptable could be based on either thresholding or implementing a Metropolis step.

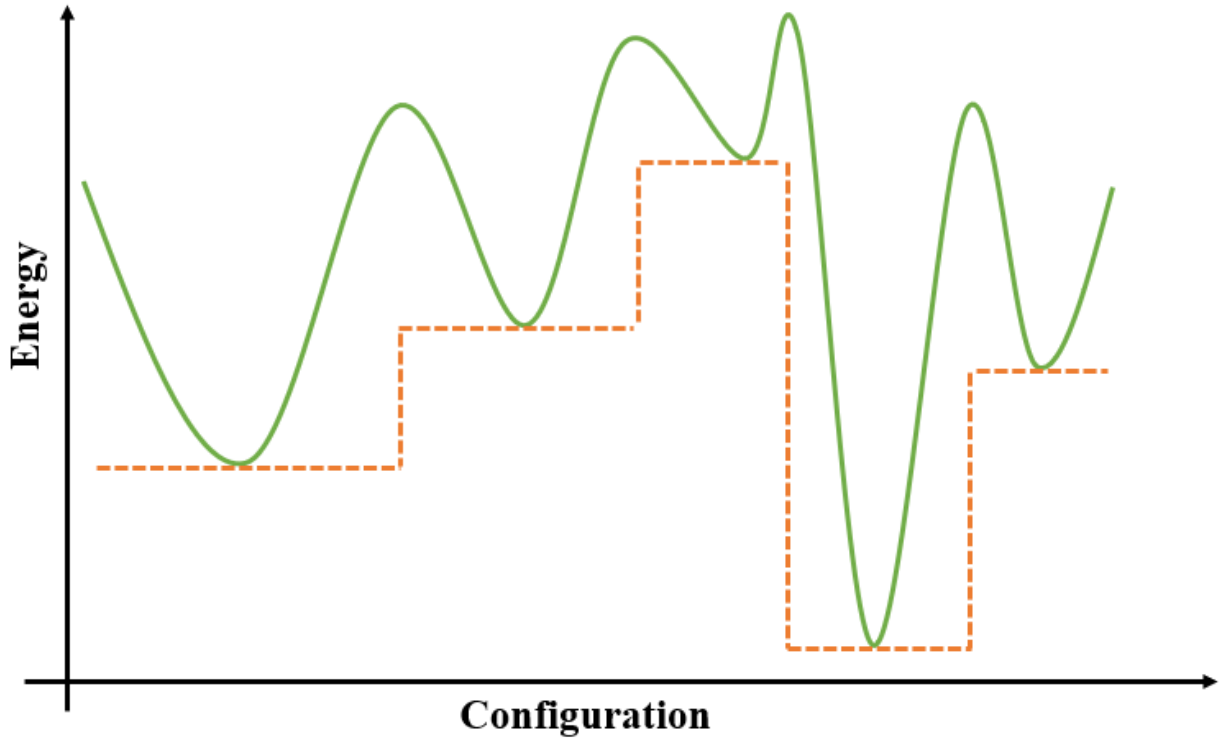

Figure 2.6: An illustration of basin hopping barrier crossing mechanism.

In thresholding, if a new minimum E_{new} is lower than the starting E_{old}, then it will be accepted. Meanwhile in the Metropolis step, the new minimum will be accepted if it is lower that the previous one ($E_{new} < E_{old}$) and if otherwise, then the step is acceptable if the probability $\exp[(E_{old} - E_{new})/kT]$ is greater than a random number drawn from the interval of 0 to 1 [103, 104]. It must be noted that the temperature T is an adjustable parameter

which is not used for annealing. In a nutshell, the procedure in basin hopping is an iterative cycle that begins with a random perturbation of coordinates followed by a local minimization after which the new coordinates or configurations are either accepted or rejected based on a minimized function value [102].

2.6 Simulated Annealing

Simulated annealing (SA) is an approach that is motivated by the physical annealing in which a matter is heated above its recrystallization temperature and then allowed to maintain the desired temperature for some time before cooling [82]. The cooling process has to be controlled in order to maximize the size of crystals formed and also reduce any defect incurred. For example, heating a metallic material such as Copper above its recrystallization temperature and allowing it to melt make the atoms become disordered in nature [105]. However, when cooled slowly from the molten state, the atoms may crystallize orderly and the energy may reach its global minimum. If otherwise cooled rapidly, it could become an amorphous solid or a crystal with notable defects such as vacancies and dislocations. Therefore, the SA process begins by melting the system at a highly acceptable temperature and then slowly reducing its temperature until the system gets to a steady state where no further changes can be observed. During the run, at each temperature, the atoms undergo series of movements and rearrangements either by molecular dynamics or Monte Carlo process during which the simulation is permitted to proceed for a time long enough to allow it get to a steady state [106]. Consider a current state of the system which is characterized by the positions of its particles, suppose one then introduces a small random perturbation say by displacing a random particle. If the energy (E) of this perturbed state is lower that the current state (i.e $\Delta E < 0$), then the process is continued with the new state. If not (i.e $\Delta E \geq 0$), the probability of accepting the perturbed state will be $\exp(-\frac{\Delta E}{k_B T})$ according to the Metropolis criterion [107]. Repeating this process slowly enough could lead to a final state likely to be the global minimum of the system.

2.7 Application Examples

As have earlier discussed, there are several optimization related methods that can be applied to locate local minimum as well as global optimum in theoretical crystal structure investigations. In this work, we applied the random structure search [88], genetic algorithm (GA) [94, 95] and metadynamics [98, 99, 100]. The following are cases where these methods have been successfully applied to characterize interesting materials.

2.7.1 Pressure-induced structural transformations and new polymorphs in $BiVO_4$

Bismuth vanadate ($BiVO_4$) has been well discussed for its application in photo-catalysis. It is known to have various structures including tetragonal zircon structure (tz-$BiVO_4$ $I4_1/amd$), monoclinic fergusonite structure (mf-$BiVO_4$ I2/a), and tetragonal scheelite structure (ts-$BiVO_4$ $I4_1/a$) with each of them showing different level of photo-catalytic activity. This indicates that the properties of $BiVO_4$ depends enormously on its crystal structure. To explore the structural stability and likely transition between structures in material science, high pressure has long been known as an important tool. At ambient pressure, unlike most orthovanadate compounds that crystallize in either $I4_1/amd$ or $I4_1/a$ phase, $BiVO_4$ takes the I2/a structure. Hence, it may undergo a different phase transition and properties when subjected to high pressure. In 2018, Pellicer-Porres et al. [108] reported that both fergusonite and zircon-type $BiVO_4$ transform to the scheelite structure phase and then to an unidentified phase at high pressure. The reversible transition from fergusonite to scheelite and scheelite to the new phase was observed at 3.2 GPa and 15.0 GPa pressure respectively. Meanwhile, an irreversible zircon to scheelite transition begins at about 1.3 GPa and completes at about 5 GPa with the second reversible transition from scheelite to the new phase starting around 15 GPa as well. Until now, this new high pressure phase has yet to be characterized and explained, hence the motivation for this work.

In order to identify this new high pressure phase, first principles metadynamics simulations

were applied. The simulations were done on a 2 ×2× 2 supercell of scheelite-$BiVO_4$ at room temperature (300 K) and at four different pressure conditions between 25-40 GPa at 5 GPa interval. As often done in metadynamics simulations, it is important to over-pressurize the system in order to speed up the transition. At 30 GPa, a transition to a completely new C2/c phase occurred. A careful comparison with other known structures in literature indicates that the C2/c phase is an isostructure to a β-fergusonite structure which had been seen in $ZnVO_4$ previously at high pressure. A pictorial representation of the phase transition is show in Figure 2.7.

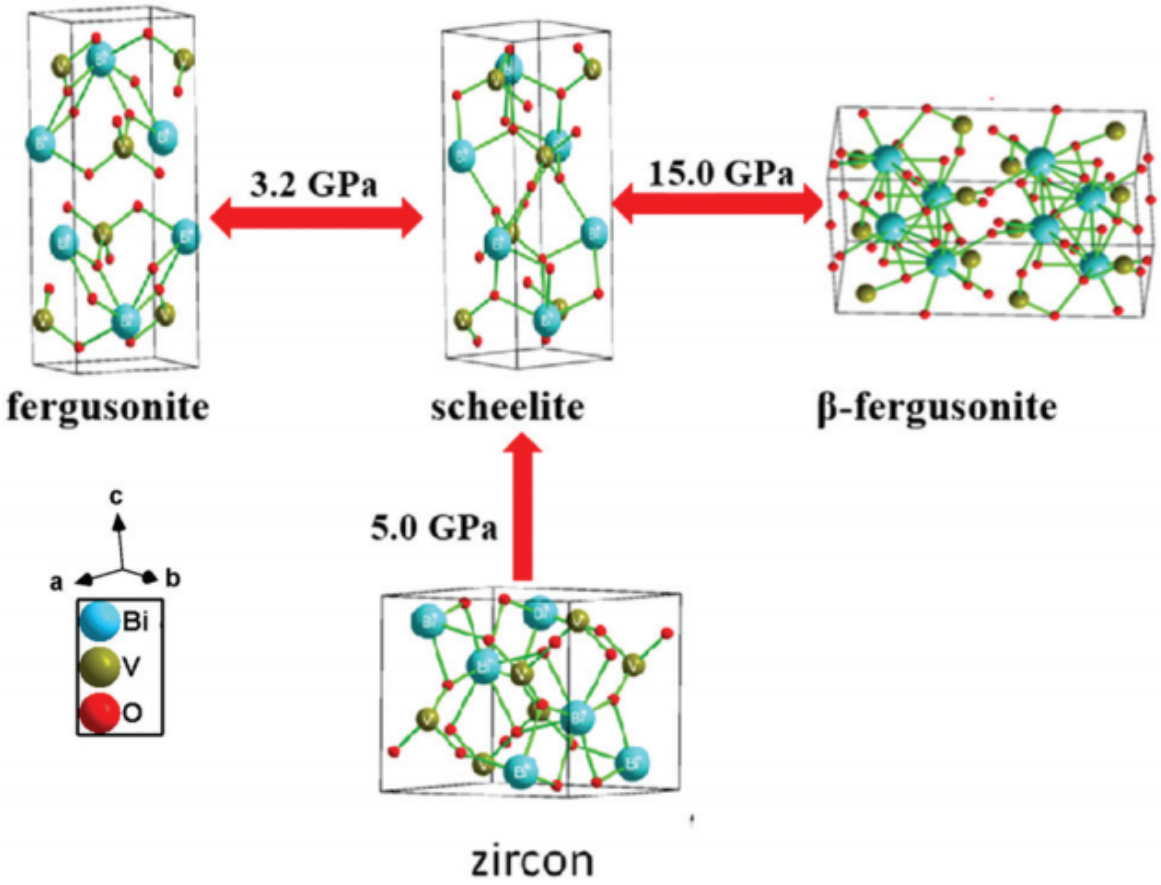

Figure 2.7: Schematic model for the phase transition of $BiVO_4$ upon compression [109].

Interestingly, metadynamics simulation at 30 GPa also shows that this β-fergusonite structure further transforms to another Cmca phase that has so far not been reported in any orthovanadate compound. Phonon dispersion analysis (see Figures 2.8 and 2.9) performed

on both β-fergusonite and Cmca structures at 30 and 40 GPa respectively shows no negative value, suggesting that they are dynamically stable. For this reason, it is safe to project that β-fergusonite structure of $BiVO_4$ may transit to Cmca phase at high pressure [109].

The pressure stimulated transitions in the compound were explored with metadynamics [80, 100] in addition to the projector augmented plane wave method which has been implemented in VASP. The Bi, V, and O potentials employ $5d^{10}6s^26p^3$, $3s^2$ $3p^63d^34s^2$, and $2s^22p^4$ as valence states with the Perdew–Burke–Ernzerhof (PBE) functional , respectively. The plane wave basis set was expanded with a kinetic energy cutoff of 500 eV and a dense k-point grid with spacing of $2\pi\times$ 0.03 Å^{-1}. At each metastep, first principles molecular dynamics (MD) simulation with canonical ensemble was done for 0.4ps. To quicken barrier crossing, the supercell was over-pressurized under both hydrostatic and nonhydrostatic conditions. Phonon dispersion relations were calculated using the density functional perturbation theory and post processed using the PHONOPY code [61].

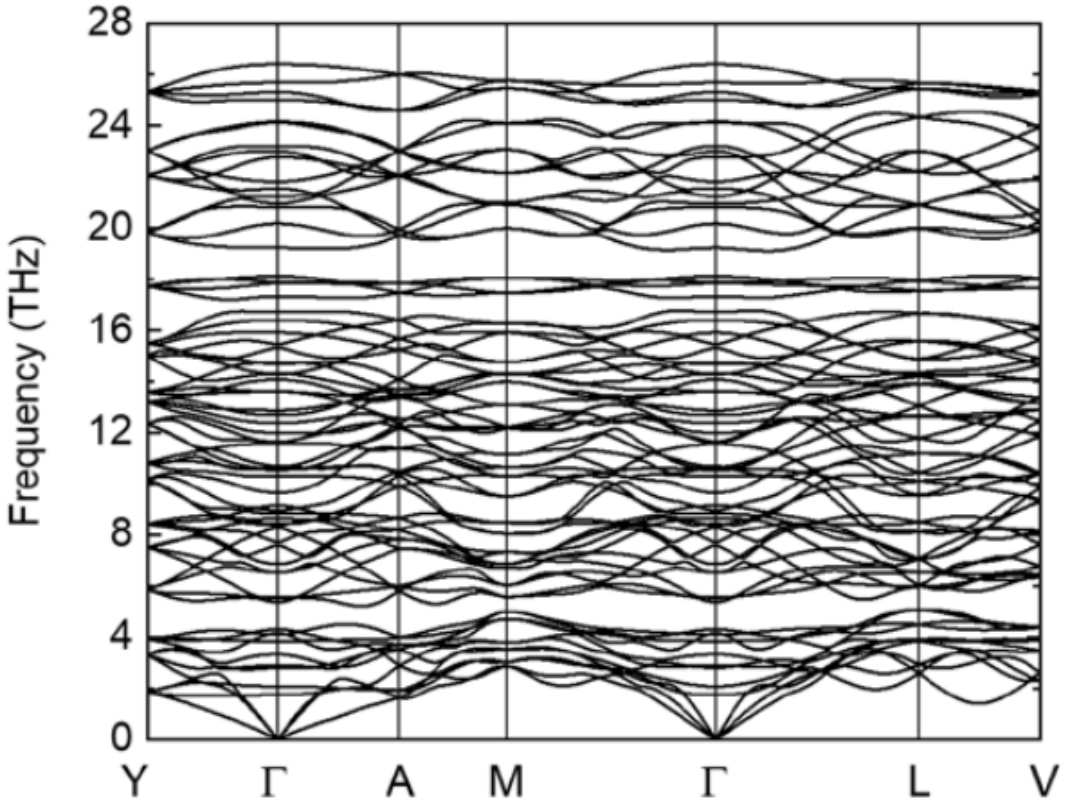

Figure 2.8: Calculated phonon dispersion relations for β-fergusonite structure at 30 GPa [109].

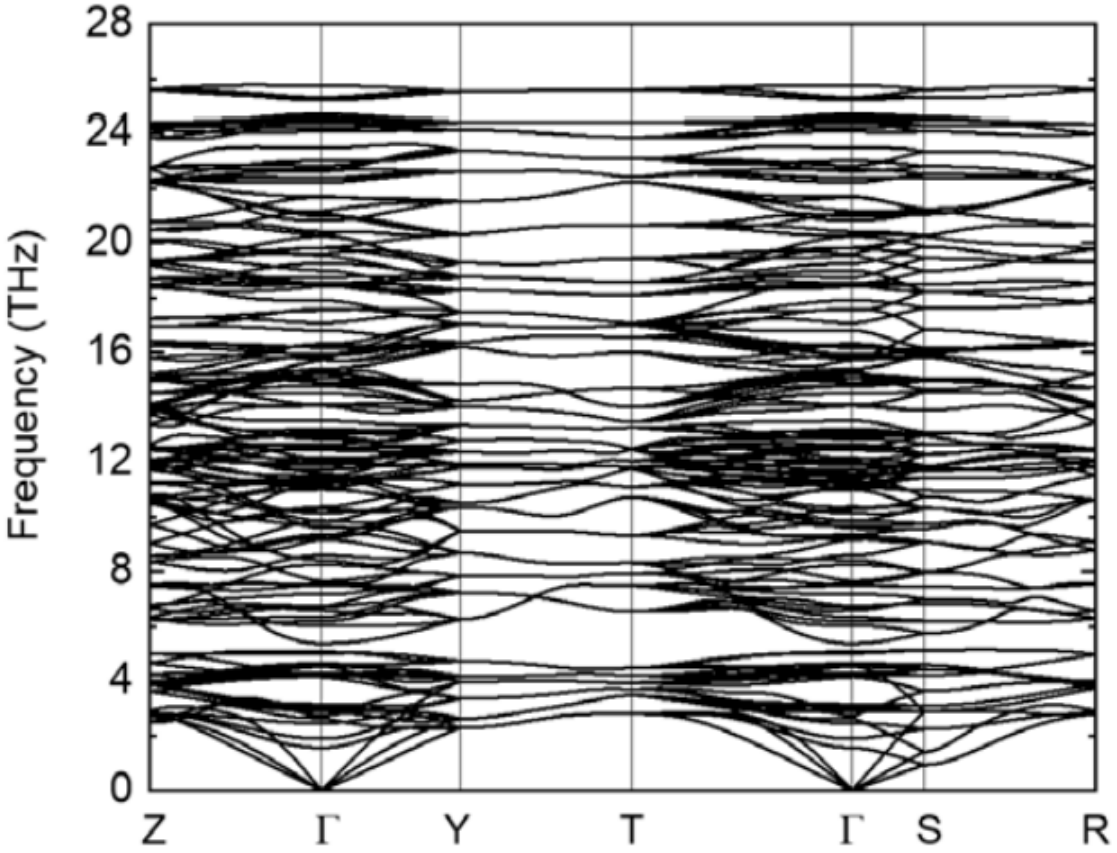

Figure 2.9: Calculated phonon dispersion relations for the Cmca structure at 40 GPa [109].

2.7.2 o-C_{240}: A New sp^3-dominated allotrope of carbon

Carbon is one of the most basic elements in nature with several industrial applications. It can exist in many forms including amorphous carbon, diamond, graphite and fullerene as well as numerous metastable phases. A lot of theoretical and experimental investigations have been directed towards finding carbon structures with special properties such as ultra high density, super hardness and stability [110, 111, 112]. The application of external stimuli such as pressure and temperature can be used to create these new allotropes of carbon. Very often, the process entails the modification of carbon bonding environment in an already known allotrope. For instance, with heat treatment, C_{60} filled single-wall carbon nano-tube (CNT) have been shown to transform to carbon nano-tube with double-wall [110]. Meanwhile solid C_{60} has be reported to change to polymerized phases of crystalline carbon dominated by sp^3 and sp^2 hybridized carbon at high pressure and temperature [111]. Of a notable interest is the conversion of carbon onions to diamond with the application of a controlled nano-twinning in which the resulting diamond shows a high level of hardness compared with natural diamond [112].

Allotropes of carbon that contain mixture of sp^3 and sp^2 hybridized C atoms have been reported to show some fascinating properties including ultra hardness and strength that make them very usable in device fabrication. For this reason, several attempts have been made to synthesize mixed sp^3/sp^2 compounds of carbon including CNTs [113] and fullerene [114]. A combination of experimental and theoretical studies revealed that buckminsterfullerene (C_{60}) can polymerize under pressure with a large existence of both sp^3 and sp^2 bonds in the resulting polymer [115]. Clathrates of carbon have also been reported to demonstrate considerable strength despite having a low density [116].

In spite of the notable success, designing new allotropes of carbon from just experiment is time consuming and costly since such processes will involve countless number of attempts and trails. Consequently, theoretical structure search investigations become very useful since they can identify potentially synthesizable new allotropes and therefore guide further experimen-

tal explorations. In this work, a new allotrope of carbon was predicted from metadynamics and first principles calculations. It is formed from a conversion of 2D polymeric C_{60} at high pressure and temperature. An orthorhombic (Immm) 2D polymeric C_{60} was compressed at 40 GPa and heated to 1500 K in a metadynamics simulation. After the conversion, C_{60} significantly lost its identity, fusing into a 3D structure with new bonds formed within the starting C_{60} through sp^3 hybridization. This new compound (shown in Figure 2.10) is named o-C_{240} because it has 240 atoms in a unit cell of a primitive orthorhombic (Pmmm) space group [117]. Interestingly, the ratio of sp^2/sp^3 changed significantly from 52:8 in the starting C_{60} to 9:51 in the o-C_{240} compound. Dynamical stability of o-C_{240} explored at 0 GPa as shown in Figure 2.11 indicates that it is dynamically stable and therefore quench recoverable after its synthesis at high pressure-temperature conditions. With respect to electronic properties, the computed electronic band structure at ambient conditions (see figure 2.12(a)) shows that o-C_{240} is a semiconductor of an indirect energy gap of about 1.72 eV. Projected electron density of states in Figure 2.12(b)) indicates that the carbon p-states is at the valence band maximum (VBM) and the conduction band minimum (CBM) for the o-C_{240}.

The new allotrope is calculated to have optimum fracture toughness and to be superhard with a calculated Vickers hardness of about 45 GPa which is close to or even more than that of some known superhard materials including B_4C (38 GPa) [118], B_6O (45 GPa) [119], and WB_5 (45 GPa) [120]. This high value of hardness is not surprising due to the appearance of both sp^2 and sp^3 carbons in the o-C_{240}, since there exists a dependable correlation between the hardness of a carbon allotrope and the sp^2 /sp^3 ratio. The 9:51 sp^2 /sp^3 ratio makes o-C_{240} a superhard material while maintaining a semiconducting state, which could potentially find significant applications in industry [117].

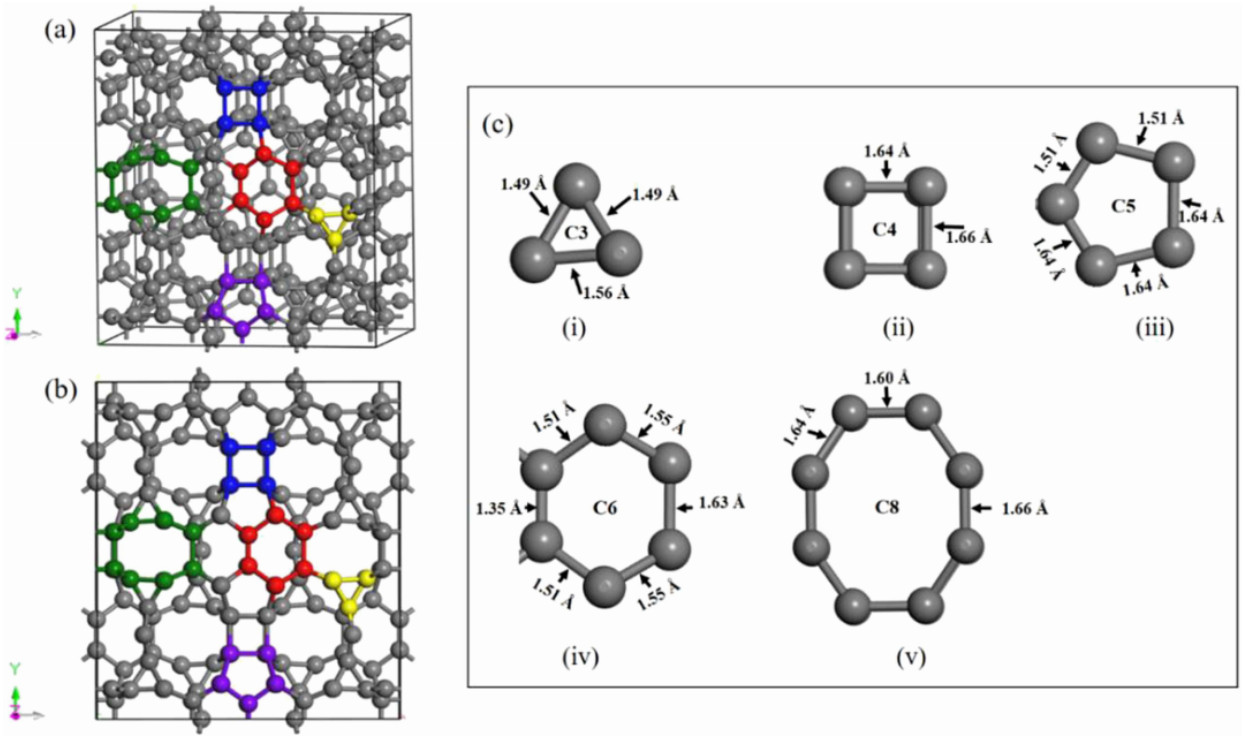

Figure 2.10: The unit cell of the o-C_{240} compound shown in (a) three-dimension and (b) two-dimension as well as (c) unique carbon rings that characterize the structure at 0 GPa [117].

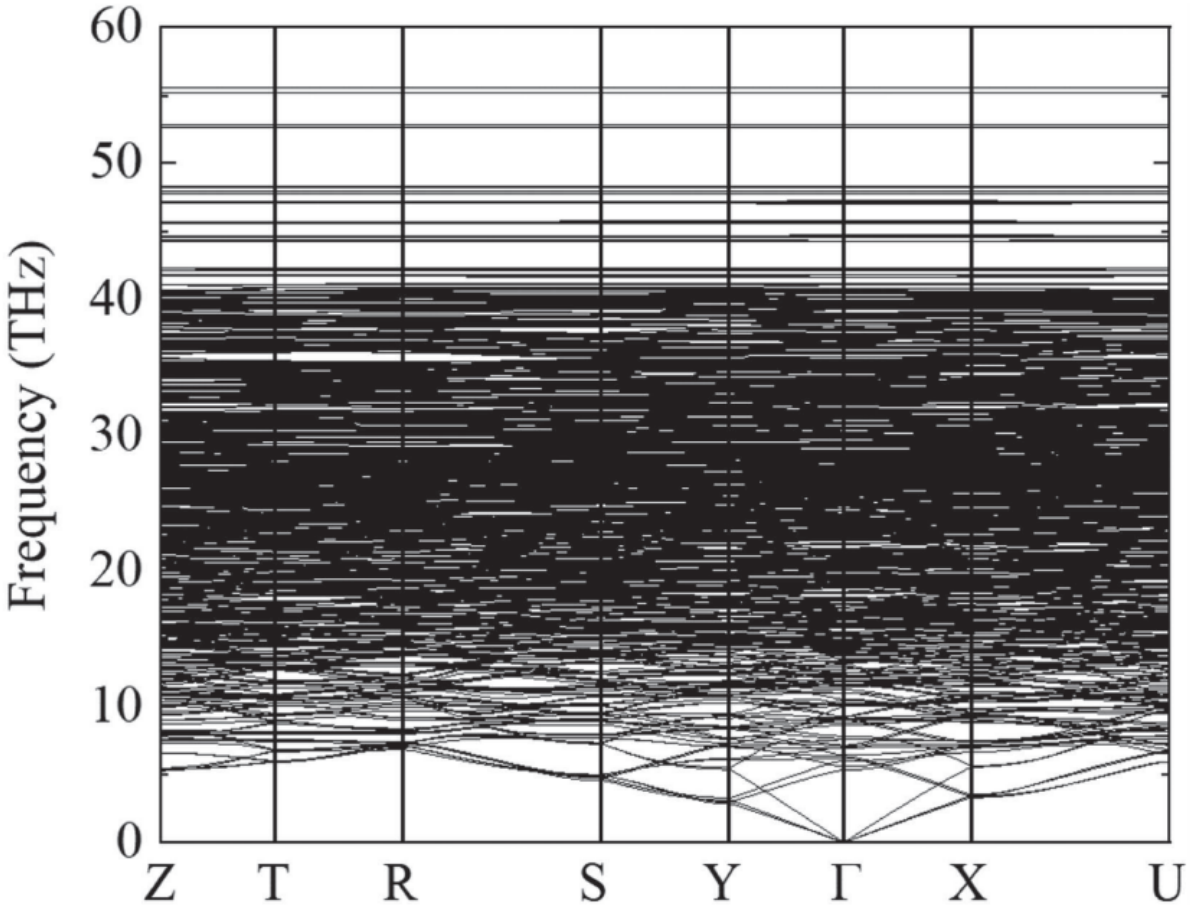

Figure 2.11: Calculated phonon dispersion relation for o-C_{240} compound at 0 GPa [117].

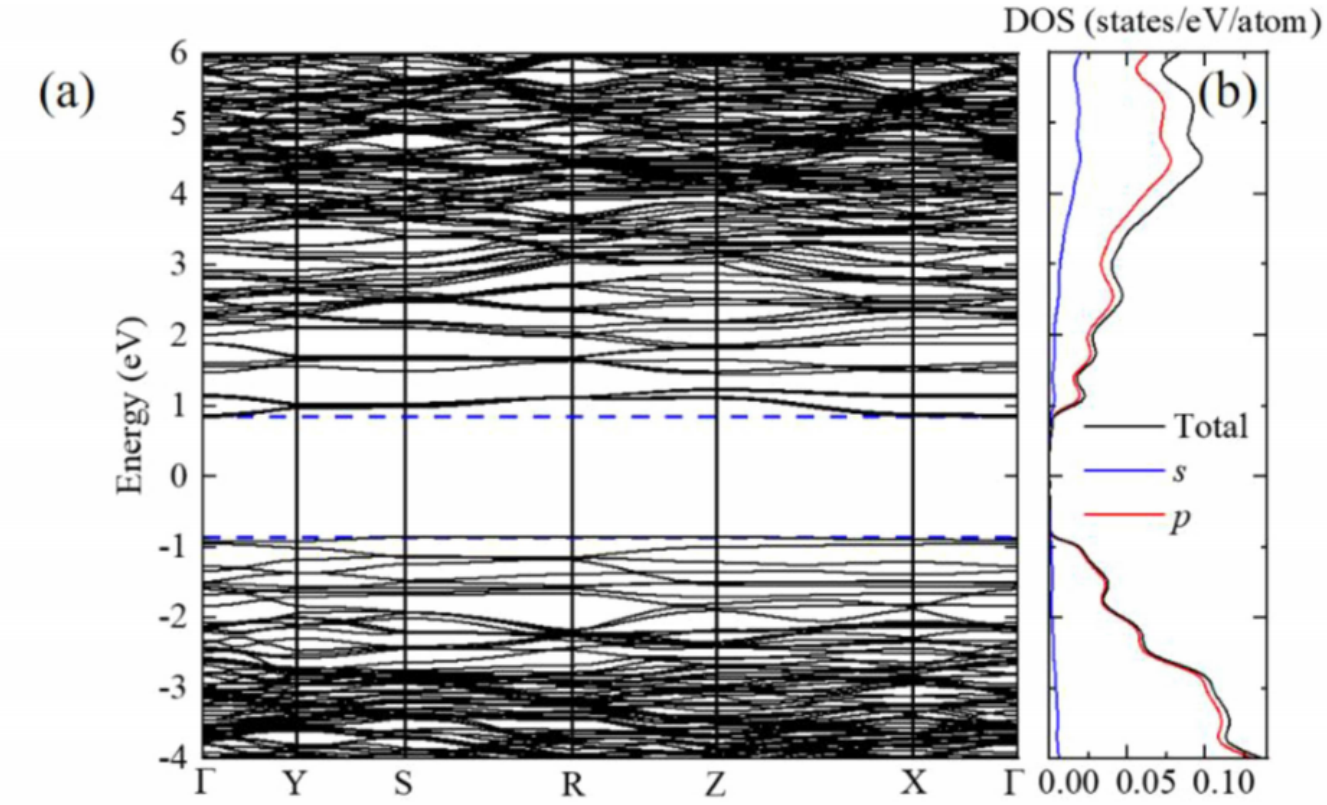

Figure 2.12: (a) Calculated electronic band structure of o-C_{240}. (b) Total and projected electronic density of states of o-C_{240} [117].

2.7.3 Two good metals make a semiconductor: A potassium-nickel compound under pressure

Properties of materials can undergo a significant change at elevated pressure and temperature. For instance, at ambient conditions, alkali metals are known to have a very simple electronic band structures that can be described by a nearly free-electron model. However with increasing pressure, they undergo series of structural phase transitions from a very well symmetric body-centered cubic metallic phase to other phases accompanied with a decrease in symmetry. Moreover, heavy alkali metals such as potassium (K), rubidium (Rb) and caesium (Cs) upon compression can experience a transition from s electronic configuration to d state in which case the s-d transition enables them to behave like transition metals [121]. Chemical reactions that are not achievable at ambient conditions can even be triggered at high pres-

sure as a result of breaking of bonds and formation of new ones leading to the appearance of unprecedented compounds with unique properties. One of such remarkable compound formation between K and Ni had been synthesized above 30 GPa [121]. This effect of pressure on the reaction of alkali metal with transition metal has its foundation in Miedema's rule [122]. According to this rule, a small difference in charge density at the Wigner-Seitz radius and a large difference in the electronegativity between two metals support the formation of compound [122]. The electronegativity of alkali metals are quite different from those of transition metals so this part of the rule is easily satisfied. Nonetheless, there is a huge difference in the charge densities of the alkali metals and those of transition elements. The differences in charge density between them are too large to readily allow compound formation at ambient conditions. At high pressure, the charge densities of alkali metals grow faster than those of the transition metals because of the s-to-d transition leading to the formation of compounds between them.

A little above two decades ago, Parker et al. successfully synthesized a crystalline compound of K and Ni at about 2500 K above 30 GPa but not able to pinpoint the exact crystallography of the observed structure [121]. In this work, a combination of GA and PSO have been applied to explore the potential energy surface of K-Ni. The search was done at 0 and 37 GPa which is the pressure at which a compound of K-Ni was synthesized. Simulation cells of up to four K_xNi_y formula units were employed. Structure optimization, total-energy calculation, and molecular dynamics (MD) simulation were performed using the Vienna ab initio simulation package (VASP) [21] and projector-augmented wave (PAW) potentials [20, 123] with the Perdew-Burke-Ernzerhof (PBE) functional [124]. The K and Ni potentials used have valence states of $3s^23p^64s^1$ and $3s^23p^63d^84s^2$, respectively, and an energy cutoff of 450 eV. A k spacing of $2\pi \times 0.02$ Å was used for Brillouin zone (BZ) sampling.

The convex hull computed at 37 GPa shows that there exists a good number of compounds with several stoichiometries that are thermodynamically accessible on the energy surface of K-Ni systems (see Figure 2.13 (a)). After comparing the x-ray diffraction pattern of all predicted compounds with the experimentally obtained pattern, a particular $P2_1/m$ K_2Ni

turns out to be a good match as shown in Figure 2.13 (b). One very interesting property of this $P2_1/m-K_2Ni$ is that its electronic band structure shows that it is a semiconductor with energy band gap of about 0.65 eV despite the fact that both K and Ni are metals. The formation and synthesis of this compound is a confirmation that K can be incorporated with Ni at high-pressure conditions. It is important for understanding the partition of trace elements between the core and mantle, a key problem in the evolution of Earth. This study will provide insight for understanding the partition of trace elements between the Earth's core and the mantle, a key problem in getting a full grasp of Earth's evolution [39].

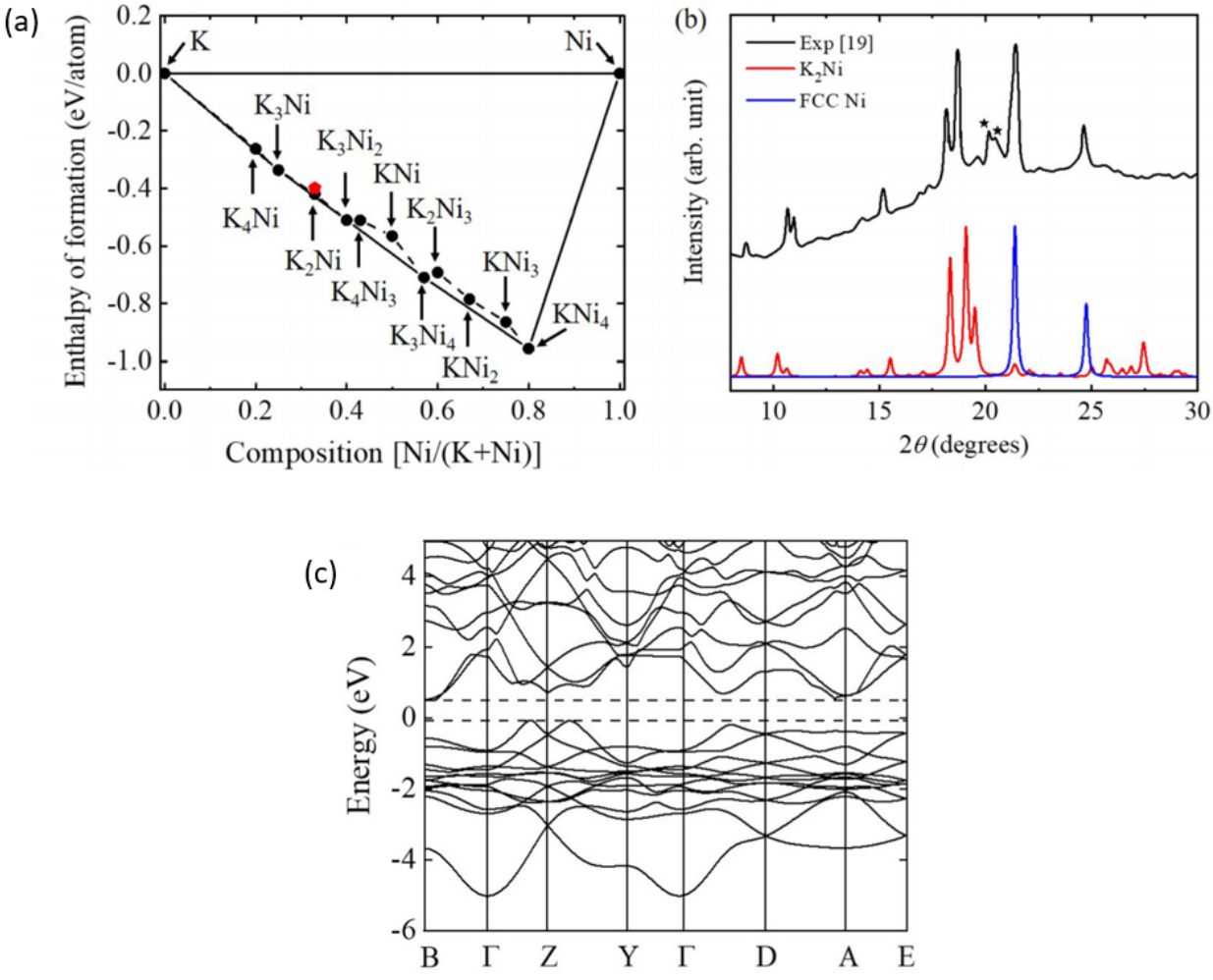

Figure 2.13: (a) Enthalpy of formation of various K-Ni compounds with respect to constituent elemental decomposition at 37 GPa.(The red dot was obtained from GA, all other points are from PSO) (b) Calculated XRD patterns for the $P2_1/m$-K_2Ni and the fcc-Ni at 37 GPa, compared with the previous reported experimental XRD pattern at the same pressure. (c)Electronic band structure of $P2_1/m$-K_2Ni at 37 GPa [39].

Chapter 3

HIGH-ENTHALPY CRYSTALLINE PHASES OF CADMIUM TELLURIDE

This chapter is a slight modification of the paper that had been published in Physical Review Research. The reference to the published work is as shown below:

- **Adeniyi, A. O.,** Kunz, M., Stavrou, E., Yao, Y. High-enthalpy crystalline phases of cadmium telluride. Physical Review Research, 2(3), 033072.(2020).

3.1 Introduction

Groups IIB-VIA compounds have attracted research interest for many decades from both experimentalists and theorists due to their wide applications that include light-emitting diodes, laser diodes, chemical sensors, field-effect transistors, catalysis, and solar cells. The behaviour of these compounds at high presure has also been explored for about three decades. At high pressure, fascinating physical and chemical properties of these materials develop, for instance their electronic properties may change from that of a semiconductor to metallic [125, 126]. Both experimental and theoretical studies have shown that the widely acceptable transition path for these compounds is zinc-blende (ZB) or wurtzite (WZ) $\rightarrow$ NaCl $\rightarrow$ Cmcm with increase in pressure [87, 127, 128]. Like the other IIB-VIA binary compounds, cadmium telluride (CdTe) has found many applications especially in highly efficient optoelectronic devices. It is a direct-bandgap semiconducting material with a bandgap value matching almost perfectly to the solar spectrum [129, 130]. This trait makes CdTe an optimal material for low-cost high-efficient photovoltaics (PV) applications. Current state-of-the-art CdTe-based single junction devices can reach a conversion efficiency as high as 22%, providing a

low-cost alternative to conventional silicon-based devices [131]. Moreover, doped CdTe and variants have numerous applications in thermoelectrics, ferroelectrics, and quantum dots [132, 133, 134]. Driven by its versatile applications, the study on CdTe is currently very active. Since, the properties of CdTe are closely tied to its crystal structure, understanding the latter and its changes under external stimuli is a key step to developing new applications.

At ambient conditions, CdTe crystallizes in a semiconducting zincblende structure which is a commonly adopted structure for group II-VI binary binary compounds. About 3.5 GPa, it is known to transform into a semimetallic rocksalt structure through an intermediate cinnabar structure which has a very narrow region of stability. Nelmes et al. reported a further transformation of the rocksalt phase (B1) of CdTe to an orthorhombic Cmcm phase at about 10 GPa [127]. The Cmcm phase remains stable to about 40 GPa [127, 135] before undergoing further pressure induced phase transition at about 42 GPa to an unidentified phase. Up until now, the structure of the post-Cmcm phase of CdTe has so far been unresolved. Theoretical calculations with density functional theory have been applied to successfully reproduce the transition sequence zinc-blende $\rightarrow$ cinnabar $\rightarrow$ rocksalt $\rightarrow$ Cmcm [136, 137]. Interestingly, the Cmcm phase was predicted to transform a new phase at about 44 GPa which is close to the experimental transition pressure [136]. However the simulated diffraction pattern of the predicted P-3m1 structure does not match the x-ray diffraction pattern of the post-Cmcm phase. Moreover, DFT calculation shows that the enthalpy of CdTe should become higher than that of its elemental constituents (Cd and Te) at 34 GPa, indicating that CdTe may actually undergo an elemental dissociation in this pressure neighborhood.

Up to the present time, the post-Cmcm phase of CdTe remains unknown and the predicted dissociation in this pressure neighborhood adds to the mystery. To address this problem and understand the mechanisms underlying the interesting phase transitions, a detailed synchrotron XRD (done by Dr. Stavrou at the Lawrence Livermore National Laboratory, Livermore, California) and first principles computational study (by me under the supervision of Dr. Yao) of CdTe in the rocksalt to post-Cmcm regions (6 – 63 GPa) are performed. The experiment successfully reproduces the rocksalt to Cmcm transition at 10.5 GPa and

the Cmcm to post-Cmcm transition at 42 GPa. The measured XRD pattern for the post-Cmcm phase agrees very well with the previously reported pattern [135]. A metadynamics simulation is used to successfully identify the structure of this phase as a monoclinic $P2_1/m$ structure. The calculations further reveals that $P2_1/m$ structure is a distorted form of the B11 structure (P4/nmm) and can be viewed as an intermediate phase for the Cmcm to B11 transition in a broader pressure range. Consistent with previous reports, both $P2_1/m$ and B11 structures are found to have higher enthalpies than their elemental constituents. This extraordinary phenomenon is attributed to a significant kinetic energy barrier separating crystalline CdTe from elemental phases in composition space [138].

3.2 Computational Methods

The calculations in this work was done using the density functional theory [4] by solving the Kohn-Sham equations [10]. Vienna ab initio simulation software package (VASP) [21] was used for the structure optimization, calculation of the pressure-volume relation as well as the enthalpy, band structure and the density of states. The projector augmented planewave (PAW) [20, 123] pseudopotential combined with the Perdew-Burke-Ernzerhof (PBE) exchange-correlation functional [124] and a kinetic energy cut off of 650 eV was used with Cd and Te taking $4s^2 4p^6 4d^{10} 5s^2$ and $5s^2 5p^4$ as valence states respectively. Phonon dispersion curve was calculated using the Quantum ESPRESSO (QE) code [57, 58] with kinetic energy cut off of 75 Rydberg. A 4 X 4 X 4 q-point grid was applied for the phonon calculation and the dynamical matrix. To simulate the phase transition, metadynamics simulations were performed starting with several supercells of Cmcm phase consisting 8 - 32 CdTe formula units (f.u) at 300 K and pressure in the range of 50 - 120 GPa. Each metastep involves molecular dynamics simulation with a canonical ensemble (NVT) for 0.8 ps.

3.3 Results and Discussion

x-ray diffraction experiment performed by Dr Stavrou at Lawrence Livermore National Laboratory revealed the transition of CdTe from the rocksalt structure to Cmcm and from the

Cmcm structure to an unknown structure at high pressure (see Figure 3.1).

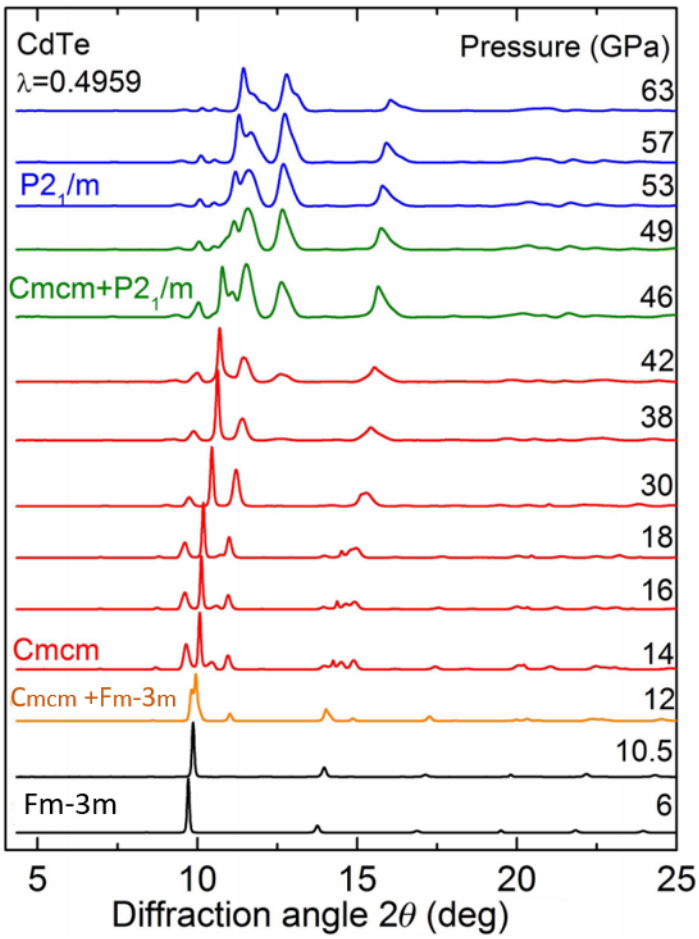

Figure 3.1: Experimental XRD patterns of CdTe at various pressures measured on pressure increase. The XRD patterns of the rocksalt (Fm-3m), Cmcm, and post-Cmcm phases are shown by black, red, and blue lines, respectively. The XRD patterns of mixtures of Cmcm and rocksalt and of Cmcm and post-Cmcm ($P2_1/m$) phases are shown by yellow and green lines, respectively.(The Figure was produced by Dr Stavrou) [138].

At low pressure in the range 6 - 10.5 GPa, the diffraction pattern is consistent with the rocksalt (Fm-3m). The first phase transition occurs at about 12 GPa to a structure that has a diffraction pattern that agrees with previously reported Cmcm phase. This structure is stable to about 42 GPa at least, before transforming to another phase that has not been previously solved.

3.3.1 Structure Determination

In order to identity the unknown high pressure phase, metadynamics simulation was used to explore the potential energy surface of CdTe. The simulation uses the scaled components of the edge vectors of the simulation cell as the collective variables. The simulation was carried out in a vast pressure region, from 50 to 120 GPa, to capture as many phase transitions. At 90 GPa for instance, evolution of the collective variables (Figure 3.2) as well as the enthalpy (Figure 3.3) indicate a clear phase transition at the 35^{th} metastep.

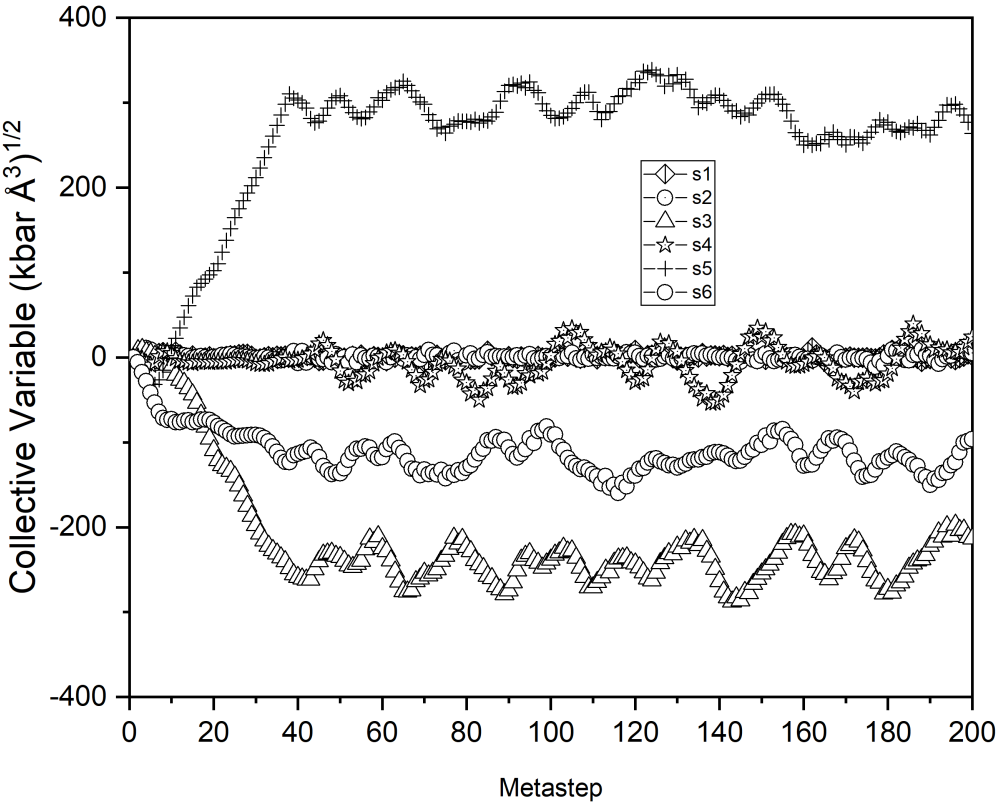

Figure 3.2: Evolution of the Collective Variables showing a phase transition at 35^{th} metastep.

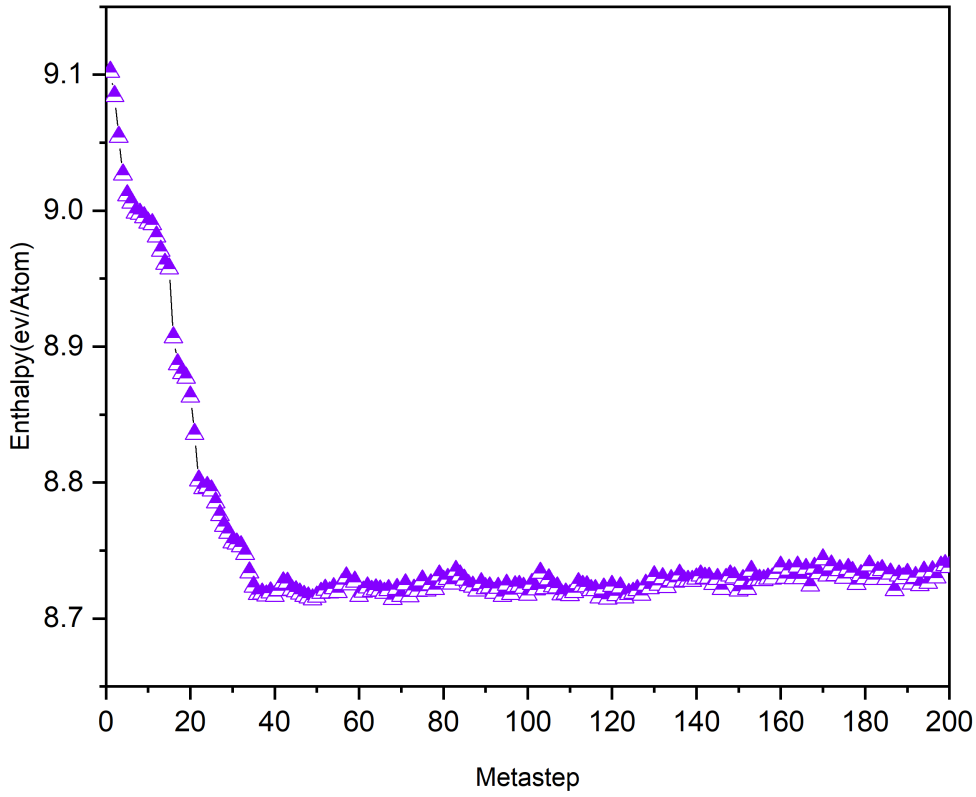

Figure 3.3: Enthalpy per atom evolution in the metadynamics simulation showing a transition at the 35^{th} metastep.

Many structures were found to have competitive enthalpies in this region but with different space groups, such as P$-$1, C2/m, C2/c, P2_1/m, P2/m, P2_1/c, Pbcm, I4/mmm, and P$-$3m1. Of all these structures, only P2_1/m structure fits best to the experimental diffraction pattern of the phase after the Cmcm. Figure 3.4 shows the comparison of the simulated x-ray diffraction of P2_1/m structure with experimentally observed pattern at 63 GPa. It can be seen that all major reflection peaks and features are well reproduced by this structure. At high 2θ angles (greater than 20°), the experimental XRD pattern is degraded because of the reduced diffracted intensity, but the calculation nevertheless reveals several reflections. In view of this reasonably good match, it is easy to suggest the P2_1/m structure as the structure of the post-Cmcm phase.

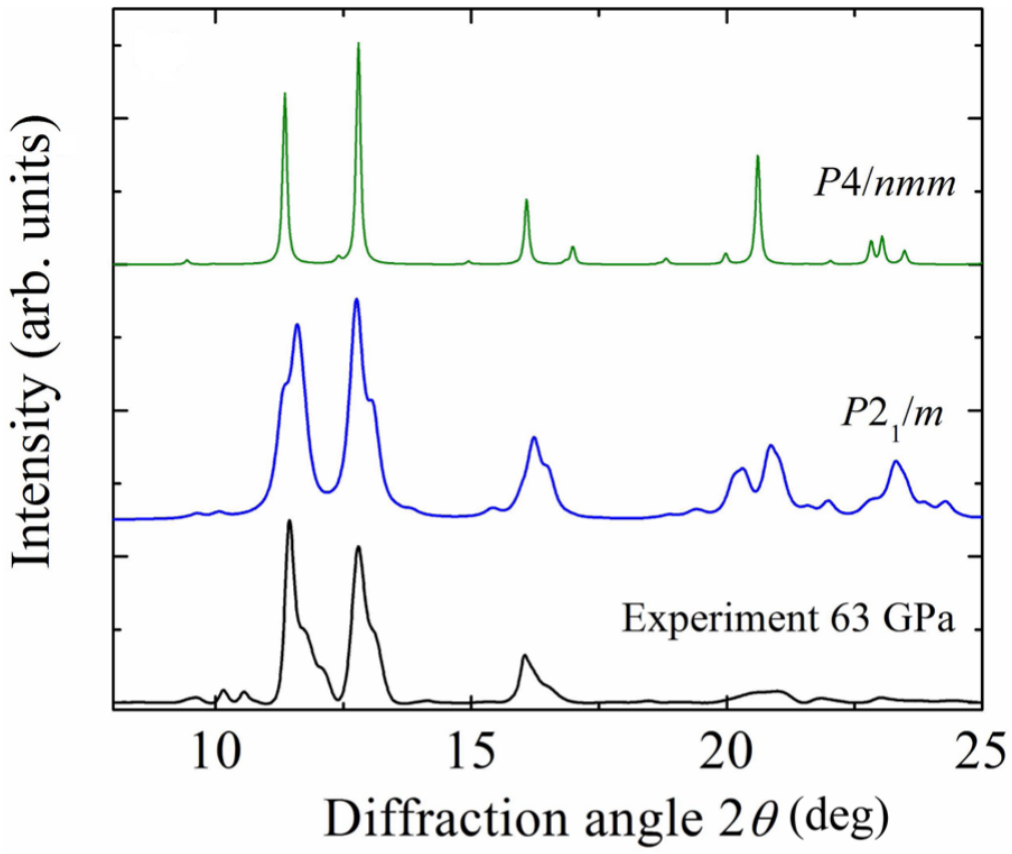

Figure 3.4: Experimental XRD pattern for the post-Cmcm phase at 63 GPa compared with the simulated XRD pattern for the $P2_1/m$ and P4/nmm structures at the same pressure [138].

3.3.2 Transition Mechanism

This $P2_1/m$ structure belongs to a primitive monoclinic unit cell with Z = 4. This assignment is in agreement with the preliminary indexing of the XRD pattern. The optimized lattice parameters of the structure at 63 GPa are: a = 5.8793, b = 4.741, c = 4.900 $\mathring{A}$ and β = 94.19°. The Cd atoms occupy two 2e sites, (0.5051, 0.25, 0.3150) and (0.8025, 0.25, 0.7820) while the Te atoms occupy another two 2e sites, (0.0054, 0.25, 0.2779) and (0.3281, 0.25, 0.8044). The transition from Cmcm to $P2_1/m$ structure involves significant shearing of the (100) plane relative to neighboring plane (see Figure 3.5). The (100) in the Cmcm structure is a pseudo-hexagonal plane on which Cd and Te atoms occupy the sites alternatively in a zig-zag manner. The neighboring (100) plane has identical geometry but the sites are occupied by the other type of atom. As such, the closest Cd-Te distance in the Cmcm

structure occurs between adjacent (100) planes, connecting the Cd and Te that are on top of each other. During the continuous transition to the $P2_1/m$ structure, the (100) planes become puckered and shift relative to the neighboring plans along the [010] direction. After the phase transition, these planes become the (001) planes in the $P2_1/m$ structure.

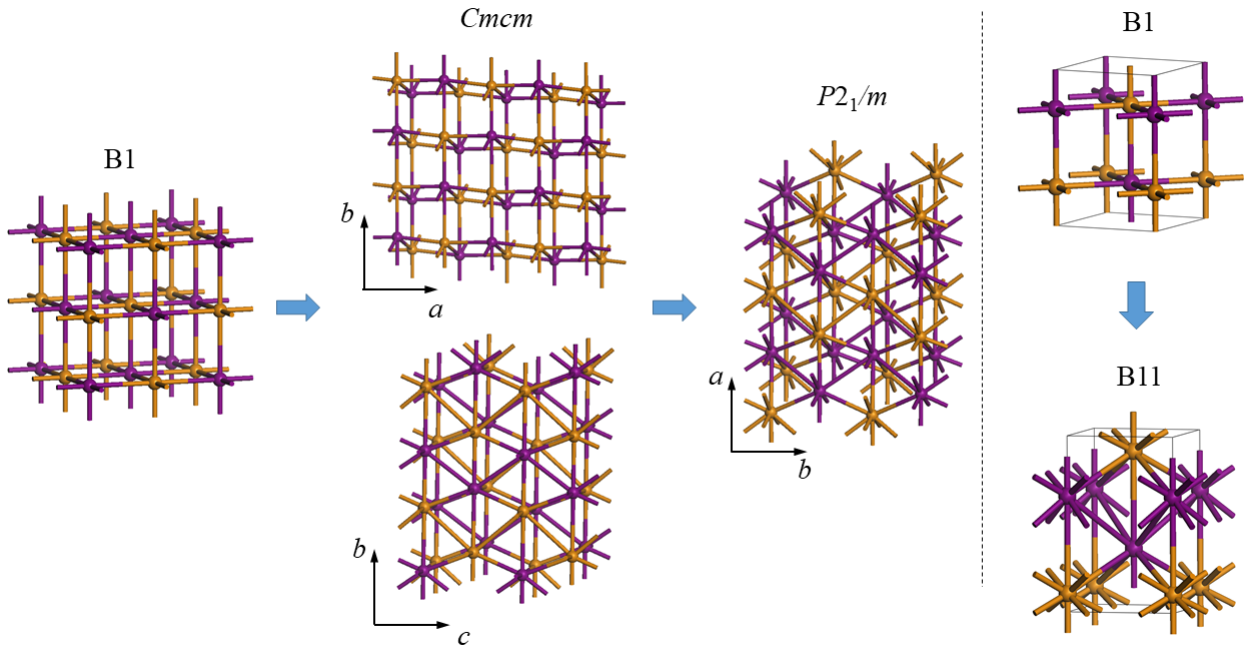

Figure 3.5: Transition pathway for the B1→ Cmcm → $P2_1/m$ phase transition. Shown on the right is the structural relation between B1 and B11 structures. The Cd and Te atoms are colored purple and yellow, respectively [138].

Taking a closer look at this transition path, it can be envisaged that if the simulation is allowed to continue, the transition may continue further and eventually get to a high symmetry P4/nmm (B11) structure. For this reason, it is predicted that the transition from Cmcm does not complete at the $P2_1/m$ structure but changes further to a P4/nmm structure at higher pressure. The B11 structure is the structure of γ-CuTi. Specifically, for the $P2_1/m$ structure to become the B11 structure, the Cd 2e sites need to change to (0.5, 0.25, 0.3423) and (1.0, 0.25, 0.6578), and the Te 2e sites change to (0.0, 0.25, 0.1048) and (0.5, 0.25, 0.8952), while the lattice parameters change to a = 5.01, b = 5.01 and c = 5.71 Å. As can be seen in Figure 3.4, comparing the simulated XRD pattern for the $P2_1/m$ structure with that of the P4/nmm indicate a good amount of resemblance except of the peak broadening which

results from distortion of the unit cell. From this analysis it seems appropriate to suggest that the $P2_1/m$ structure is the intermediate phase between the Cmcm and B11 structures, for it being the common subgroup along the transition path. In a broader pressure range, the phase transition of CdTe is viewed as a B1 to B11 transition bypassing Cmcm and $P2_1/m$ intermediate phases (Figure 3.5).

3.3.3 Equation of States

Pressure dependence of experimentally obtained lattice parameters shows a good agreement with the calculated results particularly in pressure range where CdTe is known to have completely settled in its identified phases (see Figure 3.6). In the region (around 12 - 15 GPa) between the rocksalt and Cmcm CdTe structures, theoretical evaluations give a slighly higher value for b and with slight lower values of c. This region can be seen as the intermediate region in which the system is yet to fully settle into the local minimum that represents the orthorhombic Cmcm phase. Perhaps, the implemented theoretical methods which are designed to visit the local minimum of the condensed matter systems may not fully capture the intermediate region between two phases as can accurately be described by experiments. Be that as it may, the decreases in the calculated values of b is accurately compensated by appropriate values of c to allow the CdTe structure maintains its cell volume as can be seen in Figure 3.7. The drop in volume as the system makes a transition from B1 to Cmcm and a further drop in volume as it changes from Cmcm to $P2_1/m$ further support the phase change of CdTe induced by pressure. To examine the energetics, the enthalpies of the $P2_1/m$ and P4/nmm structures are calculated and compared with that of the Cmcm structure at different pressures (Figure 3.8). This calculation shows that the $P2_1/m$ structure becomes thermodynamically more stable than the Cmcm structure near 45 GPa, which is indeed very close to the experimental transition pressure to the post-Cmcm phase (46 GPa). The P4/nmm structure is calculated to be more stable than the $P2_1/m$ structure near 68 GPa. This finding establishes the $P2_1/m$ structure as the intermediate phase between the Cmcm and P4/nmm structures. Previously, the B2 structure (as in CsCl) was suggested as a candidate structure for the post-Cmcm phase on account of its low Madelung energy, which becomes dominant in determining structures at small volumes [139]. After all, the B1 to B2

transition has been found in many covalent binaries under high pressure. Our calculation shows that the B2 structure of CdTe indeed becomes more stable than the Cmcm structure near 70GPa, but with the $P2_1/m$ and P4/nmm structures now considered, the B2 structure has higher enthalpy than both. In fact, the enthalpy difference between the P4/nmm and B2 structures becomes bigger with increasing the pressure, indicating that the latter has no region of stability at high pressures. This theoretically obtained equation of states shown in Figure 3.8 gives a dependable transition sequence that are consistent to the experiments.

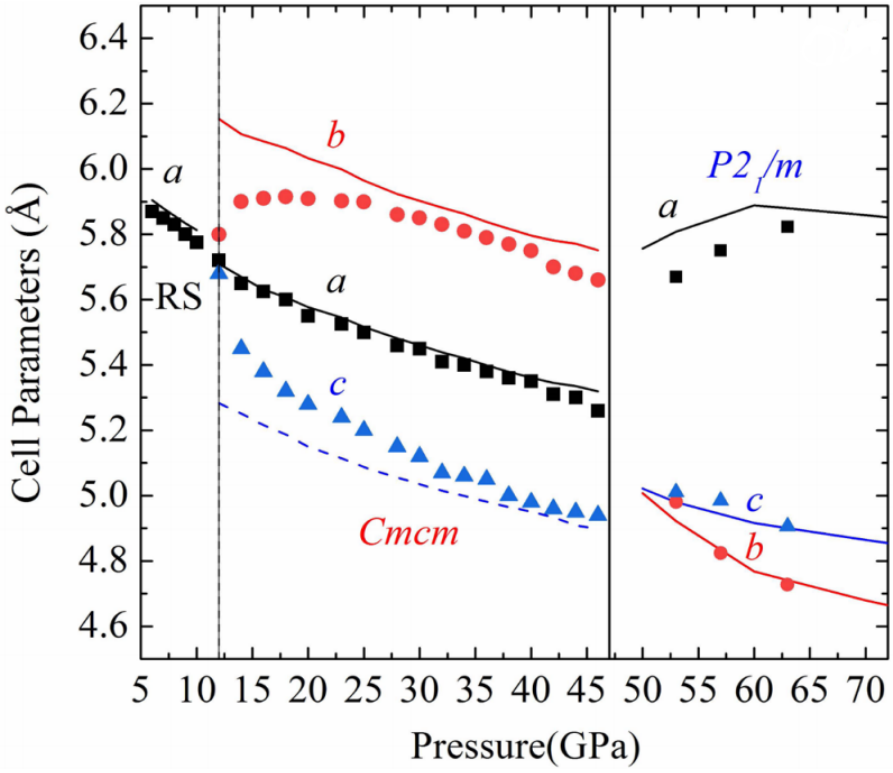

Figure 3.6: Pressure dependence of the lattice parameters of CdTe for the rocksalt, Cmcm, and post-Cmcm phases from experiment (solid symbols) and calculations (lines) [138].

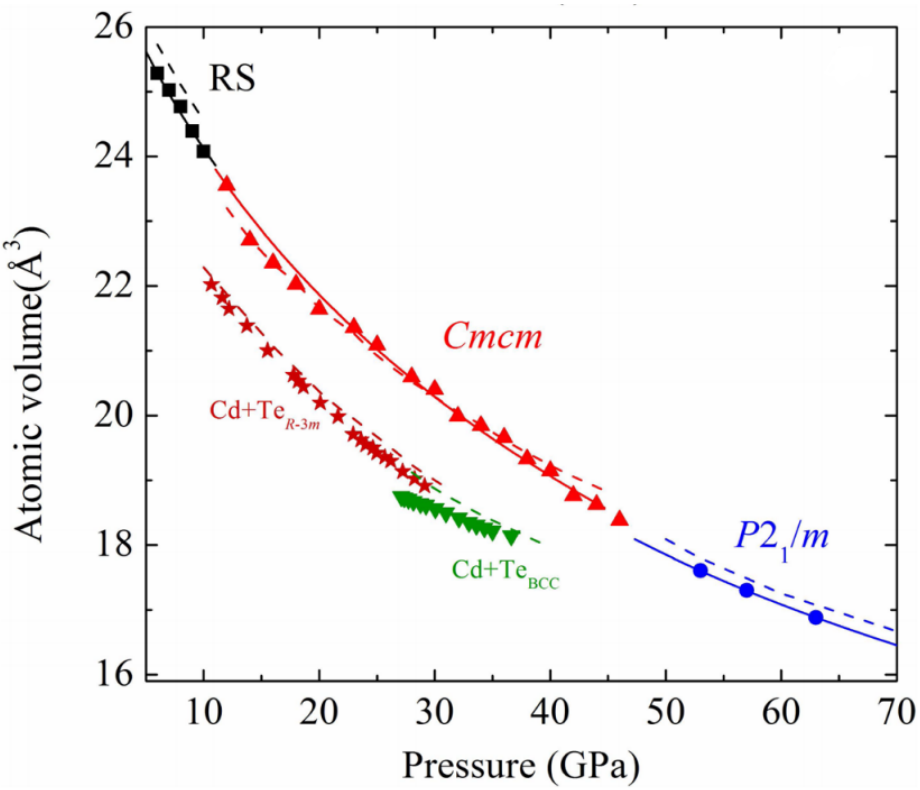

Figure 3.7: Volume-pressure data for the rocksalt, Cmcm, and post-Cmcm CdTe. Experimental and calculated values are shown with solid symbols and dashed lines, respectively. The solid lines are unweighted third-order Birch-Murnaghan EOS fits to the experimental data points. Experimental and the calculated volume of the superposition of (Cd + Te)/2 are also shown for comparison [138].

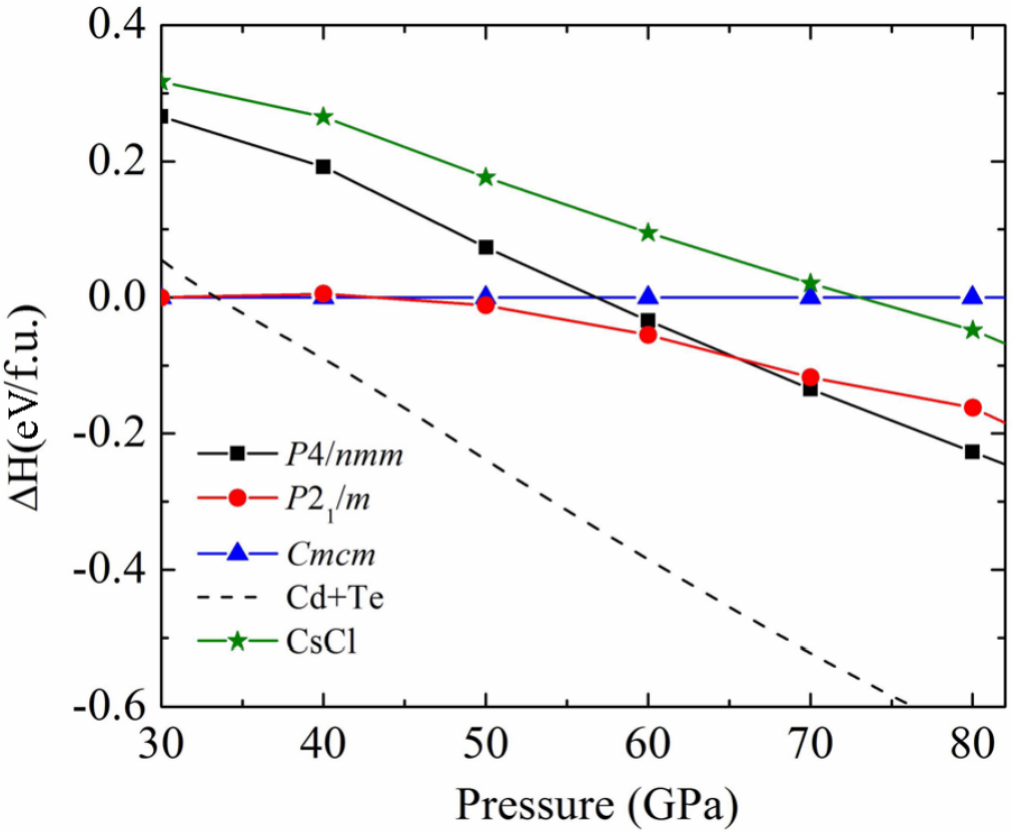

Figure 3.8: Calculated enthalpies for Cmcm, $P2_1/m$, P4/nmm, and B2 (CsCl) structures at different pressures. The enthalpy of the Cmcm structure is used as the zero-energy reference. The enthalpy sum for elemental solids Cd and Te is included for comparison.[138]

3.3.4 Electronic Property and Dynamical Stability

In agreement with previous experimental reports that CdTe becomes metallic in the B1 phase [127, 135], electronic structure results from electronic band structure and density of states calculations show that all the considered structures (B1, Cmcm, $P2_1/m$ and P4/nmm) are metallic (see Figures 3.9 - 3.12)

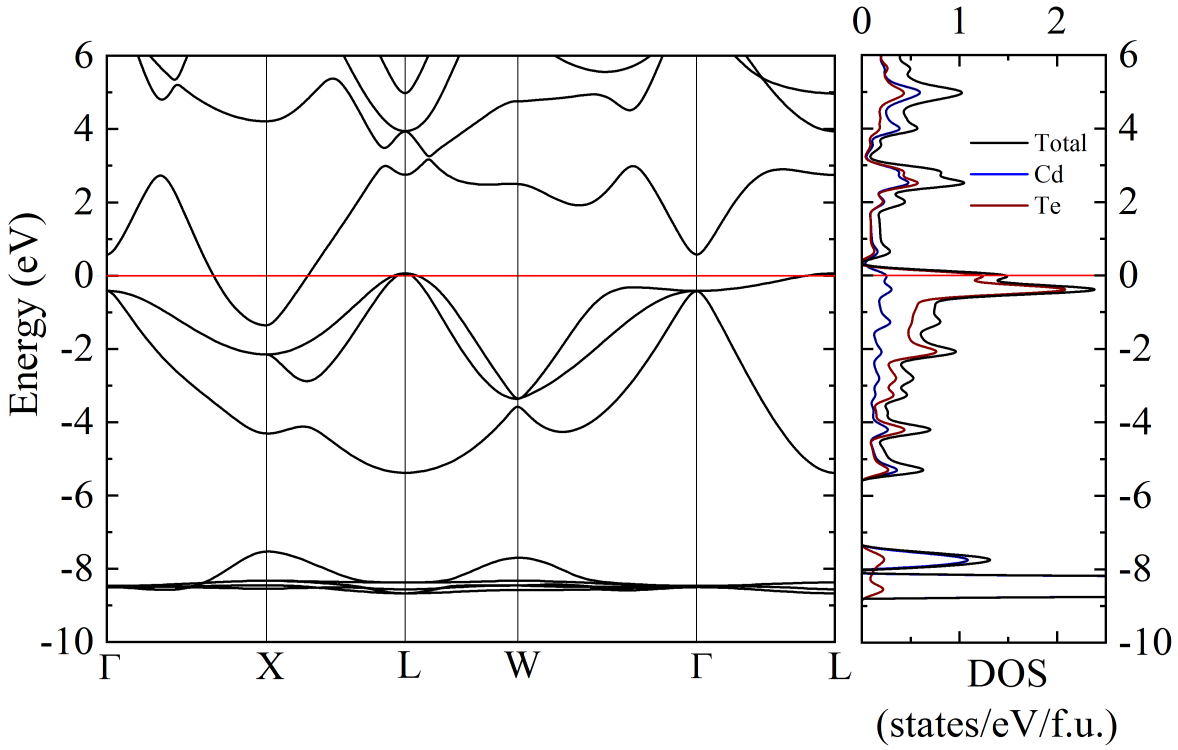

Figure 3.9: Band structure and DOS of the B1 structure at 7.3 GPa. The Fermi level is indicated with the red line [138].

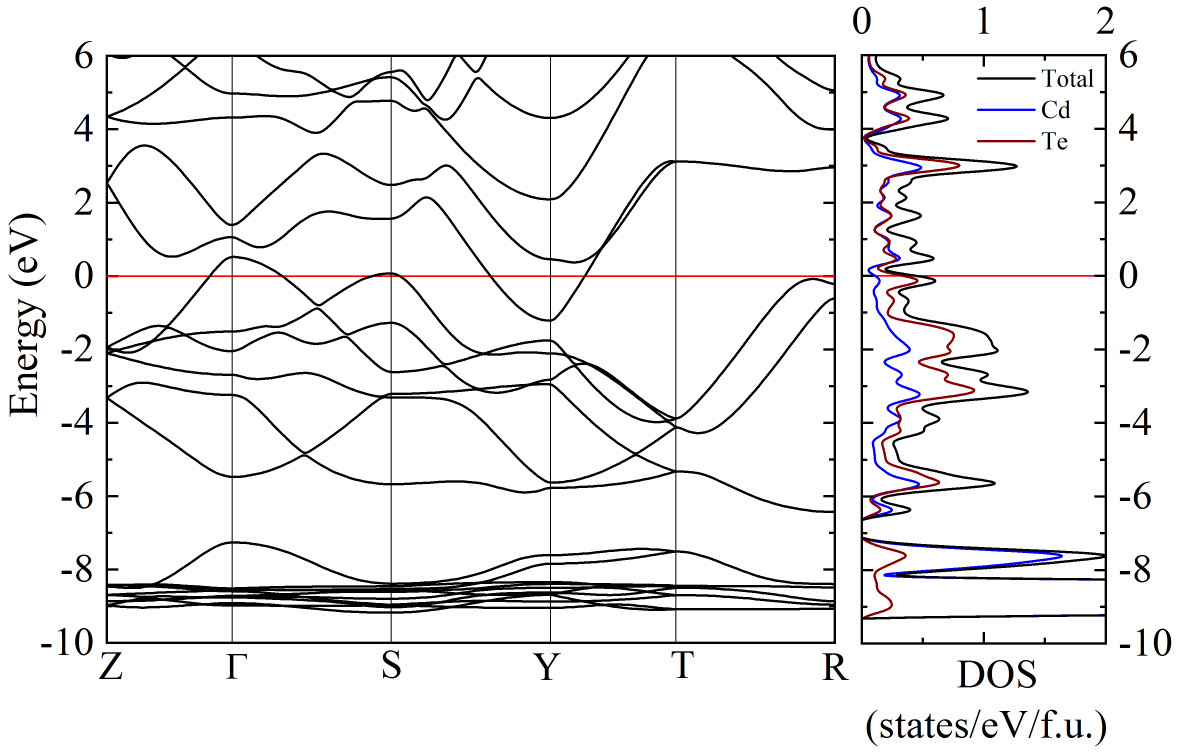

Figure 3.10: Band structure and DOS of the Cmcm structure at 15 GPa. The red line represents the Fermi level [138].

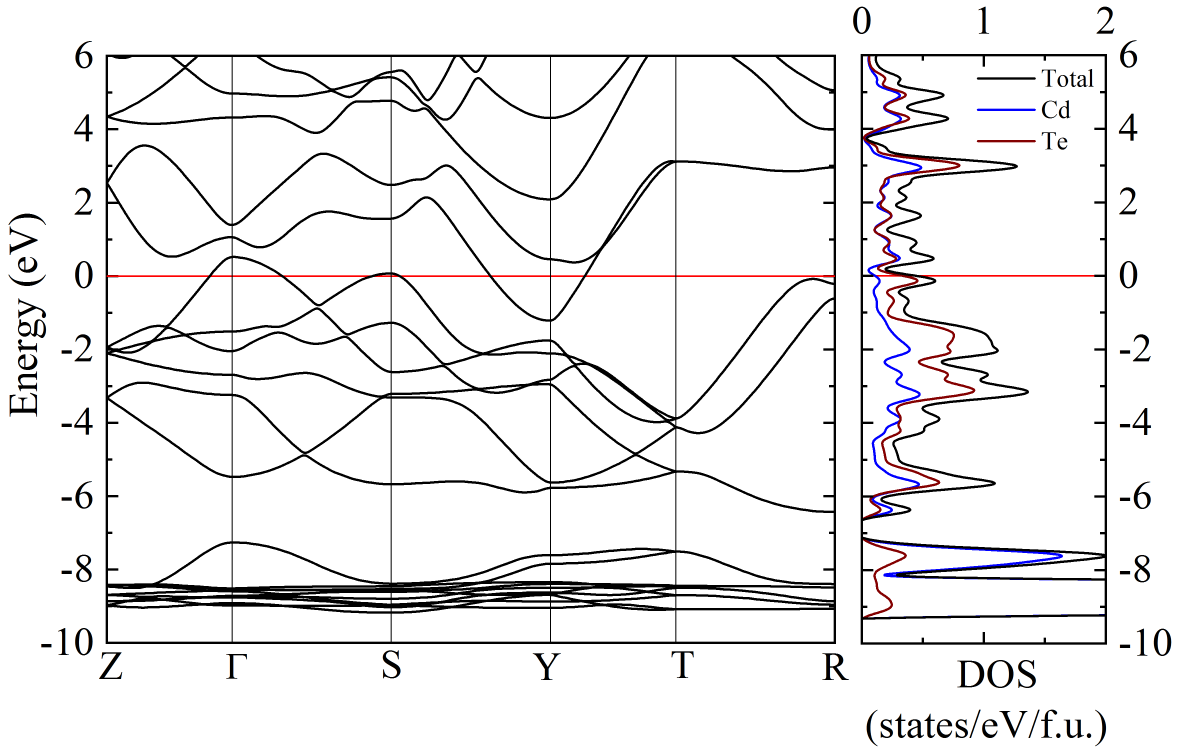

Figure 3.11: Band structure and DOS of the $P2_1/m$ structure at 60 GPa. Fermi level is shown with red line [138].

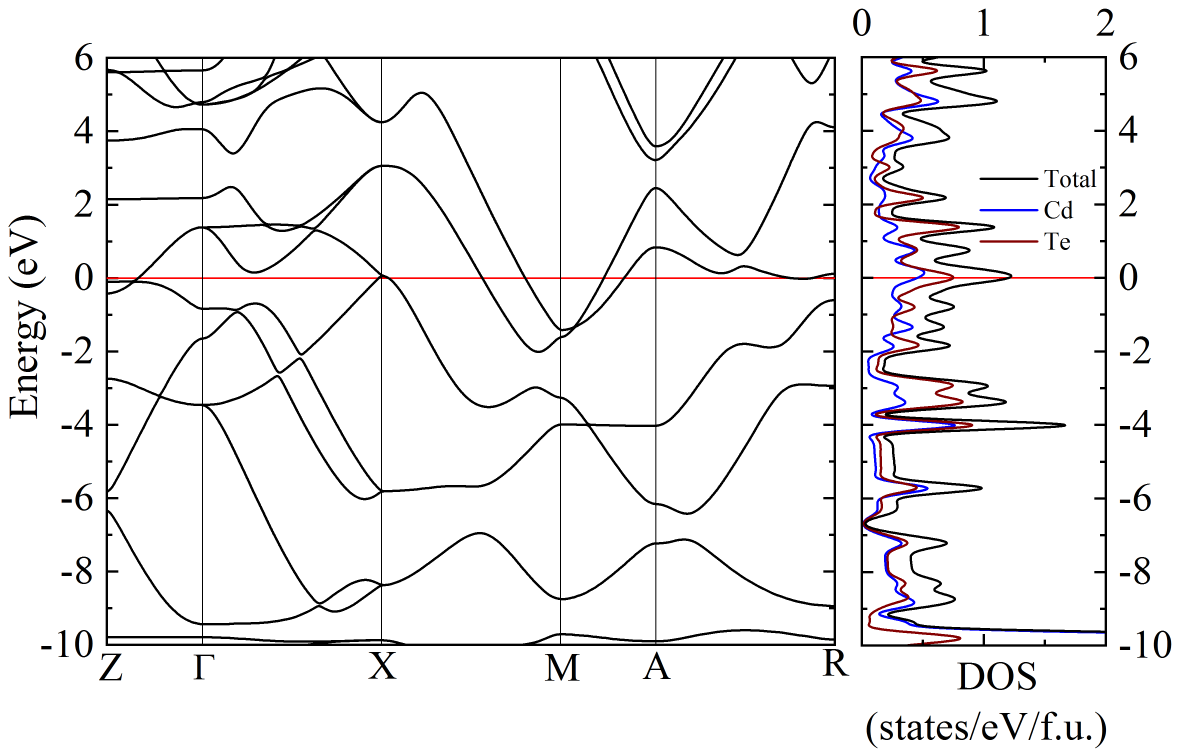

Figure 3.12: Band structure and DOS of the P4/nmm structure at 80 GPa. Fermi level is depicted with red line [138].

In the observed phase transition, the theoretically computed equation of states in Figure 3.8 gives an incontrovertible transition sequence that are consistent to the experiments. Notwithstanding, the fact that the enthalpies of all the CdTe structures are higher than sum of the enthalpies of its constituent elements (Cd+Te) at pressures higher than 34 GPa, is very fascinating. With respect to thermodynamic principles, this occurrence is an indication that CdTe is most likely to decompose in this pressure range. Obviously, it does not decompose to at least 63 GPa which is the maximum pressure attained in the experiment that shows that CdTe is stable at high pressure. A similar situation has been reported in zinc telluride (ZnTe) in that theoretical calculations shows that it should dissociate to elemental components (Zn + Te) at 38 GPa [140] whereas experiment shows that it should be stable to at least about 85 GPa [141]. Although this occurrence may seem troubling, it may not be a coincidence but something particularly related to tellurium compounds. One possible factor that contributes to this anomaly is the non-inclusion of temperature effects since the calculated equation of

states is at zero kelvin so it is likely to underestimate/overestimate the decomposition pressure, but the errors should be minor since the vibrational free energy is only in the order of 10 meV/atom at room temperature. Moreover, since CdTe, Cd and Te are all in solid state at the room temperature, there are no large heat reservoirs, i.e., heat of fusion and vaporization, to reverse the huge enthalpy difference between CdTe and the elements. Thus, we speculate that there exists a large kinetic energy barrier for the decomposition of CdTe, which needs extra pressure to overcome. To this end, the mechanical and dynamical stability of the $P2_1/m$ and P4/nmm structures are examined by the phonon calculations (Figures. 3.13 and 3.14).

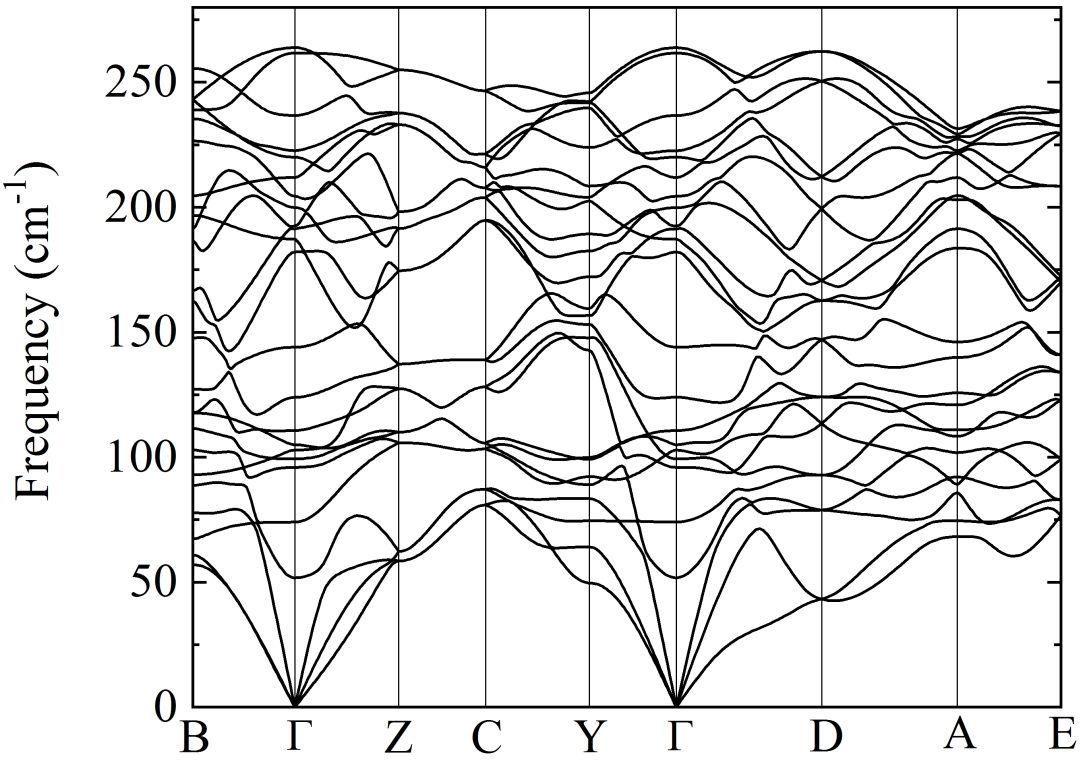

Figure 3.13: Calculated phonon dispersion relations for the $P2_1/m$ structure at 60 GPa [138]

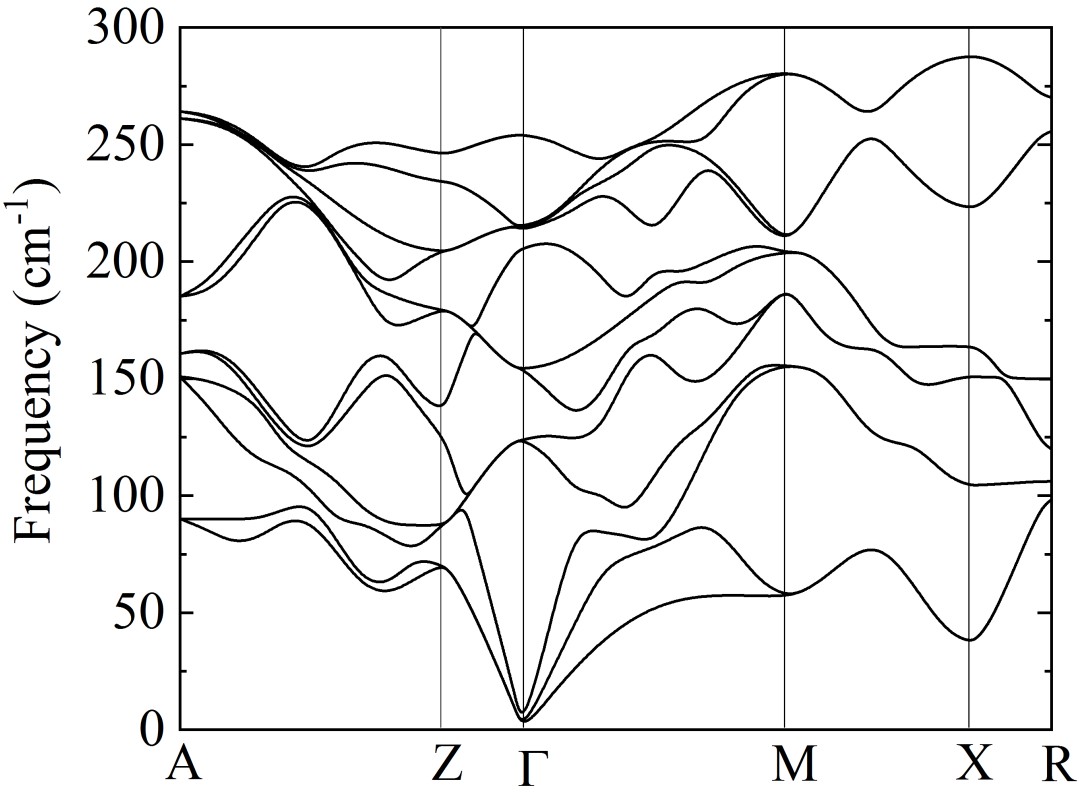

Figure 3.14: Calculated phonon dispersion relations for the P4/nmm structure at 80 GPa.[138]

The appearance of no imaginary frequencies in the phonon dispersion curves for both $P2_1/m$ and P4/nmm confirms that these structures are dynamically stable. Establishing their dynamical stability further ascertain that these two structures neither decompose nor undergo a phase transition in their stable regions. The $P2_1/m$ and P4/nmm phases are predicted as high-enthalpy phases which are commonly seen in solids under high-pressure. For example, the high-pressure synthesis of new compounds from elemental constituents, which is a reversed process to decomposition, always requires much higher pressure than what is predicted for the dissociation pressure. In order to further understand the stability of CdTe at high pressures, a comparison of theoretically calculated atomic volume of CdTe structures and a half of the superposition of (Cd + Te) with experimentally obtained values ([142, 143])

in several pressure points was done (Figure 3.7). The comparison clearly shows that the atomic volume of CdTe is always larger than the superposition of (Cd + Te)/2 both below and above the critical pressure for decomposition (34 GPa) as determined by enthalpy calculations. This observation implies that CdTe has a much lower potential energy (higher stability) than the superposition of (Cd + Te)/2 and provides a plausible explanation for the experimentally observed stability of CdTe at higher pressures. Still, the observed stability of CdTe for more than 30 GPa above the theoretical dissociation point is very significant, and future investigation is encouraged to address this interesting question.

3.4 Conclusion

High-pressure phase transition of CdTe has been investigated by a combined experimental (by Dr. Stavrou) and computational study (by Adebayo under the supervision of Dr. Yao) up to 63 GPa. The previously reported B1 to Cmcm and Cmcm to post-Cmcm phase transitions have been successfully reproduced and identified by synchrotron x-ray diffraction measurements. The long-sought crystal structure for the post-Cmcm phase has been characterized as a monoclinic $P2_1/m$ structure. Analysis of the phase transition pathway suggests that the $P2_1/m$ structure is an intermediate phase between Cmcm phase and the B11 phase. Using enthalpy calculation, the $P2_1/m$ to B11 phase transition is predicted to occur near 68 GPa. In the pressure range of interest, the enthalpy of CdTe is higher than the enthalpy sum of Cd and Te solids, indicate that this compound is a high-enthalpy compound which is stabilized by a tremendously large kinetic barrier.

Chapter 4

STABLE HELIUM-HYDROGEN COMPOUND

This chapter is a slight modification to the paper published in Physical Review B. The reference to the published article is as shown below:

- **Adeniyi, A. O.**, Adeleke, A. A., Li, X., Liu, H., Yao, Y. Prediction of a stable helium-hydrogen compound:first-principles simulations. Physical Review B, 104(2), 024101.(2021).

4.1 Introduction

Helium belongs to group VIIIA in the period table. Members of this group are generally considered to be chemically nonreactive because of their complete outermost shell. In recent years however, various research groups have investigated the structures and properties of compounds formed by elements in the inert group. At high pressures, stable compounds of inert elements include van der Waals compounds in the form of Laves phase such as $Ar(He)_2$, $Ne(He)_2$ [144], $Ar(H_2)_2$ [145], and $Xe(O_2)_2$ [146]. The stability of these structures has been directly linked to the efficient packing and configurational entropy which are greatly enhanced by pressure. Structures of chemically bounded metastable He compounds have been predicted [147]. Furthermore, reaction between Xe and Fe/Ni which help to provide insight into the missing Xe paradox in the earth core has also been explored [148]. More recently, He being the element with highest value of ionization potential and very low value of electron affinity [147] has received extensive experimental and theoretical exploration regarding its tendency to undergo a chemical reaction or form stable neutral compounds in which closed shell electrons of helium could take part in chemical bonding. The results of such investigations have shown that it reacts with metal, metal oxide, metal fluoride and sulphides

[95, 149, 150], in which its presence makes a significant impact on the long range Columbic interactions. It also reacts with ammonia [151], nitrogen [152], water [125] and other inert elements [144], where its presence plays important role in the internal pressure of the system with notable charge transfer. Despite the fascinating predictions at high pressures, little is known about the likelihood of helium to undergo a chemical reaction with other elements and form stable compounds that include notable helium bonds at ambient conditions.

Helium and hydrogen are the two most abundant elements in the universe and they contribute the highest percentage to the composition of stars and all the planetary bodies. For instance they contribute about 70-95% to the mass of Saturn and Jupiter in which several models predict an inner ionized helium and hydrogen envelope as well as an outer neutral He and molecular H_2 envelope [153, 154]. They are also the major components of recently discovered exoplanets [155]. To get a good model of these exoplanets, it is important to understand the equation of states (EOS) of all the various components. In principle, the mechanical structure and internal heat profile of any planet can be determined completely from the EOS of its chemical constituents. Any form of inaccuracy in the EOS can lead to false estimation of what these planets contain as well as their formation process and how they may evolve. One long unanswered question is why Saturn has about 50% luminosity more than predicted by existing models [154]. Both Saturn and Jupiter give out about twice the energy they get from the sun. The method of heat transfer is the same in them and they are both well mixed in their interior. A cooling model for homogenous planets to estimate the luminosity of Jupiter produces a result that closely matches the measured value whereas the luminosity of Saturn is about 50% more than the model produces [156]. This indicates that Saturn has other sources of energy that may or may not be present in Jupiter. One possible contribution to this additional energy source in Saturn as proposed by Smoluchowki [157] is H-He demixing [158], during which heavier He droplets fall down from H_2-He layer and exchange gravitational energy for thermal energy through viscous precipitation. The miscibility of H_2 in He matrix or vice versa at high pressure plays an important role in deciding the phase diagrams of the H_2-He mixture. Could a chemical reaction between helium and hydrogen leading to the formation of a stable He-H_2 compound also contribute to

this additional energy? To answer these fundamental questions and/or propose new models towards the composition, formation and evolution of these planetary bodies, the EOS for H_2-He system and any stable structure of H_2-He has to be accurately estimated [159].

Hydrogen and hydrogen-rich compounds have fascinating physical and chemical properties especially at extreme conditions. Among other interesting properties, hydrogen has been predicted to show characteristic of a metallic and superconducting superfluid and high temperature superconductivity [160, 161, 162]. Several compounds of hydrogen with other elements have been of interest in condensed matter physics because of the potential application as high temperature superconductors. These include FeH_5 [163], YH_6 [164], CaH_6[165], H_2S , H_3S [166], YH_{10} and LaH_{10} [50]. To the best of our knowledge, no actual stable compound of helium hydrogen-rich system in which there exists a favorable interaction between helium and hydrogen either from experiment or theoretical predictions, has been reported. Pioneer works including first principles calculations on this system have so far been able to provide insight to understanding the thermodynamics of helium hydrogen mixing [167, 168] and demixing [169, 170]. Theoretical studies have predicted the phase separation of H_2 and He at high pressures and temperatures [169], as well as the miscibility of H_2-He mixtures under planetary conditions [171]. The reactivity of He has also been demonstrated in helium hydrates, in which the He filled ice-II and ice-I_h were found to be energetically favorable against all decomposition reactions at 1 kbar [172]. In a recent experiment, spectral evidence has shown that there can be sufficient mixing in He-rich mixture for forming strong chemical association of H_2 to He at pressures below 100 GPa [173, 168]. However, it was later argued that the Raman signal observed in the previous experiment was due to N_2 impurities and subsequent formation of a N_2-H_2 van der Waals (vdW) solids at high pressure [174]. The question as to whether there is an interaction between helium and hydrogen that can lead to the formation of stable He-H_2 compounds at right conditions still remains unclear. Thus, unravelling possible stable compounds of this system and understanding the type of chemical bonding in such compounds will not only be potentially useful in advanced technology applications such as hydrogen storage but also be an essential tool in accurate modelling of the formation, composition and evolution of important planetary bodies. Hence, in this

work the possibility of hydrogen forming a stable compound with helium has been explored. This study is performed on helium hydrogen-rich [HeH_{2x}] (x = 1, 2,3,4,5,6) systems using ab initio random structure search and first principles calculations, and it has revealed a thermodynamically stable helium-hydrogen compound between 0 and 8 GPa with stoichiometry $He(H_2)_3$ that belongs to the triclinic P-1 space group. Topological analysis shows that this structure exhibits interaction between the H and He atoms that is similar to vdW interaction found in He-O interactions for the helium filled ice II [175]. The $He(H_2)_3$ structure is also found to be mechanically stable from the phonon calculations. The present results indicate the existence of mixing helium-hydrogen system with energetically favorable H_2-He interaction that may be sufficient for crystal solidification at low temperature and high pressure, enabling an understandable effect on the evolution of the interiors of gas giants.

4.2 Computational Method

The search was performed with the random structure search method [88] at ambient conditions with primitive cells that contain 1 helium atom and 2 to 12 hydrogen atoms. Notable successful applications of this method include the prediction of the ground-state and metastable structures of novel materials such as ice at high pressures [86], atomic metallic hydrogen [87], and several other systems [90]. Structural optimization, equation of states, electron localization function (ELF), density of states (DOS) and electronic band structure of candidate structures was done using the Vienna ab initio Simulation Package (VASP) [21] with the Projected Augmented Potentials (PAW) [20, 123]. The H potential has the $1S^1$ valence state and He has the $1S^2$ valence state in addition to the Perdew-Burke-Ernzerhof (PBE) exchange correlation functional [124]. To check the effect of van der Waal interaction on the formation of the compound, several van der Waal functionals were applied including optP86-vdW functional [25], optPBE-vdW [25], optP88-vdW [25] and vdW-D2 [176] functionals, and semi-empirical DFT-D3 method [177]. Phonon dispersion relation of the structures was done with density functional perturbation theory as implemented in VASP after which the results were post processed with the PHONOPY code [61]. The plane wave basis set was expanded with a kinetic energy cutoff of 480 eV and a dense k-point grid with

spacing of $0.5\mathring{A}^{-1}$. Topological analysis of the charge density was estimated with the quantum theory of atoms in molecules (AIM) [28] as implemented in CRITIC2 [59]. This method has been used to successfully characterize closed shell interactions such as ionic, dihydrogen, and hydrogen bonds [178].

4.3 Results and Discussion

4.3.1 Phase Stability and Stable Crystalline Structure

A crystal structure is deemed to be thermodynamically stable if it has a negative formation enthalpy (Δ H^f) compared to the mixture of its constituent elements or other likely structures. Hydrogen has been known to have complicated phase transition in the pressure ranging from 0 GPa to 500 GPa. In the pressure range < 105 GPa, it has been predicted to be most stable in the hexagonal $P6_3/m$ phase before changing to C2/c in the pressure between 105 – 270 GPa, and then changing to Cmca-12 from 270 GPa to 385 GPa and finally to Cmca-4 in the pressure range 385-480 GPa [179]. Helium on the other hand generally maintains a hexagonal closed pack (HCP) structure over a wide pressure range. The search for the structure of He-H_2 systems was performed at 0 GPa and a new compound, $He(H_2)_3$, that has a negative enthalpy of formation relative to the HCP He and the hexagonal $P6_3/m$ of hydrogen [179] has been found [180]. The convex hull of the He-H_2 system (Figure 4.1) constructed at 0 GPa indicates that all the stoichiometries in consideration have compound with negative enthalpy of formation with respect to elemental $P6_3/m$ H and HCP He. However, the convex hull at 0 GPa does not conclusively suggest the formation of any He-H_2 compound since the enthalpy is not a sufficient measure of thermodynamic stability at ambient pressure. The formation of He-H_2 compounds is therefore expected to occur at high pressures, where all phases become solid and the enthalpy becomes a meaningful factor of thermodynamic stability [180].

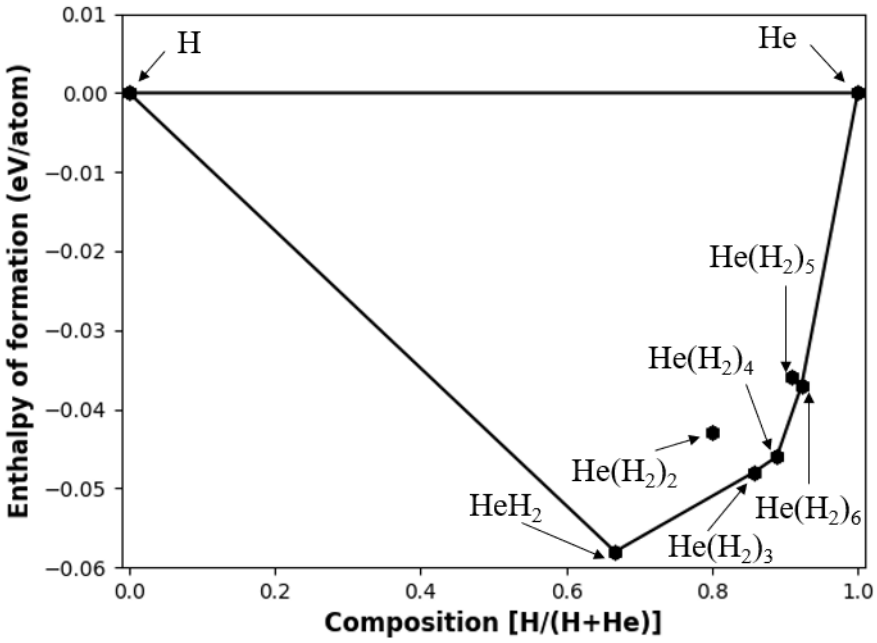

Figure 4.1: Enthalpy of formation for all the considered He-H_2 compounds with respect to elemental decomposition at 0 GPa and 0 K [180].

Nevertheless, only HeH_2, $He(H_2)_2$, $He(H_2)_3$ and $He(H_2)_6$ are on the hull from which $He(H_2)_3$ is the only dynamically stable candidate (see phonon dispersion curves later). For this reason, this work and following discussion is focused on the $He(H_2)_3$ compound. To check the threshold for the formation of this structure, the equation of state was estimated up to 20 GPa. The appropriate stable crystal structures for elemental composition in the pressure range of interest as highlighted earlier were used for the calculation. This predicted compound belongs to the triclinic P-1 space group and its formation is continually favoured at high pressure as established by the variation of ΔH^f with pressure shown in Figure 4.2. Because of the light masses of hydrogen and helium, zero-point motion may have a large effect on the stability of the He-H system. Furthermore, at low temperatures, the fluctuation of electron distribution likely induces vdW interaction which is particularly notable for helium and hydrogen [181]. Thus, ΔH^f was corrected by adding zero-point energy (ZPE) contributions estimated using harmonic approximation, and vdW contribution obtained by using optP86-vdW functional [25] (Figure 4.2). The calculation has been repeated using optPBE-vdW [25], optP88-vdW

[25] and vdW-D2 [176] functionals, and semi-empirical DFT-D3 method [177] (see Figure 4.3). The result of the inclusion of ZPE increases the pressure for decomposition of $He(H_2)_3$ (to He and H_2 solids) from 8.8 GPa to 9.6 GPa as seen in Figure 4.1 while the application of optP86-vdW functional slightly lowers the decomposition pressure to about 8.5 GPa. The inclusion of zero-point motion and vdW interaction supports the stability of the $He(H_2)_3$ solid under moderate pressures.

The structural parameters of the P-1 structure optimized at 0 GPa [shown in Figure 4.4 (a)] are a=3.8972 Å, b=4.1910 Å, c=4.2709 Å , $\alpha = 89.1897^o, \beta = 89.165^o$, $\gamma = 89.6054^o$ with H(1) at 2i: 0.43278 0.46895 0.44687, H(2) 2i: 0.45252 0.06081 0.95193 , H(3) 2i: 0.06251 0.55858 0.96521 and He 1b: 0.0 0.0 0.5. As shown in Figure 4.4 (c), in the P-1 structure, each He atom is surrounded by six hydrogen atoms, two from the H(1) and its symmetry equivalent, two from H(2) and its symmetry equivalent and then two from H(3) and its symmetry equivalent. There exists different He-H distances and they are measured to be 2.604 Å , 2.650 Å and 2.708 Å for He-H(1), He-H(2) and He-H(3) respectively. At a higher pressure of 8 GPa, these distances are reduced to 2.191 Å, 2.198 Å and 2.212 Å. Clearly, the distances are within the sum of the vdW radii of helium (1.4 Å) and hydrogen (1.2 Å), suggesting that the presence of helium is paramount to the formation and stability of the compound.

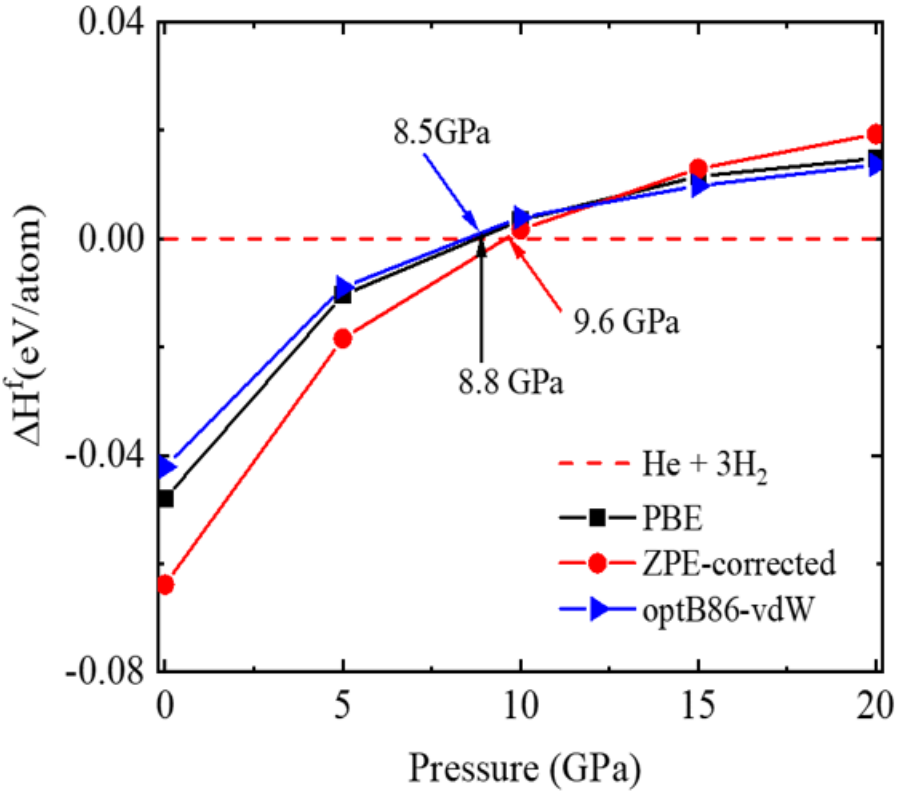

Figure 4.2: Calculated enthalpy of formation for $He(H_2)_3$ with respect to He and $3H_2$. Black: PBE calculation without any energy correction, Red: with inclusion of zero-point energy, Blue: with inclusion of vdW interaction obtained from optB86-vdW functional [180].

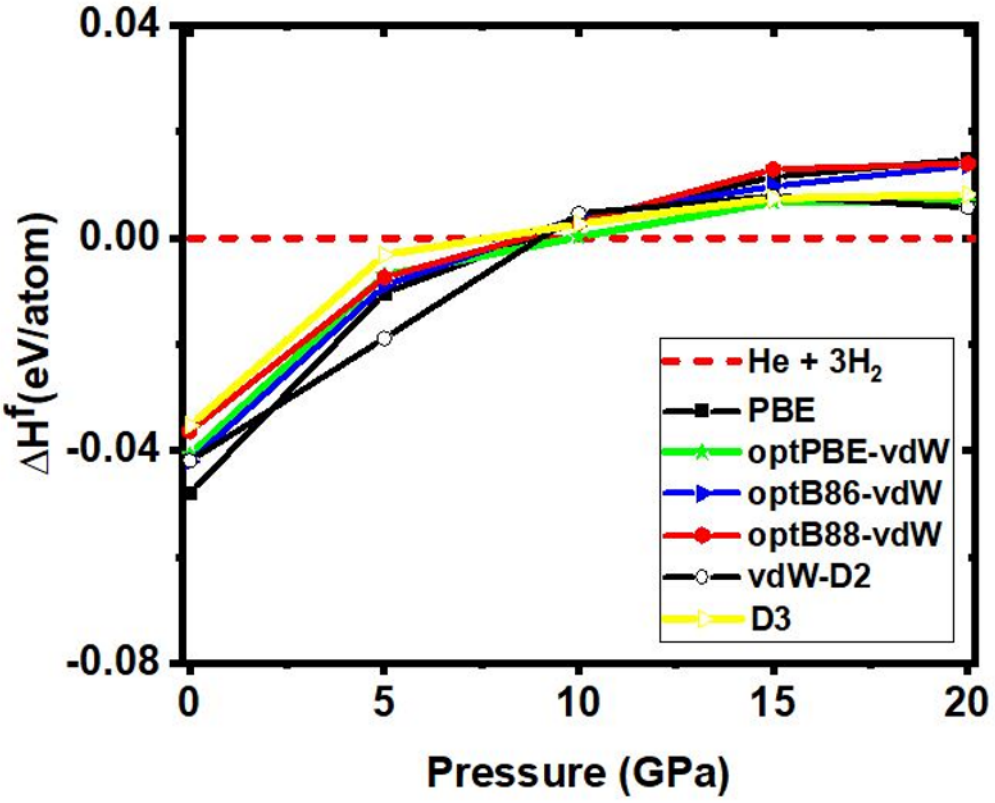

Figure 4.3: Formation enthalpy of the P-1 structure with respect to the hcp He and $P6_3/m$ hydrogen computed with PBE potential and then with optPBE-vdW, optB86-vdW, optB88-vdW, D3 and vdW-D2 functionals [180].

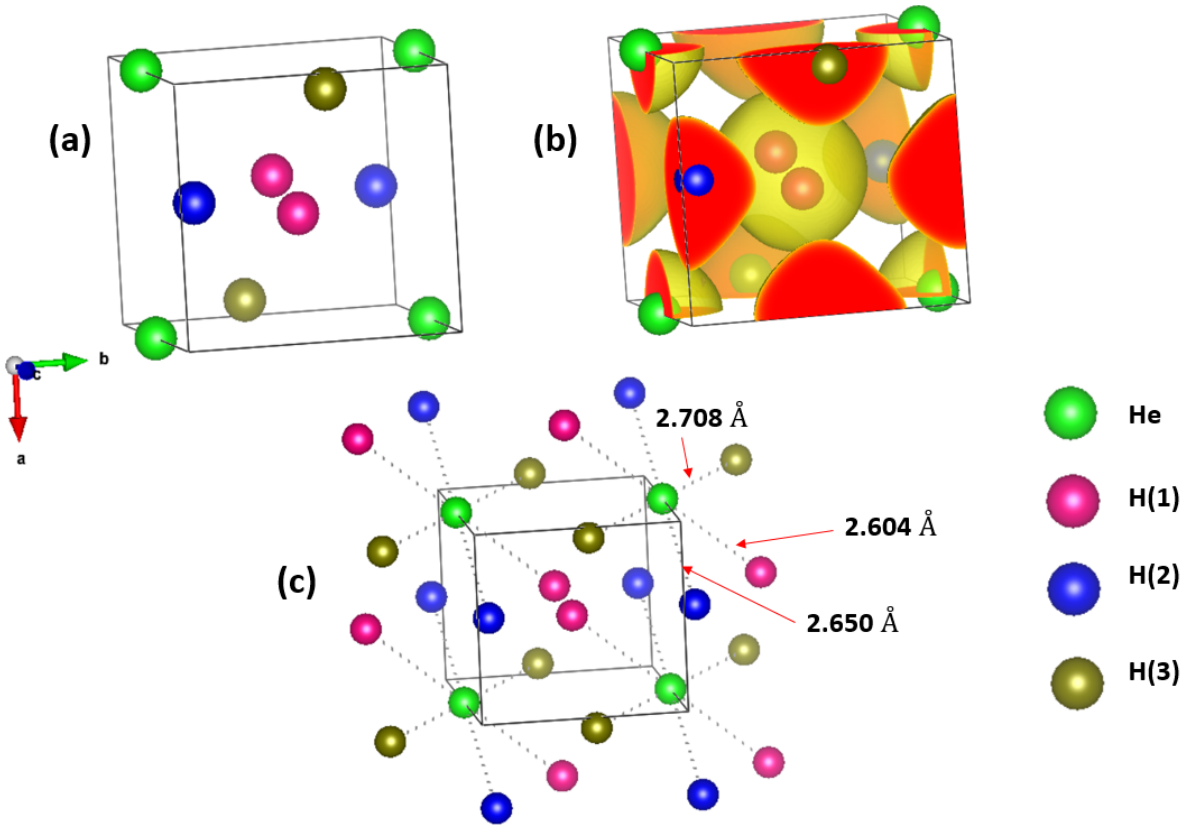

Figure 4.4: (a) P-1 crystal structure (b) the same structure with the electron localization function at $He(H_2)_3$ at 0 GPa (isovalue = 0.8) (c) Extended P-1 crystal structure showing the coordination of He atom [180].

This arrangement suggests that the presence of helium is very paramount to the formation and stability of the structure. Unsurprisingly, after the removal of helium at 0 GPa, the structure becomes very unstable as evident from the negative frequencies in the phonon dispersion curve (see Figure 4.6).

4.3.2 Dynamical stability and Electronic Structure of the P-1 Compound

The force calculation was done using a 3×3×3 supercell containing 189 atoms built from fully optimized unit cell and results was then post processed with the PHONOPY code [61] to obtain the phonon dispersion curve. The results of phonon dispersion calculation of the P-1

structure at 0 GPa (Figure 4.5 (a)) and at 8 GPa (Figure 4.5 (b)) show that it is dynamically stable and experimentally accessible at 0 GPa as well as at a high pressure of 8 GPa since the absence of imaginary frequencies is often an indication of the accessibility of a crystal structure experimentally, as well as its dynamical stability.

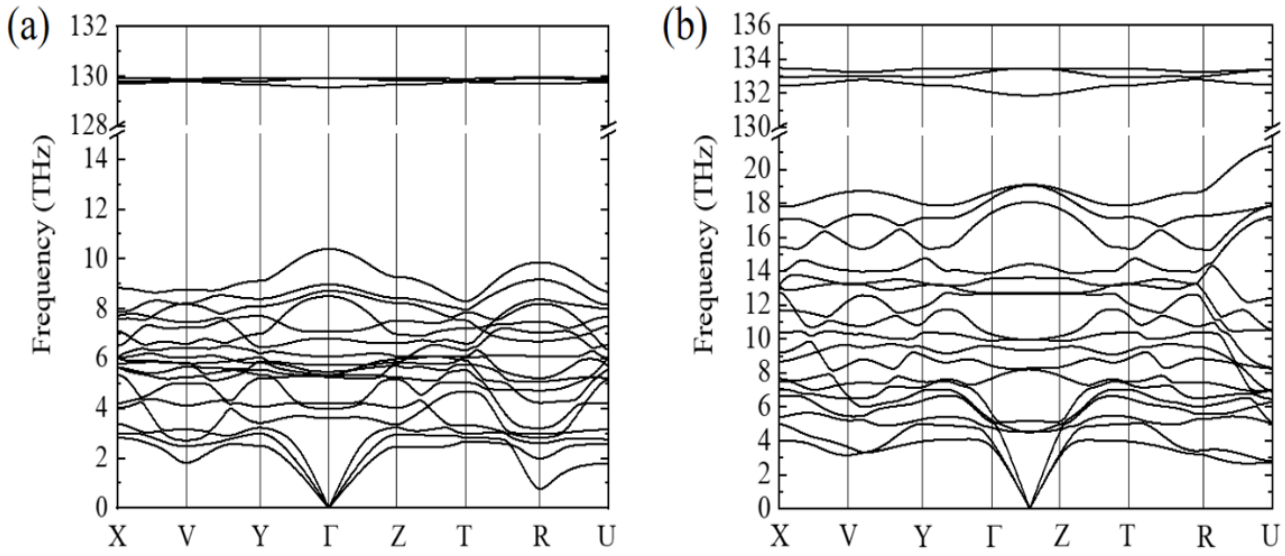

Figure 4.5: (a) Phonon dispersion curve for the P-1 structure at 0 GPa and 0 K (b) Phonon dispersion curve for the P-1 structure at 8 GPa and 0 K [180].

At ambient pressure, the highest frequency phonons in the compound has a value of 130.451 THz (4351.38 cm^{-1}) while the removal of helium leads to an increase in highest vibration frequency to 131.058 THz (4371.63 cm^{-1}). These values are consistent, within DFT approximations, with the measured value of 4342 cm^{-1} (130.17 THz) associated with H-H stretching mode at ambient condition [182]. In order to put this in perspective, at ambient pressure, calculated highest frequency phonon in the hexagonal $P6_3/m$ structure of hydrogen has a value of 4575.76 cm^{-1} (137.18 THz). Thus, there exists a notable decrease in the highest phonon frequency as a result of the presence of helium. This suggests a certain degree of He-H attractive interaction in the P-1 structure. The calculated phonon dispersion curves for all other phases on the convex hull shown in Figures 4.7 - 4.9 indicate that they are dynamically unstable.

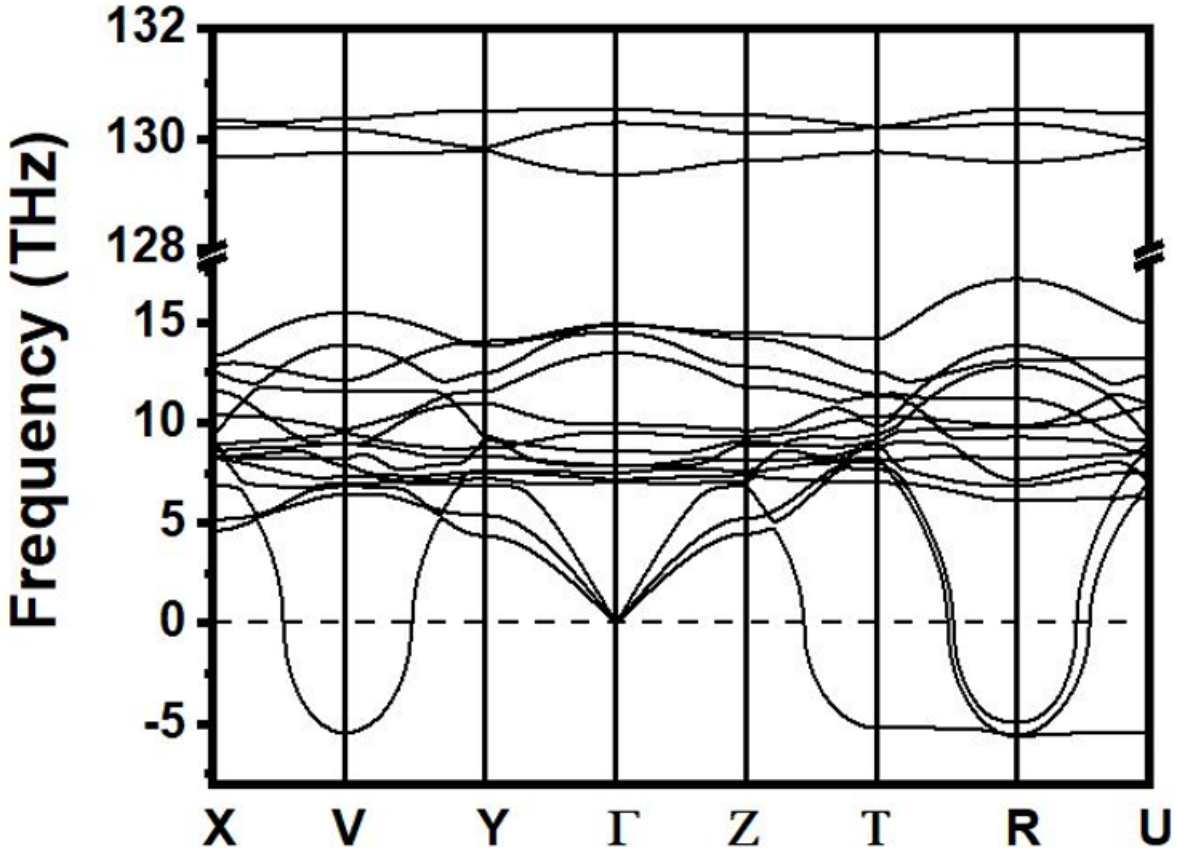

Figure 4.6: Phonon dispersion curve of the P-1 structure at 0 GPa when He atom was removed [180].

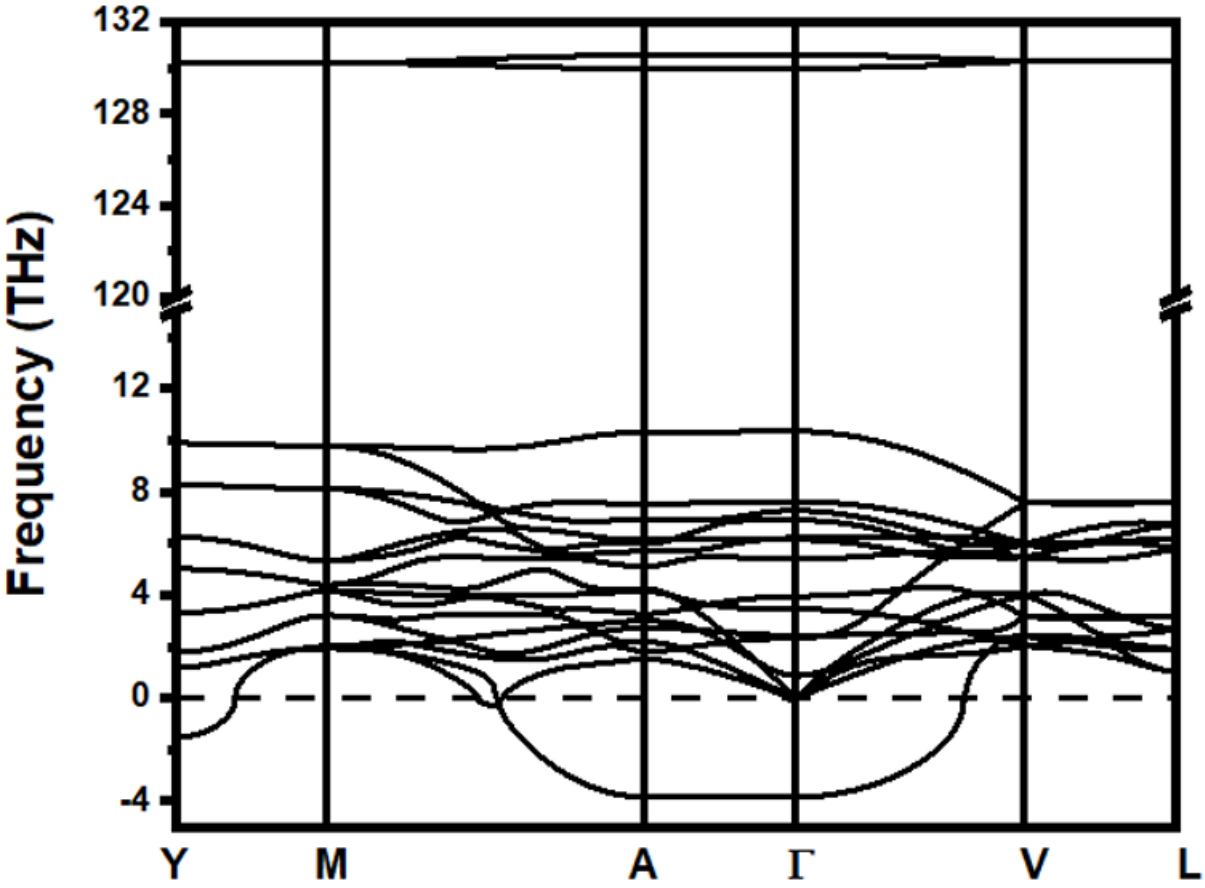

Figure 4.7: Calculated phonon dispersion curves for the HeH_2 compound with monoclinic C2/m symmetry at 0 GPa and 0 K [180].

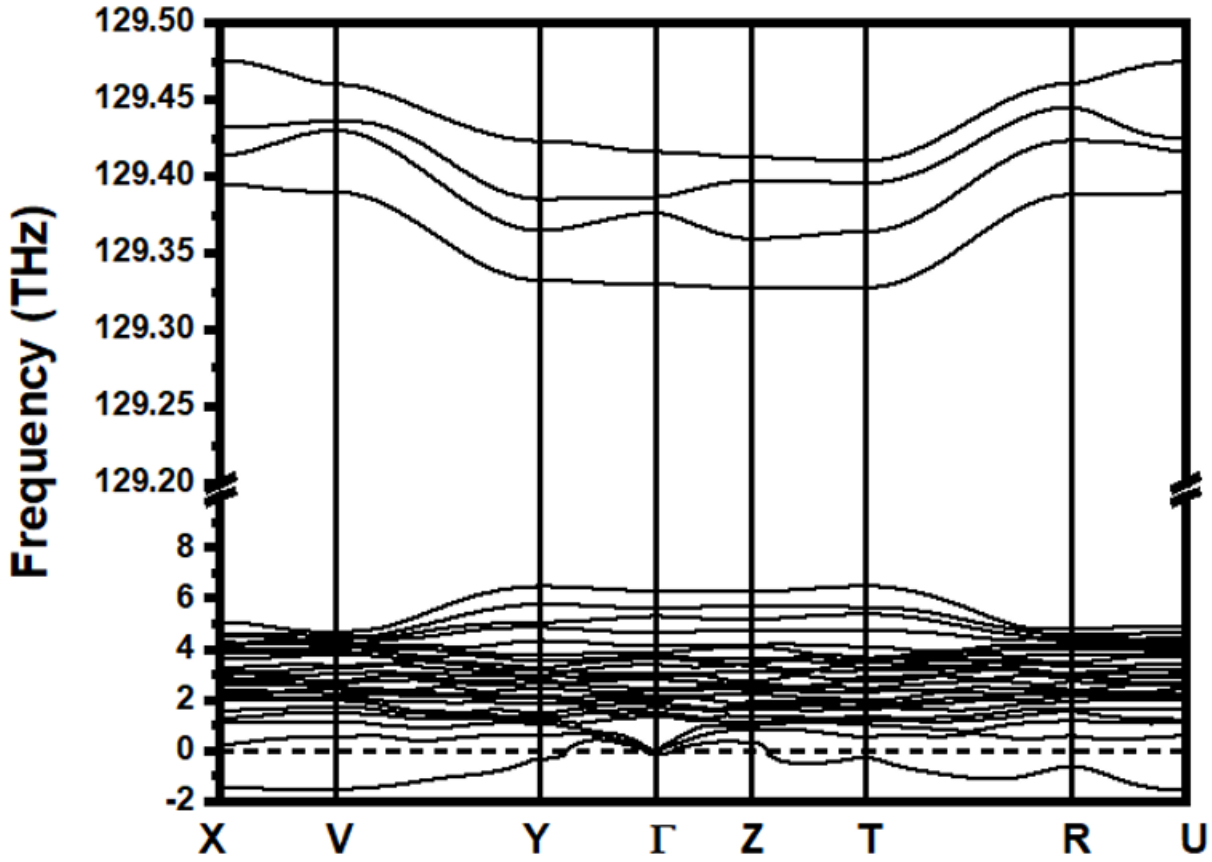

Figure 4.8: Calculated phonon dispersion curves for the $He(H_2)_4$ compound with triclinic P1 symmetry at 0 GPa and 0 K [180].

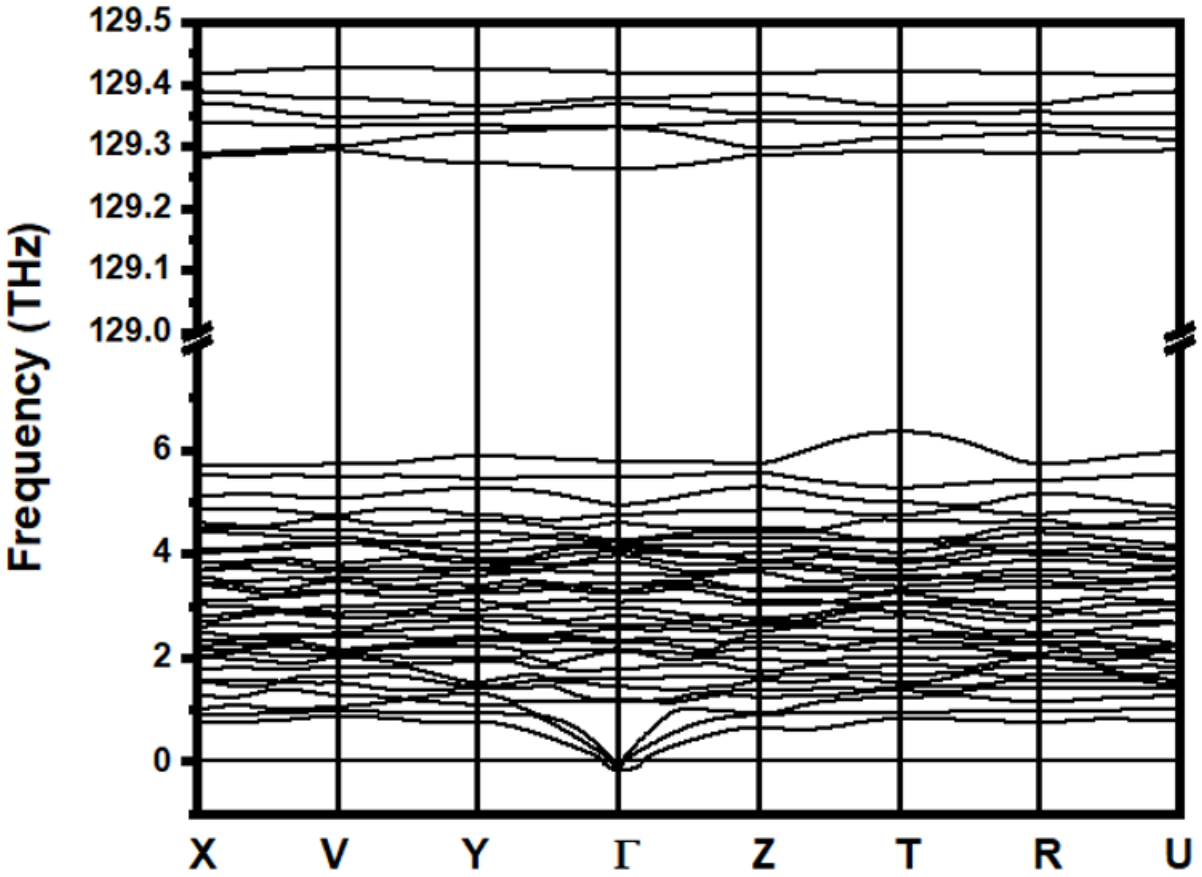

Figure 4.9: Calculated phonon dispersion curves for the $He(H_2)_6$ compound with triclinic P1 symmetry at 0 GPa and 0 K [180].

The calculated electronic band structure and projected density of states at ambient pressure and at 8 GPa [Figures 4.10 (a) - 4.10 (d)] reveal that the P-1 structure is a wide gap insulator. At 0 GPa it possesses an indirect band gap of 8.49 eV which reduces to 7.04 eV at 8 GPa between Γ and R high symmetry points. The density of states at 0 GPa shows that valence band maximum and conduction band minimum in the P-1 structure has significant contribution from both helium and hydrogen. The electronic DOS at ambient pressure shows that in the valence region, the hydrogen bands and helium bands are well separated. At higher pressure, the widths of all bands increase as a result from the enhanced state dispersion. This reveals that the intermolecular interaction within the H_2 units increase as a direct effect of compression, and the interaction between hydrogen and helium is enhanced also as seen from

the apparent orbital overlap from -5 eV to the Fermi level (Figure 4.10 (d)). This is a clear indication of certain degree of interaction between them. Thus, at this point, the question can no longer be, is there any sort of interaction between helium and hydrogen in the P-1 structure? But what? In other words, what is the interaction between helium and hydrogen in this structure and how strong is this interaction. For now, we know that it is strong enough to support the formation and stability of the structure.

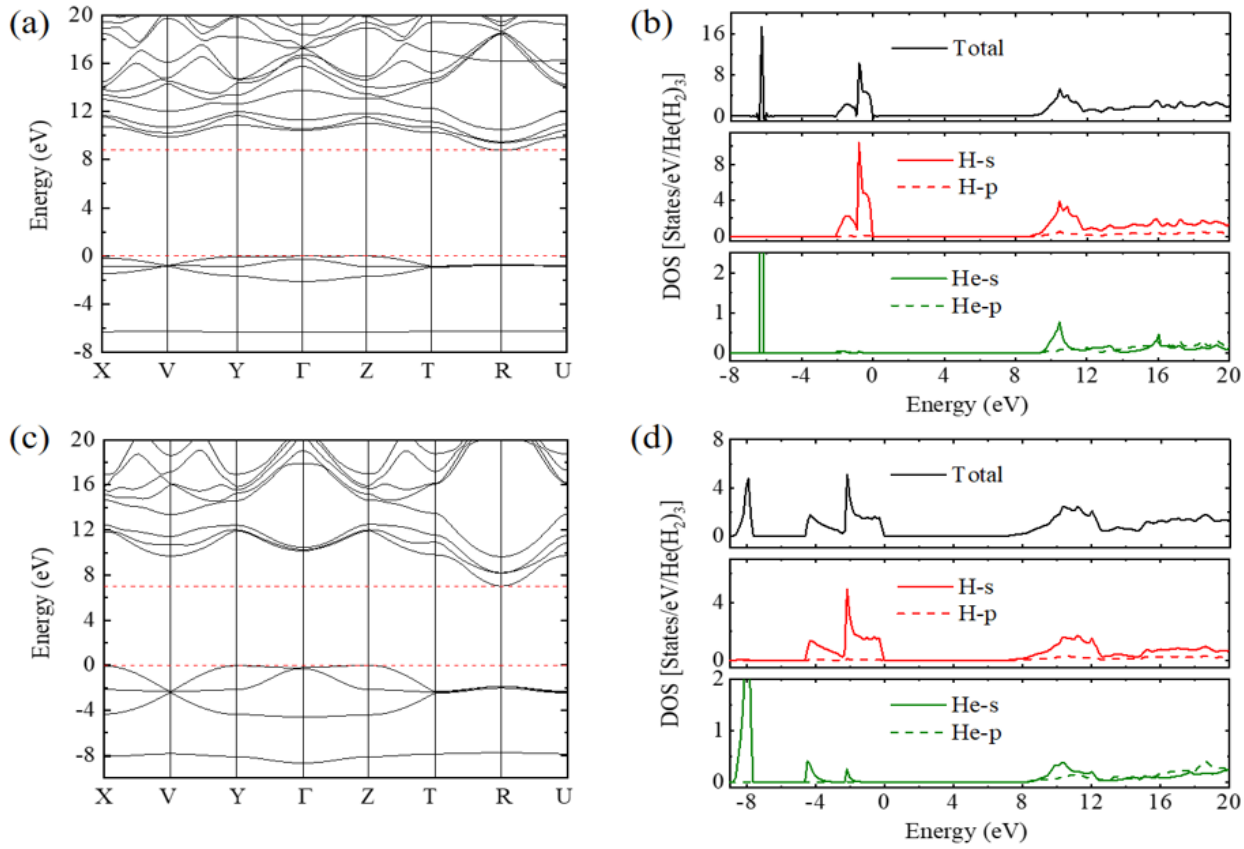

Figure 4.10: (a) Electronic band structure and (b) projected density of states for the P-1 structure of $HeH(_2)_3$ at 0 GPa. (c) Electronic band structure and (d) projected density of states for P-1 structure at 8 GPa [180].

Electron localization function (ELF) is an essential tool in the identification of places in a crystal structure where localization of electrons can be found. When applied to a crystal structure, such calculation can be used to distinguish between core and valence electrons as well as reveal the presence or absence of covalent bonds or non bonding pair of electrons.

The result of the ELF calculation in the P-1 structure [Figure 4.4 (b)] shows that the two hydrogen atoms in the middle of the unit cell are covalently bonded as their electron clouds completely overlap. In addition, the result shows that any interaction between helium and hydrogen in this structure has to be closed shell in nature as one may have guessed.

4.3.3 Topological Analysis

The reaction:

$$He + 3H_2 \rightarrow He(H_2)_3 \tag{4.1}$$

is predicted to be exothermic with reaction enthalpy of about -0.05 eV/atom at 0 GPa. Furthermore, phonon calculations have shown that the compound is dynamically stable at 0 GPa and higher pressures. Having also seen that the presence of helium is very important to the formation and stability of the P-1 structure, we now seek to understand the nature of He-H interaction in this compound as well as the evolution of such interaction with pressure. Topological analysis of charge density at bond critical points (BCPs) where gradient of the charge density is zero was done by using quantum theory of atoms in molecules (AIM) [28]. In this method, the charge density at the critical point ($\rho(r_{BCP})$) and its Laplacian ($\nabla^2\rho(r_{BCP})$) can reveal essential information about the strength and type of interaction. The magnitude of the charge density indicates the relative strength of the bond while its Laplacian determines the characteristics of interatomic interaction. A negative Laplacian is associated with covalent bonding whereas a positive Laplacian may be attributed to closed shell interactions such as dihydrogen, hydrogen bonds and vdW interactions. The potential energy density ($V(r_{BCP})$), kinetic energy density ($G(r_{BCP})$), total energy density ($H(r_{BCP})$) and bond dissociation energy ($E_{BD}(r_{BCP})$), at the bond critical points which are essential quantities in characterizing bonding strength and type can be computed from $\rho(r_{BCP})$ and $\nabla^2\rho(r_{BCP})$ as:

$$V(r_{BCP}) = \frac{\hbar^2}{4m}\nabla^2\rho(r_{BCP}) - 2G(r_{BCP}) \tag{4.2}$$

where,

$$G(r_{BCP}) = \frac{3}{10}(3\pi^2)^{2/3}\rho^{5/3}(r_{BCP}) + \frac{1}{6}\nabla^2\rho(r_{BCP}) \tag{4.3}$$

[183] and

$$H(r_{BCP}) = V(r_{BCP}) + G(r_{BCP}); E_{BD} = -\frac{1}{2}V(r_{BCP}) \tag{4.4}$$

At 0 GPa, topological analysis revealed bond critical points between helium atom and each of the distinct hydrogen atoms in the structure. This is an indication that there exists a quantifiable degree of interaction between helium and hydrogen in the P-1 structure at ambient conditions. The interatomic distances earlier calculated (in Figure 4.4 (c)) are accurately reproduced. Calculated $\rho(r_{BCP})$ at BCP for shortest helium hydrogen contacts are 0.019 eÅ^{-3}, 0.0174 eÅ^{-3} and 0.0155 eÅ^{-3} for He-H(1), He-H(2), and He-H(3) respectively. Multiplicity of all these interactions is 2 as we have already established in Figure 4.4. Calculated $\nabla^2\rho(r_{BCP})$ for these interactions are 0.266 eÅ^{-5} for He-H(1), 0.243 eÅ^{-5} for He-H(2) and 0.207 eÅ^{-5} for He-H(3). These $\rho(\mathrm{r}_{BCP})$ values are much lower than the expected values for conventional hydrogen bonds (0.04 to 0.24 eÅ^{-3}) [178]. The calculated Laplacian for these interactions are all positive, which identify the closed shell nature of the interaction. All other calculated parameters at the bond critical points for these interactions at 0 GPa are presented in Table 4.1. In addition, a complete table of all other BCPs in the structure at 0 GPa can be found in the Table 4.5. All the results are consistent with vdW interaction and comparable in strength with those found in He-O closed shell interactions for the helium filled ice II [184]. The calculated Bader charges also confirm that the $He(H_2)_3$ compound is dominated by vdW interaction at 0 GPa with an appearance of small but non negligible interaction between He and H (see Table 4.3).

At 8 GPa, the calculated $\rho(\mathrm{r}_{BCP})$ for He-H(1), He-H(2), and He-H(3) contacts are 0.051 eÅ^{-3}, 0.049 eÅ^{-3} and 0.050 eÅ^{-3}, respectively, which are notably enhanced from the ambient pressure values and reach the lower bound of the charge density for hydrogen bonding. The respective $\nabla^2\rho(r_{BCP})$ are 0.783 eÅ^{-5}, 0.746 eÅ^{-5} and 0.755 eÅ^{-5}, which are also increased from the ambient values. Table 4.2 shows all the calculated parameters at these three BCPs between helium and hydrogen at 8 GPa. A complete table of all other BCPs in the structure at 8 GPa is shown in Table 4.6. To put these results in perspective, we performed the same analysis on the pure elemental structures at 0 GPa and 8 GPa. In the $P6_3/m$ hydrogen, at 0 GPa, non-covalent H-H contacts have $\rho(\mathrm{r}_{BCP})$ that range from 0.029

eÅ^{-3} to 0.035 eÅ^{-3} with corresponding $\nabla^2\rho(r_{BCP})$ that goes from 0.365 eÅ^{-5} to 0.436 eÅ^{-5} as shown in Table 4.7 whereas at 8 GPa, $\rho(\mathrm{r}_{BCP})$ for the same contacts are from 0.069 eÅ^{-3} to 0.077 eÅ^{-3} with corresponding $\nabla^2\rho(r_{BCP})$ having values from 0.647 eÅ^{-5} to 0.857 eÅ^{-5} (see Table 4.8). Thus, it appears the strength of the He-H contacts in $He(H_2)_3$ crystal may reach that of hydrogen bonding when it is compressed. Conventional hydrogen bonds have been reported to have $\rho(\mathrm{r}_{BCP})$ in the range 0.04 to 0.24 eÅ^{-3} and $\nabla^2\rho(r_{BCP})$ 0.58 to 3.35 eÅ^{-5} [178]. Meanwhile, at 0 GPa, He-He contact in the pure He hexagonal closed packed structure has $\rho(\mathrm{r}_{BCP})$ value of 0.044 eÅ^{-3} and $\nabla^2\rho(r_{BCP})$ of 1.109 eÅ^{-5} that increased to 0.061 eÅ^{-3} and 1.439 eÅ^{-5} respectively at 8 GPa (see Table 4.9). Although these results are reported as obtained, it is important to point out that future work is required to completely understand all the properties and the stabilization mechanism of this $He(H_2)_3$ compound. In particular, the high-pressure field has in recent years seen the emergence of atypical new compounds from chemical reactions that do not result in the formation of local chemical bonds [56]. Perhaps, future theoretical and experimental analysis on the $He(H_2)_3$ compound could give significant insight to the rapidly increasing classes of compounds formed without an actual chemical bond [185]. Meanwhile the limitation of standard DFT tools to properly account for the nuclear quantum effect and anharmonicity in hydrogen at low temperature region is well known [46, 186]. A very important future work would be to apply ab initio path-integral molecular dynamics (PIMD) or path integral Monte Carlo (PIMC) calculations on all these phases ($He(H_2)_3$, H and He) before comparing the enthalpy so as to properly account for these effects.

It is worth noting that although the $He(H_2)_3$ compound possesses lower internal energy than the combination of constituent elements throughout the pressure range of consideration, the contribution of pressure-volume work to the enthalpy of the system triggers the decomposition of the compound at the aforementioned pressure (see Figure 4.11). In addition, despite the increase in strength of the interaction between helium and hydrogen in the compound with pressure, which is evident with the reduction in interatomic distances, and supported by the comparison of the internal energy, the pressure-work contribution to the enthalpy grows faster in the compound than in the constituent elements and becomes significant enough to

induce decomposition.

Table 4.1: Topological properties at the BCPs for all He-H contacts in the P-1 structure at 0 GPa [180].

Bond type	d [Å]	Multiplicity	$\rho(r_{BCP})$ [eÅ^{-3}]	$\nabla^2\rho(r_{BCP})$ [eÅ^{-5}]	G (kJ/mol)	V (kJ/mol)	H (kJ/mol)	E_{BD} (kJ/mol)
He—H1	2.604	2	0.019	0.266	5.247	-3.259	1.987	1.629
He—H2	2.650	2	0.017	0.243	4.779	-2.937	1.841	1.469
He—H3	2.708	2	0.016	0.207	4.065	-2.485	1.580	1.242

Table 4.2: Topological properties at the BCPs for all He-H contacts in the P-1 structure at 8 GPa [180].

Bond type	d [Å]	Multiplicity	$\rho(r_{BCP})$ [eÅ^{-3}]	$\nabla^2\rho(r_{BCP})$ [eÅ^{-5}]	G (kJ/mol)	V (kJ/mol)	H (kJ/mol)	E_{BD} (kJ/mol)
He—H1	2.191	2	0.051	0.783	16.387	-11.450	4.936	5.725
He—H2	2.198	2	0.050	0.755	15.820	-11.073	4.747	5.537
He—H3	2.708	2	0.016	0.746	15.589	-10.850	4.739	5.425

Table 4.3: Bader charge on all atoms in the P-1 structure at 0 GPa [prime denote symmetry equivalent atom] [180].

Atom	Charge
He	2.014
H1 ; H1'	1.008 ; 0.986
H2 ; H2'	1.009 ; 0.987
H3 ; H3'	1.009 ; 0.988

Table 4.4: Bader charge on all atoms in the P-1 structure at 8 GPa [prime denote symmetry equivalent atom] [180].

Atom	Charge
He	2.024
H1 ; H1'	1.004 ; 0.988
H2 ; H2'	1.003 ; 0.988
H3 ; H3'	1.004 ; 0.988

Table 4.5: Topological properties at the BCPs for all other interactions in the $He(H_2)_3$ structure at 0 GPa. M is the multiplicity of the interaction [180].

Bond type	d [Å]	Multiplicity	$\rho(r_{BCP})$ [eÅ^{-3}]	$\nabla^2\rho(r_{BCP})$ [eÅ^{-5}]	G (kJ/mol)	V (kJ/mol)	H (kJ/mol)	E_{BD} (kJ/mol)
H1—H1	0.748	1	1.806	-32.043	256.365	-1385.320	-1128.950	692.660
H2—H2	0.749	1	1.804	-31.804	258.620	-1383.310	-1124.690	691.655
H3—H3	0.750	1	1.803	-31.934	255.740	-1381.100	-1125.360	690.550
H3—H2	2.514	2	0.032	0.357	7.519	-5.319	2.199	2.660
H3—H1	2.552	2	0.030	0.334	6.983	-4.870	2.112	2.435
H2—H1	2.623	2	0.026	0.289	5.958	-4.045	1.913	2.022

Table 4.6: Topological properties at the BCPs for all other interactions in the $He(H_2)_3$ structure at 8 GPa. M is the multiplicity of the interaction [180].

Bond type	d [Å]	Multiplicity	$\rho(r_{BCP})$ [eÅ^{-3}]	$\nabla^2\rho(r_{BCP})$ [eÅ^{-5}]	G (kJ/mol)	V (kJ/mol)	H (kJ/mol)	E_{BD} (kJ/mol)
H1—H1	0.742	1	1.869	-39.009	179.090	-1420.48	-1241.38	710.24
H2—H2	0.743	1	1.866	-38.851	179.780	-1417.56	-1237.78	708.78
H3—H3	0.743	1	1.866	-38.853	179.320	-1416.69	-1237.37	708.34
H3—H2	2.096	2	0.080	0.850	20.099	-17.038	3.061	8.519
H3—H1	2.098	2	0.078	0.844	19.820	-16.646	3.173	8.323
H2—H1	2.111	2	0.077	0.816	19.183	-16.140	3.042	8.070

Table 4.7: Topological properties at the BCPs for non-covalent H-H contacts in $P6_3/m$ Hydrogen structure at 0 GPa [180].

Bond type	d [Å]	Multiplicity	$\rho(r_{BCP})$ [eÅ^{-3}]	$\nabla^2\rho(r_{BCP})$ [eÅ^{-5}]	G (kJ/mol)	V (kJ/mol)	H (kJ/mol)	E_{BD} (kJ/mol)
H1—H3	2.540	6	0.035	0.436	9.060	-6.257	2.803	3.128
H2—H3	2.608	6	0.030	0.355	7.350	-5.044	2.305	2.522
H1—H2	2.607	12	0.029	0.365	7.478	-5.016	2.462	2.508

Table 4.8: Topological properties at the BCPs for non-covalent H-H contacts in $P6_3/m$ Hydrogen structure at 8 GPa [180].

Bond type	d [Å]	Multiplicity	$\rho(r_{BCP})$ [eÅ^{-3}]	$\nabla^2\rho(r_{BCP})$ [eÅ^{-5}]	G (kJ/mol)	V (kJ/mol)	H (kJ/mol)	E_{BD} (kJ/mol)
H1—H3	2.072	6	0.077	0.857	19.877	-16.419	3.458	8.210
H2—H3	2.174	6	0.075	0.802	18.762	-15.674	3.086	7.837
H1—H2	2.227	12	0.069	0.647	15.38	-13.142	2.238	6.571

Table 4.9: Topological properties at the BCPs for He-He contact in HCP He structure [180].

Bond type	d [Å]	Multiplicity	$\rho(r_{BCP})$ [eÅ^{-3}]	$\nabla^2\rho(r_{BCP})$ [eÅ^{-5}]	G (kJ/mol)	V (kJ/mol)	H (kJ/mol)	E_{BD} (kJ/mol)
He—He (0GPa)	2.241	2	0.044	1.109	21.885	-13.548	8.337	6.774
He—He (8GPa)	2.130	2	0.061	1.439	29.049	-18.909	10.140	9.454

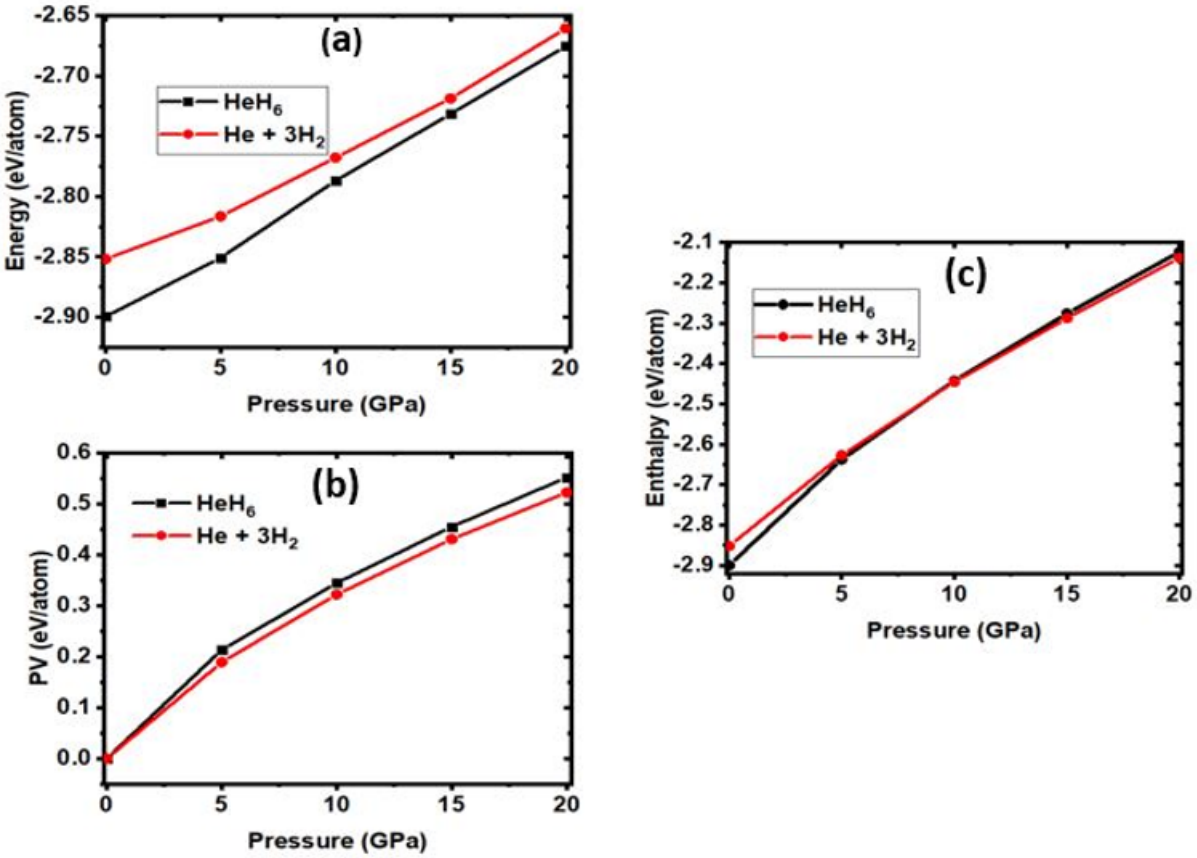

Figure 4.11: (a) Internal energy contribution to the enthalpy, (b) pressure-volume work contribution to the enthalpy, (c) enthalpy of the $He(H_2)_3$ structure and the appropriate combination of the constituent elements [180].

4.4 Conclusion

We report a stable helium−hydrogen compound formed at high pressures. It has $He(H_2)_3$ stoichiometry, belongs to the triclinic P-1 space group, as well as an arrangement of atoms that showcases the importance of the presence of helium to the formation and stability of the structure. Phonon dispersion curve reveals dynamical stability of the structure at ambient conditions as well as a higher pressure of 8 GPa, hence in principle, experimentally accessible. Topological analysis of electron density at the bond critical points shows there exists weak vdW interaction between helium and hydrogen in the $He(H_2)_3$ crystal. This predicted compound will not only give a twist to the chemistry of helium reactivity but also contribute greatly to our understanding of rapidly increasing classes of compounds formed without an actual chemical bond.

Chapter 5

A MACHINE LEARNING POTENTIAL FOR SODIUM

5.1 Introduction

Under ambient pressure, alkali metals are known to exhibit very simple electronic band structures that can be described by a nearly free-electron model. With increasing pressure, some alkali metals undergo series of structural phase transitions from a very well symmetric body-centered cubic (BCC) metallic phase to insulating phases accompanied with a decrease in symmetry. A transformation from BCC to FCC is known to be apparent in cesium at 2.2 GPa whereas such transformation takes about 65 GPa to be triggered in sodium [187, 188]. Upon further increase in pressure, they transform to several varieties of lower-symmetry and mainly complex crystal structures that include distorted variants of BCC as reported in lithium and sodium [188, 189] to an incommensurate composite structure in rubidium [190, 191]. Several experimental studies have established that by increasing pressure at room temperature sodium transforms from BCC phase to FCC at 65 GPa and then to a relatively complex body-centered cubic cI16 structure with 16 atoms in the unit cell at 103 GPa [189, 192]. Compressing sodium above 118 GPa, it takes a primitive orthorhombic oP8 which then transforms to an incommensurate t19 phase at about 125 GPa [193]. Continued compression to above 160 GPa produced several phases [192, 193]. Theoretical calculations proposed that these phases could include the tetragonal β-Sn type structure of cesium IV, orthorhombic oC8 structure of α-gallium [194, 195]. Interestingly, because of Na atoms pairing, calculations showed that the α-gallium phase possesses zero band gap above 800 GPa [194].

Properties of materials can undergo unconventional changes such as from metallic to semiconducting or insulating at high pressure. For instance in a recent experiment above 200 GPa, it was observed that sodium undergoes a pressure induced transition from metal to an optically transparent phase with a distorted double hexagonal hP4 symmetry [196]. The appearance of this dense insulating phase was ascribed to p-d hybridization of valence electrons rather than atom pairing [196]. Notable amount of experimental and theoretical work on the Na has so far been done at temperatures above 200 K with most reported experiment performed at room temperature. It is expected that several interesting phase transitions can be exhibited by Na as well as other alkali metals at high pressures and low temperatures. For instance, at temperature below 35K and atmospheric pressure, BCC-Na was reported to undergo a transition to one or more rhombohedral structures, however, exact nature of these phases have so far remained unexplained [197, 198]. The cI16 structure is a simple distortion of BCC in which atoms undergo a displacement along the body diagonal directions of the cubic unit cell, thus there exists a good chance that a similar transition to another interesting structure at low temperatures could occur in the BCC-like cI16 phase [199]. Meanwhile, previous report shows that at about 120 GPa, sodium may crystallize in numerous complex low-symmetry crystals containing between 50-512 atoms in a unit cell [193]. The melting line of sodium shows some unusual behaviour with reliable measurements showing a pressure induced reduction in the melting line from about 1000 K at 30 GPa to around 300 K at 120 GPa. This anomaly at about 120 GPa has been associated with the presence of many phases around this pressure at slightly different temperatures that are yet to be identified or characterized [192, 200]. Additionally, as of present, very little is known about the structural behaviour of sodium at 120 GPa and low temperatures and further studies become important.

The aforementioned complexity in the phase diagram of sodium coupled with challenges of experimental procedure in getting a detailed characterization of high pressure high temperature phases [192] has made theoretical methods particularly molecular dynamics and metadynamics very important tools for investigating complex behaviour in dense sodium. A significant contribution to the indispensability of these methods depend strongly on the

quality description of the potential energy surface. DFT based MD and metadynamics simulations often provide good frameworks for modelling several phases of sodium as well as any transition between these phases but they are computationally expensive and impracticable for lengthy simulations and large systems. Another primary downside of small-sized simulation is that the phase transition mechanism with collective atomic motions increase the activation barrier [201, 202]. A common practise to overcome this limitation is by overpressurization. While doing so may enhance the kinetics and push the system to a new state at the time scale of few picoseconds, it could impinge the transition mechanism. For these reasons, constructing accurate, reliable and computationally efficient potentials that can describe various properties in sodium at high pressure are now being explored. A lot of available potentials for sodium created from pseuodopotential theory [203, 204] and embedded atom model [205, 206] are often limited to a small P-T region of the phase diagram and do not readily capture all its properties accurately. Furthermore, the transferability of these potentials are not always satisfactory. Meanwhile an accurate description of the interatomic potentials is important in atomistic simulation. Thus, creating reliable potentials that can capture the atomic interactions with accuracy similar to that of the commonly used DFT methods howbeit at a reduced computational cost even for a larger systems will be very important. In recent times, machine learning (ML) approach has been employed particularly because of the ease of representing complex functions. A sizable amount of ML potentials have been developed in recent times with the use of techniques including artificial neural networks (ANN) [207, 208, 209], Gaussian process regression (GPR) [210, 211, 212], support vector machines [213] kernel ridge regression [214, 215] and so on. They have shown good accuracy and transferabilty close to those of quantum-mechanical simulations and with a lesser computational cost. This has resulted in a more trackable computational simulations of large systems over a long time as often required in crystallization and phase transitions. The PES of materials can be reconstructed using machine learning algorithms on the data obtained from first principles calculations to get a new sets of interatomic potentials called machine learning potential (MLP) [210, 216, 217, 218, 219, 220]. Previous applications of this method to large scale atomic systems show a satisfactory compromise between accuracy and efficiency [221, 222, 223].

In this study, we present a MLP for sodium based on the Guassian process regression (GPR) method and weighted atom-centered symmetry functions (wACSFs) representation of the PES. In this approach, the sodium PES is described by five data sets that represent different regions of the PES with each data set consisting of three element groups, i.e., total energies, interatomic forces, and stress tensors of the cell, which were constructed by DFT calculation using the Vienna ab initio simulation Package (VASP) [21]. The data sets are from crystal BCC, FCC, cI16, oP8, tI19, hP4 and several randomly generated structures of sodium for pressures up to 120 GPa and temperatures up to 300 K. We demonstrate that by learning from a DFT based calculations, this new ML potential is capable of reproducing numerous properties of sodium phases in this P-T region with an accuracy comparable to that of the underlying DFT calculations.

5.2 Methods

5.2.1 First Principles DFT Calculation details

The first principles DFT calculations were performed with VASP [21] in which the interaction of ions and electrons was captured by the projector augmented wave (PAW) [20, 123] method in addition to treating the exchange-correlation functional with the generalized gradient approximation of Perdue-Burke-Ernzerhof (PBE) [124] method. A cut off of 1360 eV was applied to the plane wave basis set and the Brillouin zone was sampled with a dense k-point grid of 0.5Å^{-1} spacing to make sure the total energy converged to a few meV per atom. The molecular dynamics simulations based on DFT were done with VASP [21]. To construct one of the data sets for the machine learning algorithm, the MD simulations was performed using isothermal-isobaric (NpT) ensemble where the temperature was controlled with Langevin dynamics and the pressure was controlled with Parrinello-Rahman barostat. The timestep of 1.0 fs and a k-point grid with 0.5 Å^{-1} spacing were used to sample the first Brillouin zone for the bcc, fcc, cI16, Cs-IV, oP8, tI19 and hP4 sodium phases, with each phase consisting of 64 atoms.

5.2.2 Machine Learning Potential

For any system with large number of atoms and high degrees of freedom, a simple acceptable format of representing the total energy (E) of the system commonly used in the construction of empirical potentials is the sum of the local energies (ϵ_i) as a function of a descriptor (d_i) of all atoms in the system

$$E = \sum \epsilon_i(d_i). \tag{5.1}$$

In terms of application to condensed matter physics, the two integral components of any ML potential are the descriptor that represents a structure numerically in a distinctive approach, and the ML method that applies the descriptor as input to reconstruct the PES. Several descriptors have been presented among which atom centered symmetry functions (ACSF) [224], the bispectrum of neighbor density [225] and smooth overlap of atomic [226] positions have shown to be good for fitting PESs. To train the potentials, high dimensional neural networks and Guassian process regression have shown encouraging results. Any of the above descriptors and ML methods can be employed in constructing a ML potential. In this work, the applied descriptor and ML method are wACSF and GPR [210, 211, 212], respectively. A conventional ACSF descriptor is made of a set of radial and angular functions that represent the energetically relevant environment of an atom based on the positions of nearby atoms within a certain cutoff radius. A notable limitation in ACSF is that the number of symmetry functions scales unfavourably with increasing number of species in a chemical system and to overcome this limitation, wACSF was developed [227]. In wACSF, the descriptor is constructed in a manner that permits the symmetry functions to remain the same through the assignment of different weight parameters for each elements in the system. The radial and angular parts of the descriptor can be written as:

$$G_i^{rad} = \sum_j \omega_j e^{-\eta(R_{ij}-R_s)^2} f_c(R_{ij}) \tag{5.2}$$

$$G_i^{ang} = 2^{1-\zeta} \sum_{j,k\neq i} \omega_j\omega_k(1+\lambda\cos\theta_{ijk})^\zeta e^{-\eta(R_{ij}^2+R_{ik}^2+R_{jk}^2)} \times f_c(R_{ij})f_c(R_{jk})f_c(R_{jk}) \tag{5.3}$$

where ζ,λ, R_s, and η are parameters that can easily with adjusted. f_c is a cutoff function that describe the nearest regions around the central atom i, R_{ij} are the interatomic distances, and

$$\theta_{ijk} = \frac{\mathbf{R_{ij} \cdot R_{jk}}}{R_{ij}R_{jk}} \tag{5.4}$$

is the angle centered at atom i. ω_j and ω_k are the weight parameters that are used to differentiate the contributions of individual elements. Finally, the total energy as a function of individual atomic energies is fitted with the GPR model [210, 211, 212] to the data from all the DFT calculations. A more elaborate description of this ML method can be found in ref[228].

5.3 Results and Discussion

5.3.1 Construction of MLP

In order to sample the PES effectively, we applied five different data sets to capture several regions in it. The first data set is made of randomly generated structures from all the space groups with the application of CALYPSO [72]. It contains 4600 random structures that ensure a rough sampling of the PES. The number of Na atoms was between 10 to 21 and the volume per formula unit was between 7 - 37 Å^3. A self consistent calculation was then performed to obtain the total energies, stress tensors and interatomic forces for all the structures. As shown in the energy volume distribution in Figure 5.1, these structures (black square dots) are diversely distributed in the high energy area of the PES. This data was then used to train a rough ML potential. In the second data set, 1000 randomly generated structures were optimized using the rough ML potential. This optimization was performed with the atomic simulation environment package (ASE) [229]. The maximum number of cycle was set to 60 in the optimization. It must be noted that the MLP at this stage is very rough and cannot be efficient, therefore, it is important to use a small number of conjugate gradient (CG) cycle at this stage to prevent the structures from deviating too large from their respective local minima. DFT-based SCF calculation was then performed on these MLP optimized structures to get the second data sets shown as red square dots in Figure

5.1.

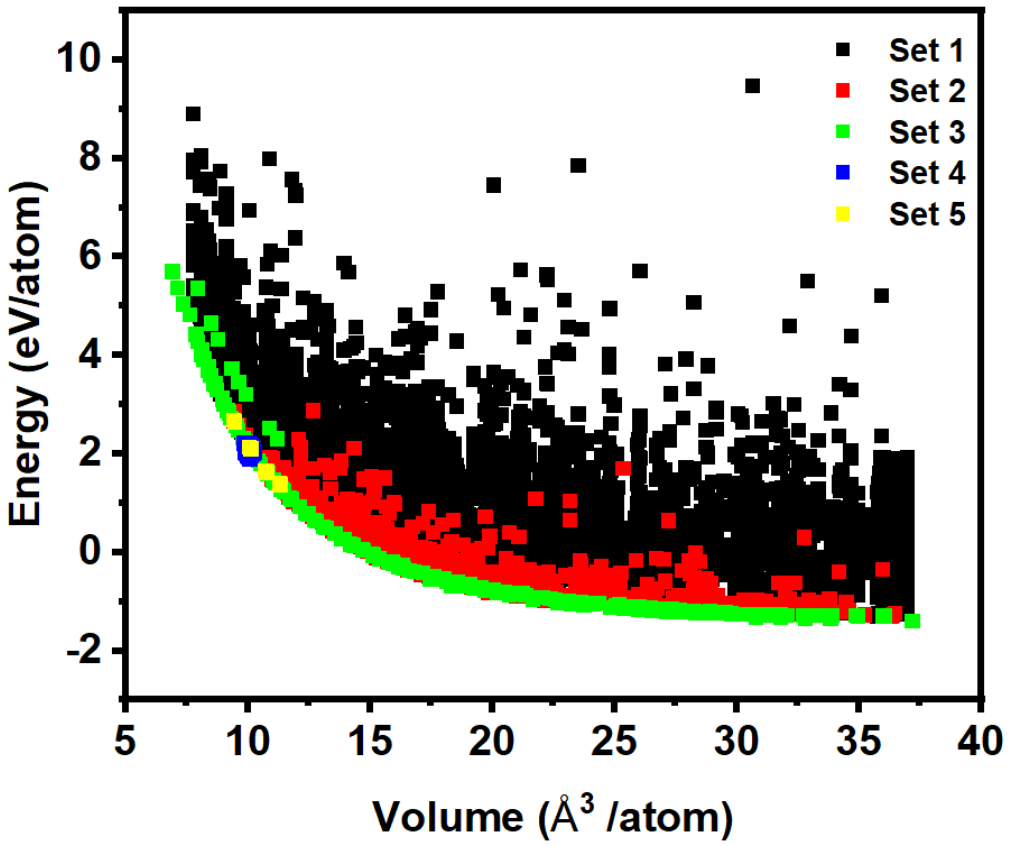

Figure 5.1: Distribution of energies and volumes for all structures in the training sets calculated using VASP. Different colours have been used to differentiates between the five data sets.

It can be clearly seen that the MLP optimization performed on these structures has significantly lower the highest energy in the distribution. Meanwhile, there are several known stable structures of Na that depict the local minima or lowest energy states on its PES. They include BCC, FCC, cI16, Cs-IV, oP8, tI19, R-3m and $P6_3/mmc$. To obtain a good potential, it is important to leverage these known local minima in the training data. Thus, data set three comprises of fully relaxed states of the aforementioned crystal structures at different volumes, which ascertain accurate capturing of the energy minima on the PES as shown with the green square dots on the energy volume distribution in Figure 5.1. One can see that some of the structures from the first and second sets of data have energies corresponding to

the minima energy region on the PES, this is an indication that the energy landscape has be well represented. Be that as it may, it is also important to ensure the training is done with some level of dynamical set as well as to account for anharmonic effect. Therefore, the fourth data set (blue square dots in Figure 5.1) was obtained from MD trajectories of a number of structures including FCC, BCC and cI16 at 120 GPa, 150 K and 300 K using simulation cells of 32 - 64 atoms with an NPT ensemble. The inclusion of these data sets can effectively describe the dynamical areas of the PES and also take care of anharmonic effect. Lastly, the data set five is made from 12 distorted structures of the cI16 phase. This data set is included to ensure that the potential can learn how to produce the Hessian matrix of sodium crystals. In Table 5.1, the number of structures used from each of the data set is shown. A total of 5074 training structures with 1554 test structures that cover a good range of the energy landscape can be very important for the MLP to be highly effective, as it learns from a wide range of relevant structures.

Table 5.1: Number of structures in training and testing configurations for each dataset.

Data set	Number of Training structures	Number of Test structures
1	3586	906
2	784	205
3	167	38
4	526	400
5	11	5
Total	5074	1554

5.3.2 Testing the MLP

The ability of the trained MLP to perform satisfactorily in estimating total energy, force, stress and structural optimization was tested as shown in Figure 5.2 a-c. Figure 5.3 a-d and Figure 5.4 a-e present the enthalpies of different known structures of sodium calculated at each of their respective stable region using the trained MLP and DFT. As can be seen in these figures, there is a remarkable agreement in the evolution of the enthalpies for all the structures. To further check if the MLP can be applied effectively to calculating other properties, the eigenvalues and eigenvectors of the Hessian matrix was computed with two different supercells containing 64 atoms and 128 atoms of the cI16 phase using the MLP and DFT. A comparison of the results is shown in Tables 5.2 and 5.3.

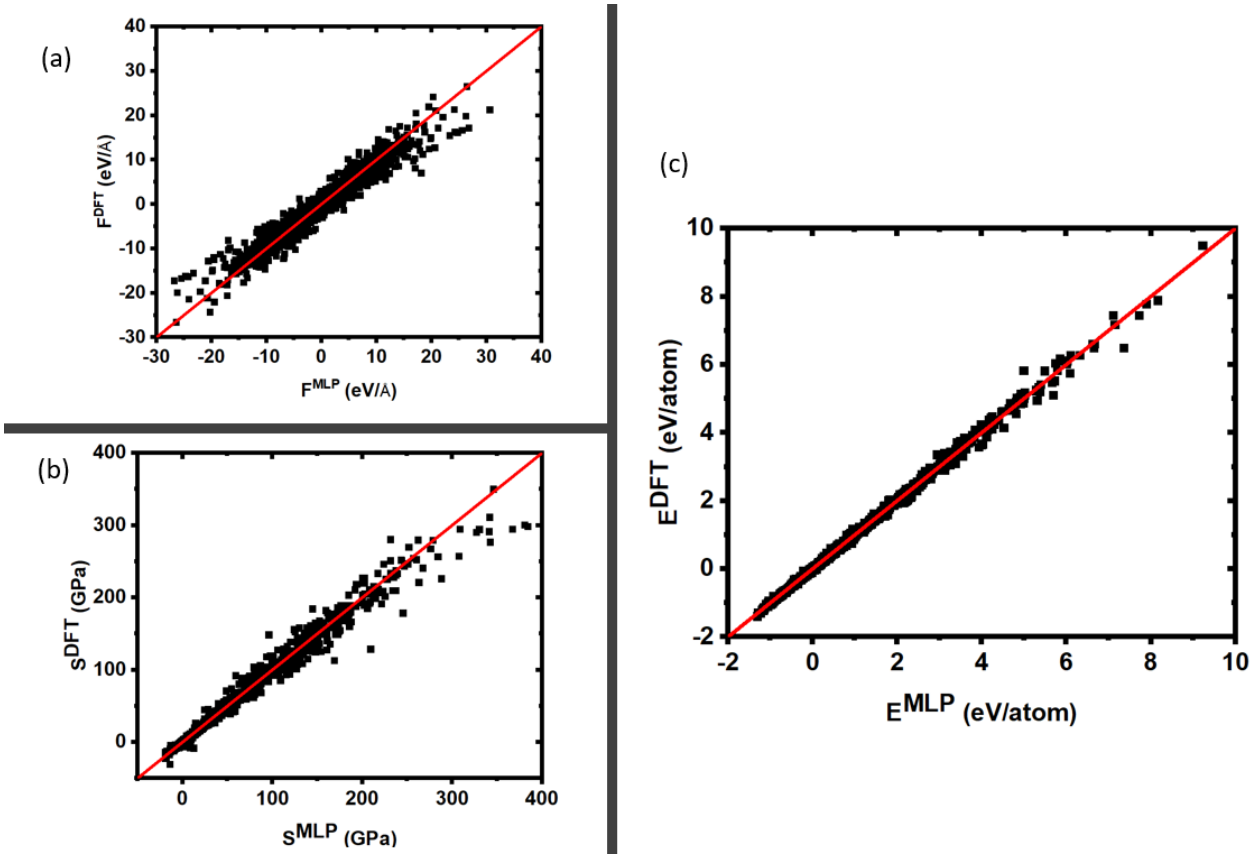

Figure 5.2: The calculated (a) force, (b) stress and (c) total energy for all data sets using MLP and DFT

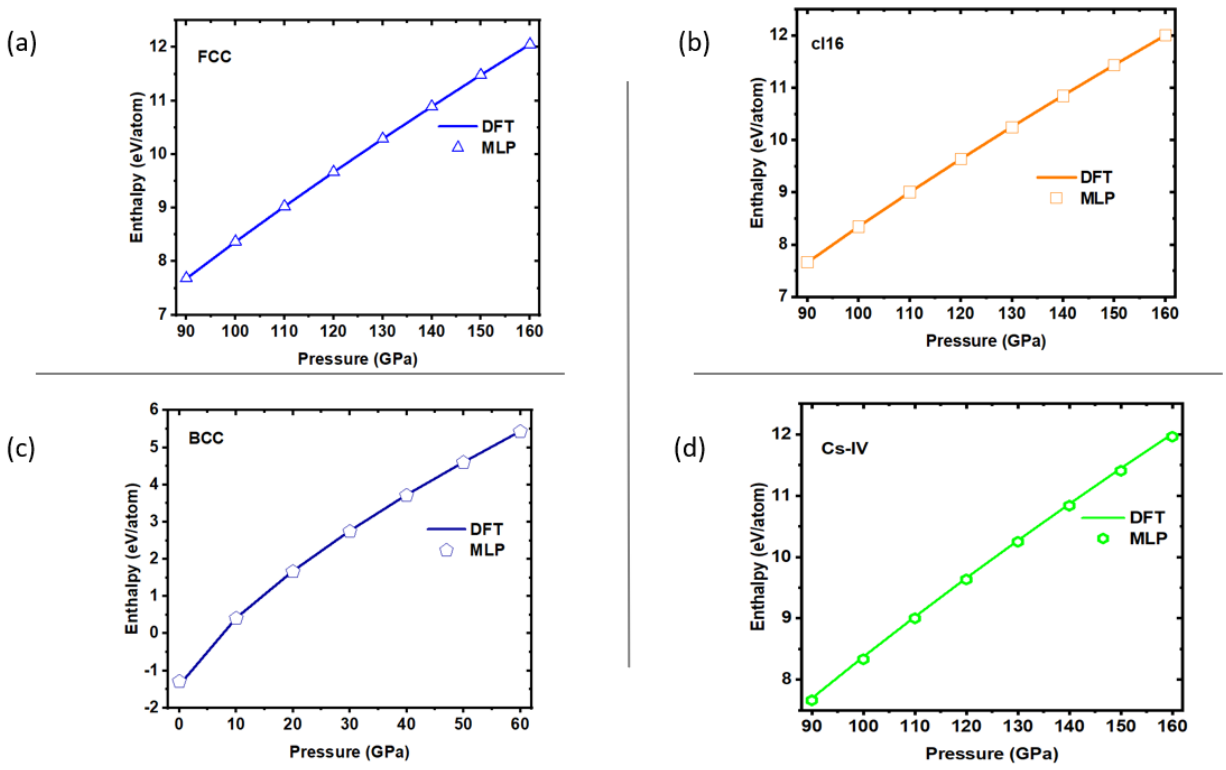

Figure 5.3: The calculated enthalpies for the FCC, cI16, BCC and Cs-IV phases of Na in their respective stable pressure range using DFT(lines) and MLP (points)

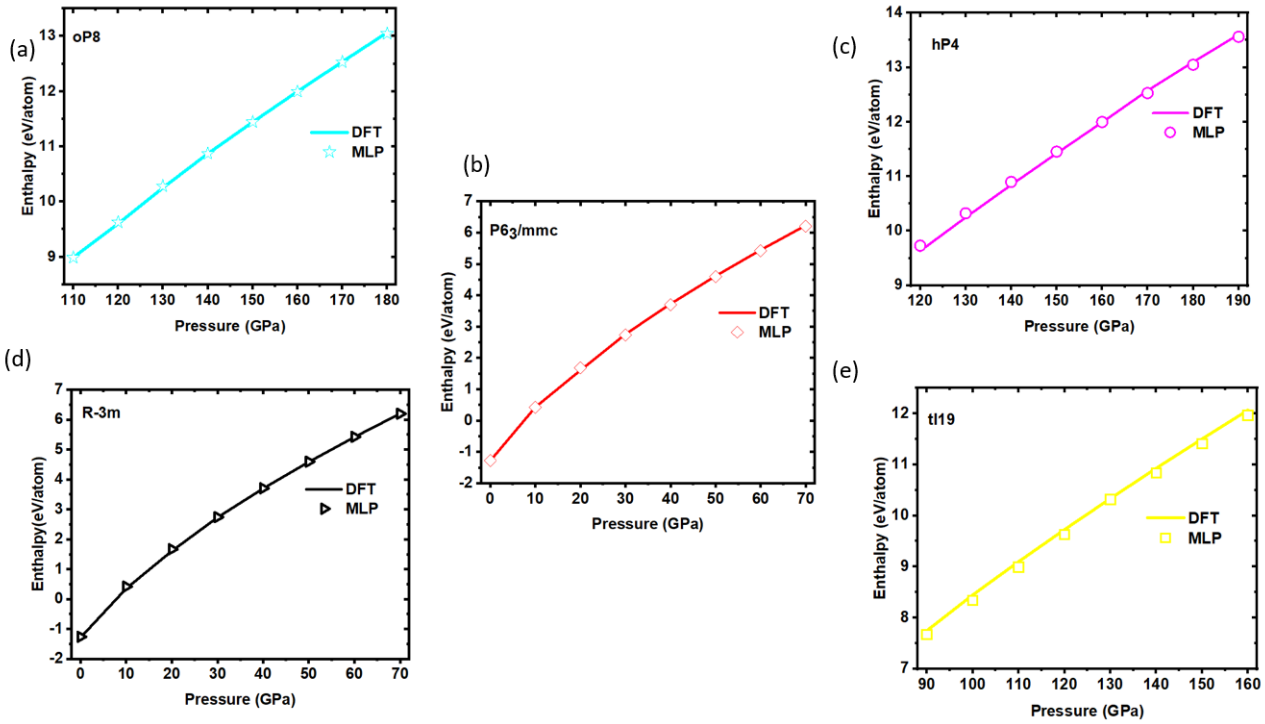

Figure 5.4: The calculated enthalpies for the oP8, P6$_3$/mmc,hP4 R-3m and tI19 phases of Na in the their respective stable pressure range using DFT(lines) and MLP (points)

Table 5.2: Eigenvalues (in unit of kbar Å) and corresponding eigenvectors of the Hessian matrix for cI16 phase consisting of 64 atoms at 0 K and 120 GPa calculated using MLP and DFT displacement value of 0.69Å. The data obtained from DFT are in brackets.

eigenvalues					
520(377)	520(3257)	1417(5203)	4205(9211)	4589(9261)	106039(109921)
eigenvectors (in column)					
0.0(0.70)	0.0(0.0)	0.0(-0.60)	0.71(0.0)	0.58(0.0)	0.40(0.38)
0.0(-0.71)	0.0(0.0)	0.0(-0.59)	-0.71(0.0)	0.58(0.0)	0.40(0.38)
0.0(0.0)	0.0(0.0)	0.0(0.54)	0.0(0.0)	-0.57(0.0)	0.82(0.84)
0.0(0.0)	0.0(1.0)	-1.0(0.0)	0.0(0.0)	0.0(0.0)	0.0(0.0)
1.0(0.0)	0.0(0.0)	0.0 (0.0)	0.0 (1.0)	0.0 (0.25)	0.0(0.0)
0.0(0.0)	1.0 (0.0)	0.0(0.0)	0.0(-0.25)	0.0(1.0)	0.0(0.0)

Table 5.3: Eigenvalues (in unit of kbar Å) and corresponding eigenvectors of the Hessian matrix for cI16 phase consisting of 128 atoms at 0 K and 120 GPa calculated using MLP and DFT with displacement value of 1.2Å. The data obtained from DFT are in brackets.

eigenvalues					
183(310)	470(365)	4179(417)	6272(2844)	16934(3399)	105336(104688)
eigenvectors (in column)					
0.0(0.0)	0.0(0.0)	-0.30(0.0)	0.65(0.81)	0.42(-0.13)	-0.56(-0.57)
0.0(0.0)	0.0(0.0)	0.16(0.0)	-0.69(-0.51)	0.44(-0.64)	-0.55(-0.58)
0.0(0.0)	0.0(0.0)	0.0(0.0)	0.0(-0.29)	-0.79(0.76)	-0.61(-0.58)
-1.0(0.56)	0.0(-0.65)	0.0(-0.52)	0.0(0.0)	0.0(0.0)	0.0(0.0)
0.0(0.67)	1.0(0.0)	0.0(0.74)	0.0(0.0)	0.0 (0.0)	0.0(0.0)
0.0(0.49)	0.0(0.76)	-0.94(-0.42)	-0.32(0.0)	-0.1(0.0)	0.1(0.0)

Table 5.4: Calculated zero pressure Bulk modulus and its derivative with respect to pressure for BCC and cI16 phases of sodium.

		K_0(GPa)	K_0'
BCC	MLP	30.5	2.58
	DFT	30.0	2.59
cI16	MLP	83.2	1.0
	DFT	82.3	1.0

It can be seen that the eigenvalues and eigenvectors from both calculations are closely matched. This indicates that the MLP can produce a potential energy well with an accuracy similar to that of the underlying DFT. Lastly to check the capability of the MLP to produce reliable results of elastic properties, the zero pressure bulk modulus (K_0) and its derivative (K_0') with respect to pressure for some sodium phases was computed with DFT and the MLP. The results (Table 5.4) show that the MLP performs excellently in estimating these elastic properties of sodium. In the next section, this well trained MLP will be applied in a metadynamics simulation to explore a possible phase transition in sodium at high pressure.

5.4 MLP Simulated Phase Transition in Sodium

Previous experiment based report has shown that at about 120 GPa, the cI16 phase of sodium can transform to numerous phases as a result of any small change in temperature and/or pressure that may include a simple structure such as oP8 with 8 atoms in a unit cell to complex structures with large number of atoms in a unit cell such as a primitive monoclinic structure (mP512) that has more than 500 atoms in the unit cell [193]. Simulating such transition and providing insight to some of the processes involve have been elusive theoretically because such simulations will require a large box and is therefore computationally unrealistic with a conventional DFT based calculations. In recent times however, such large scale simulations are now becoming trackable with the application of machine learning methods to material systems. To illustrate the significant improvements the application of MLP will bring to material discovery research in a foreseeable future, we have applied the well trained MLP in a metadynamics simulation on sodium at 120 GPa and 150 K. Details of the metadynamics approach to the simulation of phase transition in materials system had already been discussed in Chapter two.

The simulation box was built from a 4 ×4× 4 supercell of the cI16 phase consisting of 1024 atoms. A displacement value of 1.2 Å was found to be good enough in the computation of the Hessian matrix for this box. The eigenvalues and the corresponding eigenvectors for the

system of 1024 atoms are as shown in Table. 5.5. Setting the Guassian parameters to width (δ s) = 25 (kbar Å^3)$^{1/2}$ and height (W)= 625 kbar Å was found to be efficient in pushing the system into a new local minimum that is completely different from the starting configuration for the simulation performed at temperature of 150 K and hydrostatic pressure of 120 GPa. At each metastep, MD run of 0.8 ps using an NVT ensemble was performed.

Table 5.5: Eigenvalues (in unit of kbar Å) and corresponding eigenvectors of the Hessian matrix for cI16 phase consisting of 1024 atoms at 120 GPa calculated using MLP with displacement value of 1.2Å.

eigenvalues					
6252	6252	6252	18714	18714	222847
eigenvectors (in column)					
0.0	0.0	0.0	0.0	-0.817	-0.577
0.0	0.0	0.0	-0.707	0.408	-0.577
0.0	0.0	0.0	0.707	0.408	-0.577
0.177	-0.810	-0.560	0.0	0.0	0.0
-0.842	0.170	-0.512	0.0	0.0	0.0
0.510	0.562	-0.652	0.0	0.0	0.0

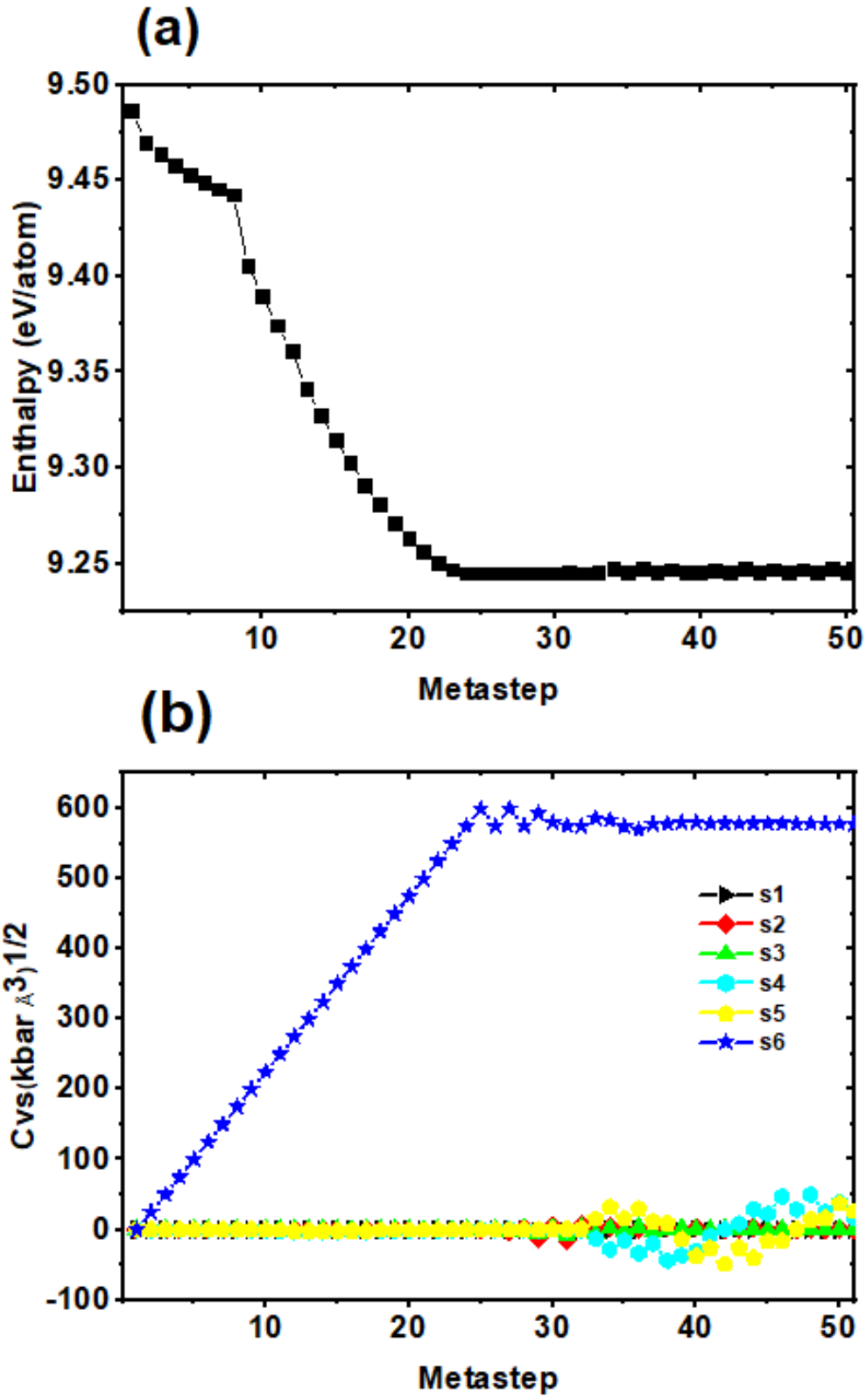

Figure 5.5: The evolution of the (a) enthalpy and (b) collective variables (CVs) in the metadynamics simulation.

Figure 5.5 (a) and (b) show the evolution of the enthalpy and that of the collective variables during the simulation. It can be seen clearly that there has been a transition to another phase at about the 26^{th} metastep. The snapshots at different metasteps show an obvious rearrangements of atomic configurations (see Figure 5.6). A comparison of the simulated x-ray diffraction pattern of the new phase (from metastep 50) with the pattern of the starting phase at 120 GPa and ambient temperature is shown in Figure. 5.7. It is important to emphasize that the goal of this part of the thesis was not to predict a new phase of sodium but to illustrate that a well trained MLP can be applied to large systems that may otherwise be difficult to handle by the mostly used DFT based potentials and by so doing, provide a notable improvement to our understanding of important physical processes such as growth and nucleation in crystal formation and phase transition. Be that as it may, this MLP simulated structure has not been reported previously either from experiment or theory for sodium and future work should be done to characterize and explore its properties. It is a tetragonal structure with space group $I4_1/ACD$ that contains 16 atoms in a unit cell. As one can clearly see from the diffraction pattern, it is different from the cubic cI16 structure which also has 16 atoms in its unit cell. For the cI16 structure to transform to the $I4_1/ACD$ phase, all the lattice constants undergo a significant change while the angles remain the same. a and b decrease by about 19% whereas c increases by about 48%, resulting in a slight volume drop.

Finally, to check if the result of this simulation is reproducible and also if the MLP approach in this simulation is scalable, the calculation is repeated with a $6 \times 6 \times 6$ simulation box that contains 3456 atoms of the cI16 phase. As done in the previous simulation, the temperature and pressure are 150 K and 120 GPa respectively. A displacement of 1.2 Å remains usable in the calculation of the Hessain matrix for this simulation box and the Guassian parameters are kept to the values applied in the previous simulation. Table 5.6 shows the calculated eigenvalues and their corresponding eigenvectors for this simulation box at 120 GPa and 0 K. In comparison with the $4 \times 4 \times 4$ simulation box, the eigenvalues of the Hessian matrix increase by about 40 % but the eigenvectors are still closely matched. Thus, one can expect the simulation performed with this box to locate the same potential energy well obtained with the box that contains 1024 atoms applied in the previous simulation.

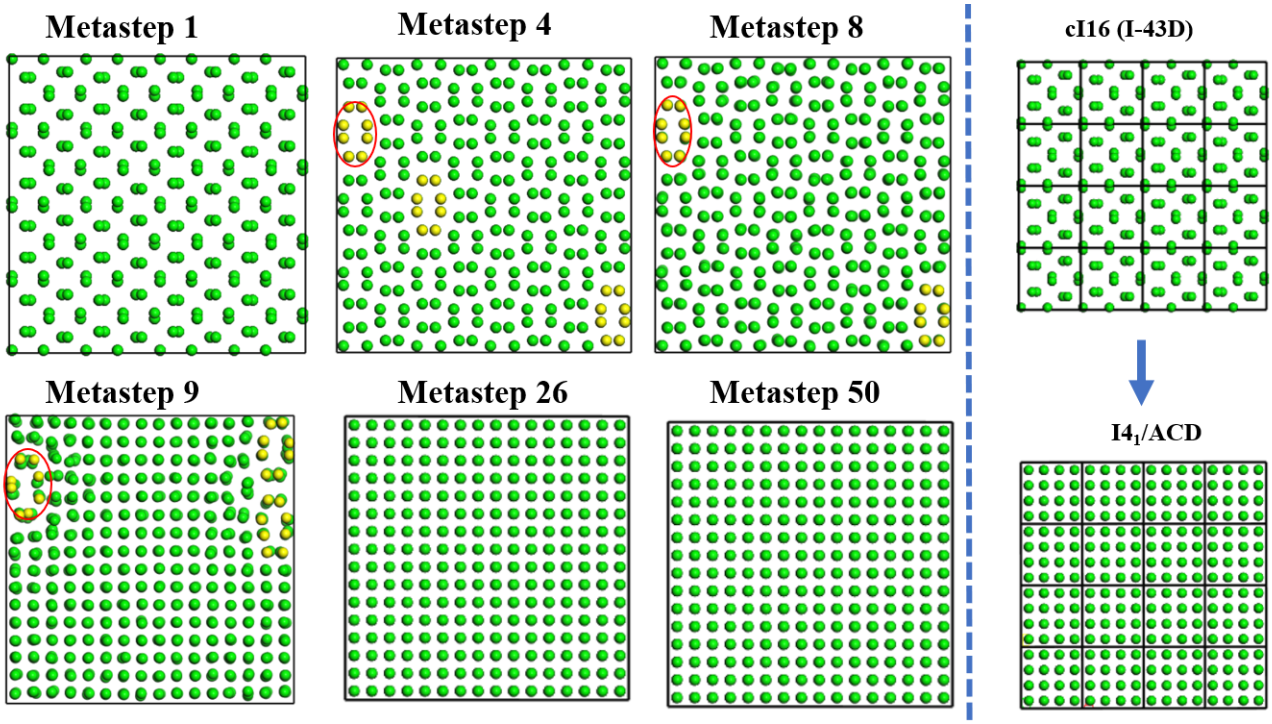

Figure 5.6: MLP simulated phase transition in sodium revealing important rearrangements of atomic configurations.

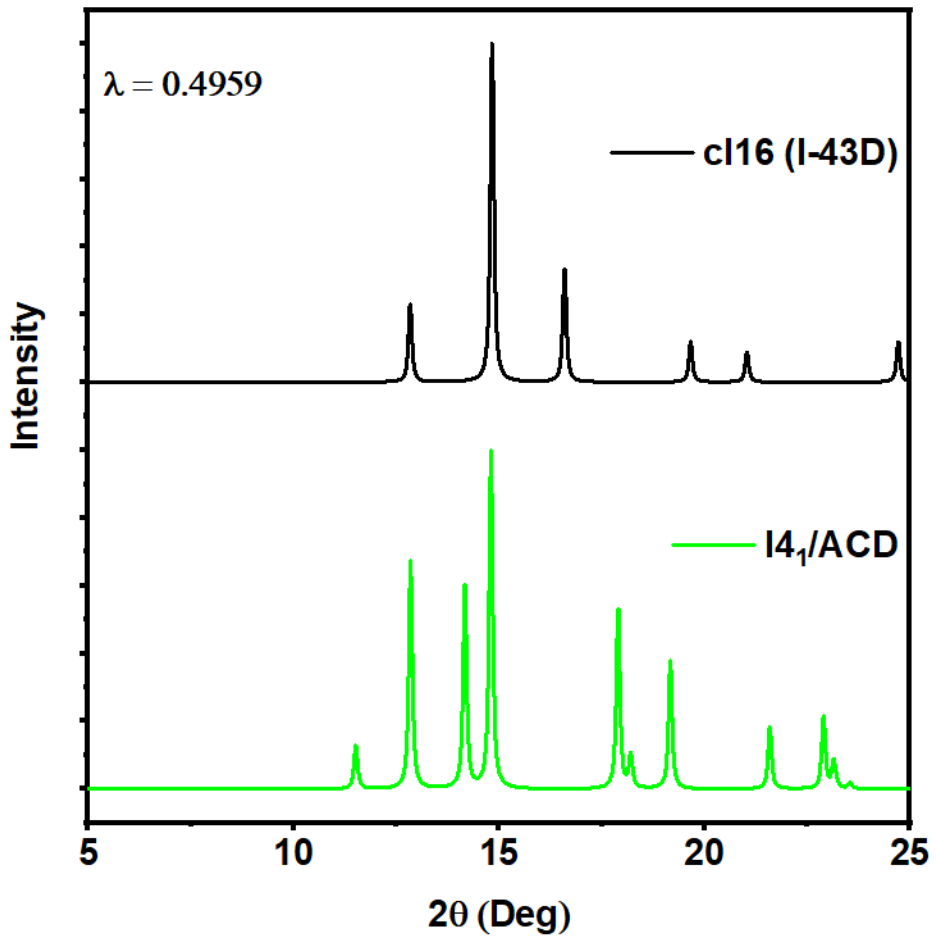

Figure 5.7: Simulated x-ray diffraction pattern for the cI16 and $I4_1/ACD$ sodium phases at 120 GPa and 0 K.

Table 5.6: Eigenvalues (in unit of kbar Å) and corresponding eigenvectors of the Hessian matrix for cI16 phase consisting of 3456 atoms at 120 GPa and 0 K calculated using MLP with displacement value of 1.2Å.

eigenvalues					
9960	9960	9960	21990	21990	335815
eigenvectors (in column)					
0.0	0.0	0.0	-0.817	0.0	-0.577
0.0	0.0	0.0	0.413	0.704	-0.577
0.0	0.0	0.0	0.403	-0.710	-0.577
0.384	-0.1	-0.918	0.0	0.0	0.0
-0.916	0.1	-0.392	0.0	0.0	0.0
0.119	0.991	-0.1	0.0	0.0	0.0

The evolution of the enthalpy and the collective variables during this simulation is shown in Figure 5.8. It is obvious that the simulation mechanism follows the same path as in the previous one except that the system spends longer time in the transition region in this case. This is expected because of the bigger size of the simulation box since it will take a longer time for heat to distribute throughout the entire bigger box. Snapshots taken at different metasteps in the simulation are shown in Figure 5.9. At metastep 13, the atoms begin to rearrange in a new order that starts from a small region (shown with the blue circle) and grows gradually throughout the entire simulation box as the simulation progresses. One can easily see that this simulation converges to the same local minima obtained in the previous simulation and can therefore conclude that the results are reproducible and the MLP method in this work is scalable.

Before concluding this chapter, I must point out that applying machine learning methods to condensed matter systems is still very new and there are lots of things unknown and several

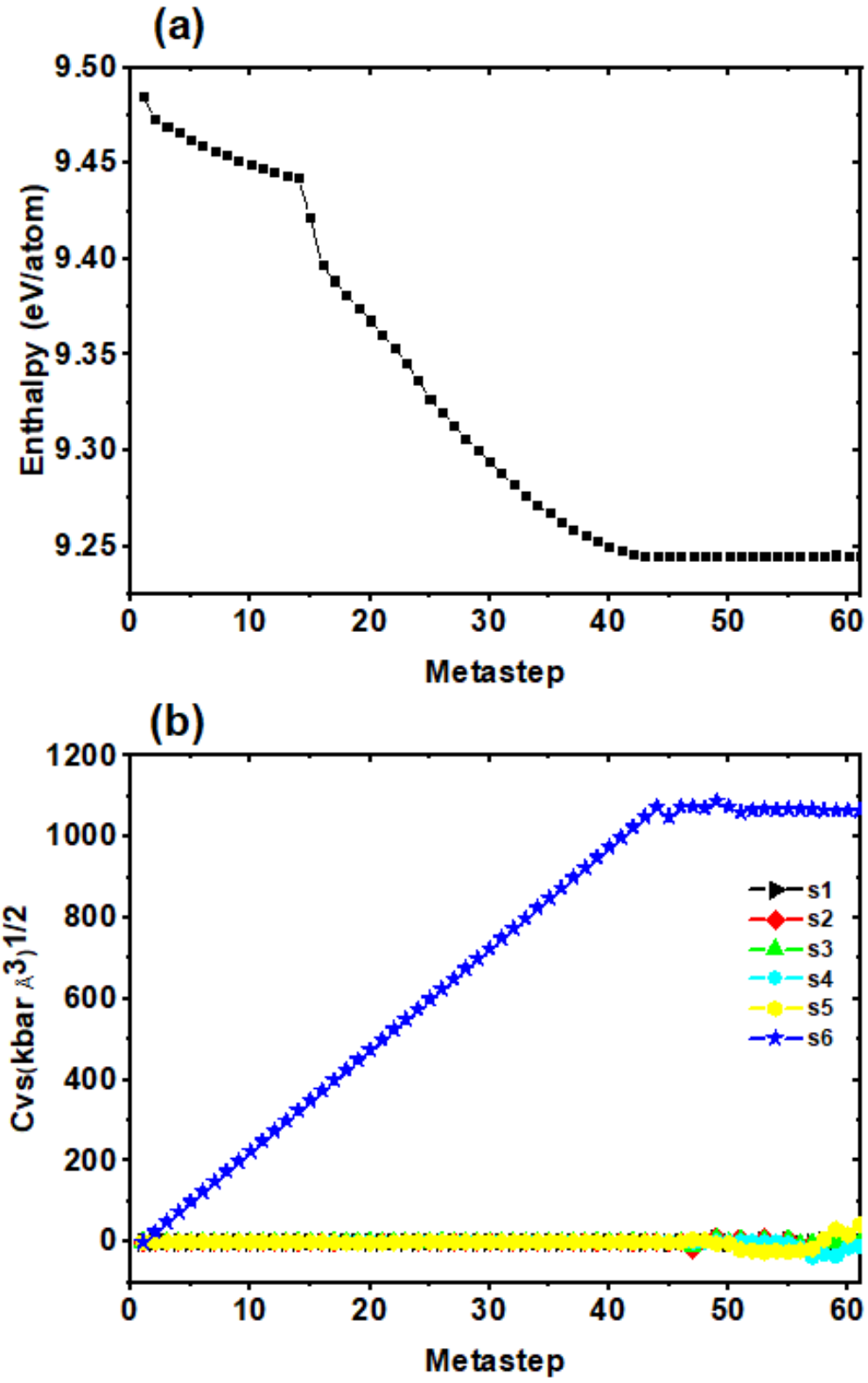

Figure 5.8: The evolution of the (a) enthalpy and (b) collective variables (CVs) in the metadynamics simulation with 3456 atoms.

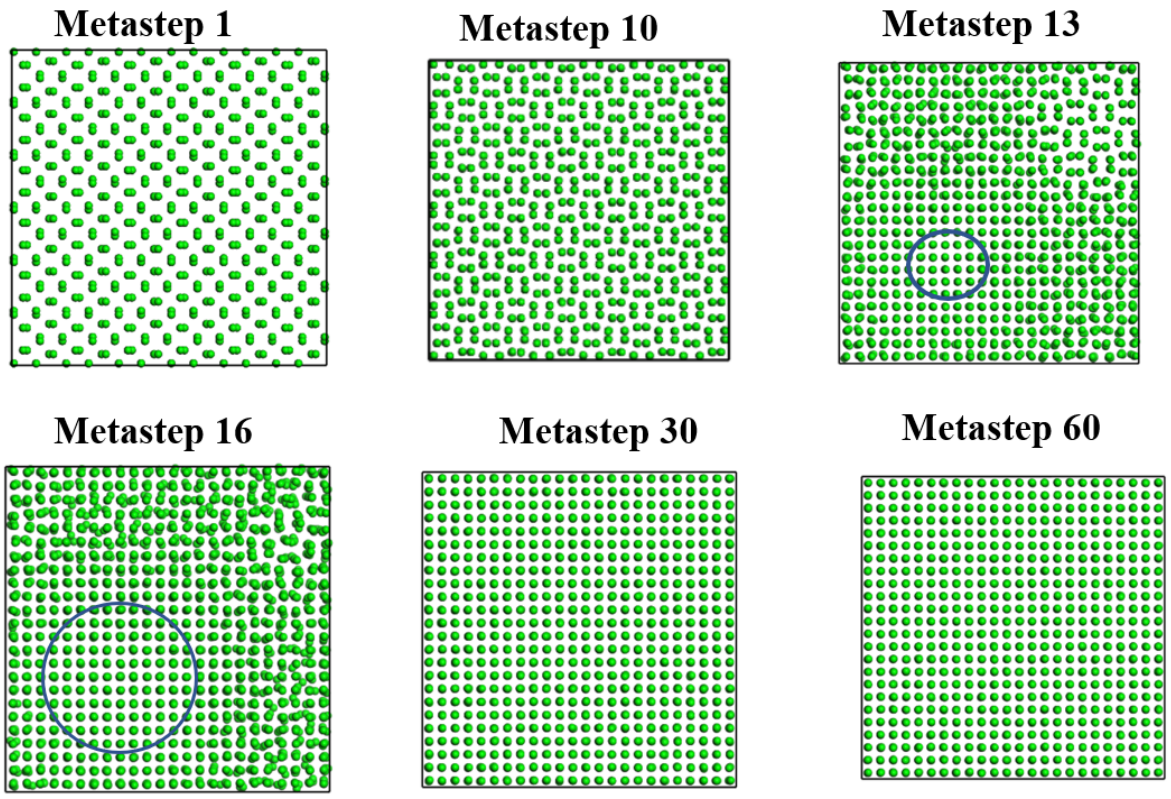

Figure 5.9: Snapshots from different metasteps in the metadynamics simulation performed with 3456 atoms.

questions one must find satisfactory answers to. For instance, how do one proceed when there are little or no database of reasonable structures for any system one intends to study? Can these machine learning potentials at one point begin to outperform the underlying potentials applied in their training? This field of research is till very young and new developments will surely come forth in coming years. Nevertheless, as this work demonstrates the significant improvements machine learning can bring to condensed matter systems and their absolute usefulness in this field, the future can only be exciting.

5.5 Conclusion

A machine learning potential was successfully created for sodium based on the Guassian process regression method and weighted atom-centered symmetry functions representation of the potential energy surface. Here, sodium potential energy surface was described using different relevant data sets that represent several regions in it with each data set consisting of three element groups which are total energies, interatomic forces, and stress tensors of the cell, which were constructed from density functional theory calculations. It was demonstrated that by learning from the underlying DFT results, the trained MLP was able to reproduce important properties of all available sodium phases with an exceptional accuracy in comparison to those computed using DFT. In combination with the metadynamics methods, this well trained MLP was applied to a large simulation boxes containing 1024 and 3456 sodium atoms in the cI16 phase. These large-scale simulations reveal a notable phase transition at 150 K and 120 GPa with an impressive capturing of the rearrangements of atomic configurations involved in the transition process that may not be evident in a small-scale simulation. Without a doubt, this work shows that applying machine learning methods to condensed matter systems will lead to significant increase in our understanding of important processes such as atomic rearrangements, growth and nucleation process in crystal formation and phase transition.

Chapter 6

CONCLUDING REMARKS

The objective of this work is to explore the properties of novel condensed matter materials with the use of first principles method and computer simulations. Structure properties, electronic properties, dynamical properties and bonding parameters of selected materials were investigated. The tools employed are based on density functional theory (DFT), density functional perturbation theory (DFPT) and projected augmented wave method.

Chapter 1 is discussion of the important fundamental theories behind the computational methods applied in all the calculations. A general review of what each chapter entails was also included with a brief highlight of the theoretical tools used.

Chapter 2 is about the detailed explanation of the theoretical mechanisms employed in crystal structure predictions such as random structure search, genetic algorithm, simulated annealing and metadynamics. Three published papers were used as examples to illustrate the application of these methods.

Chapter 3 presents the high enthalpy crystalline phases of cadmium telluride. The post-cmcm phase that had not been accurately identified for a long time was successfully characterized and predicted to also transform to a different phase at about 68 GPa. Enthalpy calculation results also supported these transition sequence. In addition, CdTe was shown to possess higher enthalpy than the addition of the enthalpies of its constituent elements above 34 GPa. Be that as it may, phonon calculations and experiments established its stability beyond this pressure point which therefore indicate that it is a high enthalpy material which is stabilized by a huge kinetic barrier.

Chapter 4 explored the possibility of helium forming a stable compound with hydrogen. A stable compound of these elements was predicted from first principle random search technique. It belongs to P-1 space group with atomic arrangements that emphasise the role of helium in stabilizing the structure. The result of topological analysis showed that there exists a quantifiable level of van der Waals interaction between helium and hydrogen in this $He(H_2)_3$ crystal at ambient pressure which is greatly enhanced with increasing compression.

Finally in Chapter 5, a machine learning potential was presented for sodium. This MLP was successfully created for sodium based on the Guassian process regressing (GPR) method and weighted atom-centered symmetry functions (wACSFs) representation of the potential energy surface (PES).Five different sets of data were used to represent various regions of the PES with each data consisting of total energies, interatomic forces and stress tensors of the cell which were all constructed from density functional theory (DFT) calculations. By learning from these data, the trained MLP was able to reproduce the properties such as energy, force, volume ans so on, for all tested sodium structures with accuracy similar to the underlying DFT method. Furthermore, in combination with the metadynamics methods, this well trained MLP was applied to a large simulation boxes containing 1024 and 3456 sodium atoms in the cI16 phase. These large-scale simulations reveal a notable phase transition at 150 K and 120 GPa with an impressive capturing of the rearrangements of atomic configurations involve in the transition process that may not be evident in a small-scale simulation. Without a doubt, this work shows that applying machine learning methods to condensed matter systems will lead to significant increase in our understanding of important processes such as atomic rearrangements, growth and nucleation process in crystal formation and phase transition.

Building on the research results of this thesis, there are numerous interesting future works that can be explored. For instance, the helium hydrogen system can be expanded to include helium-rich configurations so as to further explore the potential energy surface for insightful crystalline compounds. Other important planetary elements such as ammonia and ice at

extreme conditions typical of planetary bodies can also be investigated with the application of ab initio molecular dynamics and metadynamics. The results of such exploration can provide significant insight to the chemical processes that occur inside giant planets. In addition, the machine learning method can be implemented for different kinds of systems for a dependable simulations of solid-solid reconstructive phase transition.

References

[1] J.S. Tse. *Zeitschrift für Kristallographie-Crystalline Mat.*, 220:521, (2005).

[2] M. Born and R. Oppenheimer. *Annalen der physik*, 389:457, (1927).

[3] A. Bloch. In *Ann Fac Sci de Toulouse*, volume 17, page 1, (1925).

[4] P. Hohenberg and W. Kohn. *Phys. Rev.*, 136:B864, (1964).

[5] H. Hellmann. *J. Chem. Phys.*, 3:61, (1935).

[6] J.C. Phillips. *Phys. Rev.*, 112:685, (1958).

[7] J.C. Phillips and L. Kleinman. *Phys. Rev.*, 116:287, (1959).

[8] E. Schrödinger. *Phys. Rev.*, 28(6):1049, (1926).

[9] T. Helgaker, P. Jorgensen, and J. Olsen. *Molecular electronic-structure theory*. John Wiley & Sons, (2014).

[10] W. Kohn and L.J. Sham. *Phys. Rev.*, 140:A1133, (1965).

[11] J.P. Perdew, K. Burke, and M. Ernzerhof. *Phys. Rev. Lett.*, 77:3865, (1996).

[12] C. Kittel, P. McEuen, and P. McEuen. *Introduction to solid state physics*, volume 8. Wiley New York, (1996).

[13] R. Orlando, R. Dovesi, C. Roetti, and V.R. Saunders. *J. Phys.: Condens. Matter*, 2:7769, (1990).

[14] J.M. Soler, E. Artacho, J.D. Gale, A. García, J. Junquera, P. Ordejón, and D. Sánchez-Portal. *J. Phys.: Condens. Matter*, 14:2745, (2002).

[15] W.E. Pickett. *Comp. Phys. Reports*, 9:115, (1989).

[16] G. Kresse and D. Joubert. *Phys. Rev. B*, 59:1758, (1999).

[17] D.R. Hamann, M. Schlüter, and C. Chiang. *Phys. Rev. Lett.*, 43:1494, (1979).

[18] G.B. Bachelet, D.R. Hamann, and M. Schlüter. *Phys. Rev. B.*, 26:4199, (1982).

[19] D. Vanderbilt. *Phys. Rev. B*, 41:7892, (1990).

[20] P.E. Blöchl. *Phys. Rev. B*, 50:17953, (1994).

[21] G. Kresse and J. Hafner. *Phys. Rev. B*, 47:558, (1993).

[22] M. Dion, H. Rydberg, E. Schröder, D.C. Langreth, and B.I. Lundqvist. *Phys. Rev. Lett.*, 92:246401, (2004).

[23] O.A. Von Lilienfeld, I. Tavernelli, U. Rothlisberger, and D. Sebastiani. *Phys. Rev. Lett.*, 93:153004, (2004).

[24] A. Tkatchenko and M. Scheffler. *Phys. Rev. Lett.*, 102:073005, (2009).

[25] J. Klimeš, D.R. Bowler, and A. Michaelides. *J Phys.: Condens. Matter*, 22:022201, (2009).

[26] J. Klimeš, D.R. Bowler, and A. Michaelides. *Phys. Rev. B*, 83:195131, (2011).

[27] R.F.W. Bader. Oxford University Press. Oxford UK, (1990).

[28] R.F.W. Bader. *Chem. Rev.*, 91(5):893, (1991).

[29] C.F. Matta, R.J. Boyd, and A. Becke. Wiley-VCH. (2007).

[30] P.F. McMillan. *Nat. Mat.*, 4:715, (2005).

[31] R.J. Hemley. *High Pressure Research*, 30:581, (2010).

[32] L. Dubrovinsky, N. Dubrovinskaia, V.B. Prakapenka, and A.M. Abakumov. *Nat. Comm*, 3:1, (2012).

[33] L. Dubrovinsky, N. Dubrovinskaia, E. Bykova, M. Bykov, V. Prakapenka, C. Prescher, K. Glazyrin, H-P Liermann, M. Hanfland, M. Ekholm, et al. *Nature*, 525:226, (2015).

[34] C. Buzea and K. Robbie. *Super. Sci. and Tech.*, 18:R1, (2004).

[35] T. Matsuoka, M. Debessai, J.J. Hamlin, A.K. Gangopadhyay, J.S. Schilling, and K. Shimizu. *Phys. Rev. Lett.*, 100:197003, (2008).

[36] J. Lin, A.G. Gavriliuk, V.V. Struzhkin, S.D. Jacobsen, W. Sturhahn, M.Y. Hu, P. Chow, and C. Yoo. *Phys. Rev. B.*, 73:113107, (2006).

[37] J. Lin and T. Tsuchiya. *Phys. Earth and Planetary Interiors*, 170:248, (2008).

[38] H.G. Drickamer and C.W. Frank. *Electronic transitions and the high pressure chemistry and physics of solids*. Springer Science & Business Media, (2013).

[39] A.A. Adeleke, E. Stavrou, A.O. Adeniyi, B. Wan, H. Gou, and Y. Yao. *Phys. Rev. B*, 102(13):134120, (2020).

[40] H. Liu, I.I. Naumov, R. Hoffmann, N.W. Ashcroft, and R.J. Hemley. *Proceedings of the National Academy of Sciences*, 114:6990, (2017).

[41] F. Peng, Y. Yao, H. Liu, and Y. Ma. *J. Phys. Chem. Lett.*, 6:2363, (2015).

[42] Y. Shen, A.R. Oganov, G. Qian, J. Zhang, H. Dong, Q. Zhu, and Z. Zhou. *Scientific reports*, 5:1, (2015).

[43] X. Dong, A.R. Oganov, A.F. Goncharov, E. Stavrou, S. Lobanov, G. Saleh, G. Qian, Q. Zhu, C. Gatti, V.L. Deringer, et al. *Nat. Chem.*, 9:440, (2017).

[44] Z. M. Geballe, H. Liu, A. K. Mishra, M. Ahart, M. Somayazulu, Y. Meng, M. Baldini, and R. J. Hemley. *Angew. Chem. Int. Edit.*, 57:688, (2018).

[45] A.P. Drozdov, M.I. Eremets, I.A. Troyan, V. Ksenofontov, and S.I. Shylin. *Nature*, 525(7567):73, (2015).

[46] E. Snider, N. Dasenbrock-Gammon, R. McBride, M. Debessai, H. Vindana, K. Vencatasamy, K.V. Lawler, A. Salamat, and R.P. Dias. *Nature*, 586:373, (2020).

[47] L. Zhang, Y. Wang, J. Lv, and Y. Ma. *Nat. Rev. Mat.*, 2(4):1, (2017).

[48] W. Grochala, R. Hoffmann, J. Feng, and N.W. Ashcroft. *Angewandte Chemie International Edition*, 46:3620, (2007).

[49] C.T. Prewitt and R.T Downs. *Reviews in mineralogy*, 37:284, (1998).

[50] H. Liu, I.I. Naumov, R. Hoffmann, N.W. Ashcroft, and R.J. Hemley. *Proceedings of the National Academy of Sciences*, 114(27):6990, (2017).

[51] Y. Ma, M. Eremets, A.R. Oganov, Y. Xie, I. Trojan, S. Medvedev, A.O. Lyakhov, M. Valle, and V. Prakapenka. *Nature*, 458:182, (2009).

[52] M. Miao and R. Hoffmann. *Acc. Chem. Res.*, 47:1311, 2014.

[53] A.R. Oganov, C.J. Pickard, Q. Zhu, and R.J. Needs. *Nat. Rev. Mat.*, 4:331, (2019).

[54] M. Miao. *Nat. Chem.*, 5:846, (2013).

[55] J. Botana and M. Miao. *Nat. Commun.*, 5:1, (2014).

[56] M. Miao, Y. Sun, E. Zurek, and H. Lin. *Nat. Rev. Chem.*, 4:508, (2020).

[57] P. Giannozzi, S. Baroni, N. Bonini, M. Calandra, R. Car, C. Cavazzoni, D. Ceresoli, G. L. Chiarotti, M. Cococcioni, I. Dabo, A. Dal Corso, S. de Gironcoli, S. Fabris, G. Fratesi, R. Gebauer, U. Gerstmann, C. Gougoussis, A. Kokalj, M. Lazzeri, L. Martin-Samos, N. Marzari, F. Mauri, R. Mazzarello, S. Paolini, A. Pasquarello, L. Paulatto, C. Sbraccia, S. Scandolo, G. Sclauzero, A. P. Seitsonen, A. Smogunov, P. Umari, and R.M. Wentzcovitch. *J. Phys: Condens. Mat*, 21(39):395502, (2009).

[58] P. Giannozzi, O. Andreussi, T. Brumme, O. Bunau, M. Buongiorno Nardelli, M. Calandra, R. Car, C. Cavazzoni, D. Ceresoli, M. Cococcioni, N. Colonna, I. Carnimeo, A. Dal Corso, S. de Gironcoli, P. Delugas, R.A. DiStasio Jr, A. Ferretti, A. Floris, G. Fratesi, G. Fugallo, R. Gebauer, U. Gerstmann, F. Giustino, T. Gorni, J. Jia, M. Kawamura, H-Y Ko, A. Kokalj, E. Küçükbenli, M. Lazzeri, M. Marsili, N. Marzari, F. Mauri, N.L.

Nguyen, H-V Nguyen, A. Otero de-la Roza, L. Paulatto, S. Poncé, D. Rocca, R. Sabatini, B. Santra, M. Schlipf, A.P. Seitsonen, A. Smogunov, I. Timrov, T. Thonhauser, P. Umari, N. Vast, X. Wu, and S. Baroni. *J. Phys: Condens. Mat.*, 29:465901, (2017).

[59] A. Otero-de-la Roza, E.R. Johnson, and V. Luaña. *Comp. Phys. Comm.*, 185:1007, (2014).

[60] L. Kleinman and D.M. Bylander. *Phys. Rev. Lett.*, 48:1425, (1982).

[61] A. Togo and I. Tanaka. *Scr. Mater.*, 108:1–5, (2015).

[62] C. Mailhiot, L.H. Yang, and A.K. McMahan. *Phys. Rev. B*, 46:14419, (1992).

[63] A.R. Oganov. *Modern methods of crystal structure prediction.* John Wiley & Sons, 2011.

[64] V.A. Blatov and D.M Proserpio. *Modern methods of crystal structure prediction*, 1:1, (2011).

[65] E. Mooser and W.B. Pearson. *Acta Crystallographica*, 12:1015, (1959).

[66] J.K. Burdett, G.D Price, and S.L. Price. *Phys. Rev. B*, 24(6):2903, (1981).

[67] D.G Pettifor. *Solid State Commun.*, 51:31, (1984).

[68] R.L. Anderson. *J. Am. Stat. Asso.*, 48:789, 1953.

[69] L.A. Rastrigin. *Automaton & Remote Control*, 24:1337, (1963).

[70] C.J. Pickard and R.J. Needs. *Phys. Rev. Lett.*, 97:045504, (2006).

[71] C.W. Glass, A.R. Oganov, and N. Hansen. *Com. Phys. Commun.*, 175:713, (2006).

[72] Y. Wang, J. Lv, L. Zhu, and Y. Ma. *Phys. Rev. B.*, 82:094116, (2010).

[73] J.M. McMahon. *Phys. Rev. B*, 84:220104, (2011).

[74] J.M. McMahon and D.M. Ceperley. *Phys. Rev. Lett.*, 106:165302, (2011).

[75] C.J. Pickard and R.J. Needs. *J. Phys.: Condens. Matter*, 23:053201, (2011).

[76] Y. Yao, S.T. John, and K. Tanaka. *Phys. Rev. B*, 77:052103, (2008).

[77] J. Kennedy and R. Eberhart. Particle swarm optimization. In *Proceedings of ICNN'95-international conference on neural networks*, volume 4, page 1942. IEEE, (1995).

[78] R. Eberhart and J. Kennedy. A new optimizer using particle swarm theory. In *MHS'95. Proceedings of the Sixth International Symposium on Micro Machine and Human Science*, page 39. Ieee, (1995).

[79] A. Mujica and R.J. Needs. *Phys. Rev. B*, 55:9659, (1997).

[80] R. Martoňák, A. Laio, and M. Parrinello. *Phys. Rev. Lett.*, 90:075503, (2003).

[81] D.J. Wales and J.P.K Doye. *J. Phys. Chem. A*, 101:5111, (1997).

[82] S. Kirkpatrick, C.D. Gelatt, and M.P. Vecchi. *science*, 220:671, (1983).

[83] D.C. Karnopp. *Automatica*, 1:111, (1963).

[84] G. Csányi, C.J. Pickard, B.D. Simons, and R.J. Needs. *Phys. Rev. B*, 75:085432, (2007).

[85] C.J Pickard and R.J. Needs. *physica status solidi (b)*, 246:536, (2009).

[86] M.I. McMahon, R.J. Nelmes, N.G. Wright, and D.R. Allan. *Phys. Rev. B*, 48:15723, (1993).

[87] J.M. McMahon and D.M. Ceperley. *Phys. Rev. Lett.*, 106:165302, (2011).

[88] C.J. Pickard and R.J. Needs. *Phys. Rev. Lett.*, 97:045504, (2006).

[89] L.D. Lloyd and R.L. Johnston. *Chem. Phys.*, 236:107, (1998).

[90] C.J. Pickard and R.J. Needs. *J Phys. Condens. Matter*, 23:053201, (2011).

[91] C.J Pickard and R.J Needs. *J. Chem. Phys*, 127:244503, (2007).

[92] C.J. Pickard and R.J. Needs. *Phys. Rev. B*, 76:144114, (2007).

[93] C.J Pickard and R.J Needs. *J. Phys: Condens. Matter*, 21(45):452205, (2009).

[94] Y. Yao, J.S. Tse, and K. Tanaka. *Phys. Rev. B*, 77:052103, (2008).

[95] X. Dong, Oganov A.R., and A.F. Goncharov. *Nat. Chem.*, 9, (2017).

[96] R.C. Eberhart and Y. Shi. Comparing inertia weights and constriction factors in particle swarm optimization. In *Proceedings of the 2000 congress on evolutionary computation. CEC00 (Cat. No. 00TH8512)*, volume 1, page 84. IEEE, (2000).

[97] J.C. Schön and M. Jansen. *Angewandte Chemie International Edition in English*, 35:1286, (1996).

[98] R. Martoňák, A. Laio, and M. Parrinello. *Phys. Rev. Lett.*, 90:075503, (2003).

[99] R. Martoňák, D. Donadio, A.R. Oganov, and M. Parrinello. *Nat. Mat.*, 5:625, (2006).

[100] R. Martoňák, D. Donadio, A.R. Oganov, and M. Parrinello. *Phys. Rev. B*, 76:014120, (2007).

[101] M.P. Allen and D.J. Tildesley. Oxford Science Publ. Clarendon Press, (1989).

[102] D. Wales et al. *Energy landscapes: Applications to clusters, biomolecules and glasses.* Cambridge University Press, (2003).

[103] J.P.K. Doye and D.J. Wales. *J. Chem. Phys.*, 105:8428, (1996).

[104] J.P.K Doye and D.J Wales. *Phys. Rev. Lett.*, 80(7):1357, (1998).

[105] S.M. Woodley and R. Catlow. *Nat. Mat.*, 7:937, (2008).

[106] P.J.M Van Laarhoven and E.H.L. Aarts. Simulated annealing. In *Simulated annealing: Theory and applications*, page 7. Springer, (1987).

[107] N. Metropolis, A.W. Rosenbluth, M.N. Rosenbluth, A.H. Teller, and E. Teller. *J. Chem. Phys.*, 21:1087, (1953).

[108] J. Pellicer-Porres, D. Vazquez-Socorro, S. López-Moreno, A. Muñoz, P. Rodríguez-Hernández, D. Martínez-García, S. Achary, A.J.E. Rettie, and C.B. Mullins. *Phys. Rev. B*, 98:214109, (2018).

[109] X. Cheng, J. Guan, L. Jiang, H. Zhang, P. Wang, A.O. Adeniyi, Y. Yao, L. Su, and Y. Song. *Phys. Chem. Chem. Phys.*, 22(18):10238, (2020).

[110] S. Bandow, M. Takizawa, K. Hirahara, M. Yudasaka, and S. Iijima. *Chem. Phys. Lett.*, 337:48, (2001).

[111] Y. Iwasa, T. Arima, R.M. Fleming, T. Siegrist, O. Zhou, R.C. Haddon, L.J. Rothberg, K.B. Lyons, H.L. Carter, A.F. Hebard, et al. *Science*, 264:1570, (1994).

[112] Q. Huang, D. Yu, B. Xu, W. Hu, Y. Ma, Y. Wang, Z. Zhao, B. Wen, J. He, Z. Liu, et al. *Nature*, 510:250, (2014).

[113] R.S. Kumar, M.G. Pravica, A.L. Cornelius, M.F. Nicol, M.Y. Hu, and P.C. Chow. *Diamond and related materials*, 16:1250, (2007).

[114] S. Yamanaka, N.S. Kini, A. Kubo, S. Jida, and H. Kuramoto. *J. Am. Chem. Soc.*, 130:4303, (2008).

[115] M. Nunez-Regueiro, L. Marques, J.L. Hodeau, O. Béthoux, and M. Perroux. *Phys. Rev. Lett.*, 74:278, (1995).

[116] Y. Guo, L. Cui, D. Zhao, T. Song, X. Cui, and Z. Liu. *J. Phys.: Condens. Matter*, 32:165701, (2020).

[117] A.A. Adeleke, A.O. Adeniyi, H. Tang, H. Gou, and Y. Yao. *J Phys Condens Matter*, 32, (2020).

[118] V.L. Solozhenko, O.O. Kurakevych, D. Andrault, Y. Le Godec, and M. Mezouar. *Phys. Rev. Lett*, 102:015506, (2009).

[119] D. He, Y. Zhao, L. Daemen, J. Qian, T.D. Shen, and T.W. Zerda. *Appl. Phys. Lett.*, 81:643, (2002).

[120] A.G. Kvashnin, H.A. Zakaryan, C. Zhao, Y. Duan, Y.A. Kvashnina, C. Xie, H. Dong, and A.R. Oganov. *J. Phys. Chem. Lett.*, 9:3470, (2018).

[121] L.J. Parker, T. Atou, and J.V. Badding. *Science*, 273:95, (1996).

[122] A.R. Miedema, P.F. De Chatel, and F.R. De Boer. *Physica B+ c*, 100:1, (1980).

[123] G. Kresse and D. Joubert. *Phys. Rev. B*, 59:1758, (1999).

[124] J.P. Perdew, K. Burke, and M. Ernzerhof. *Phys. Rev. Lett.*, 77:3865, (1996).

[125] Y. Yan, S. Zhang, Y. Wang, G. Yang, and Y. Ma. *RSC Adv.*, 5:104426, (2015).

[126] B. Manjeet, K. Md. Shahzad, and S. Anurag. *AIP Conference Proceedings*, 1953:040033, (2018).

[127] R.J. Nelmes, M.I. McMahon, N.G. Wright, and D.R. Allan. *Phys. Rev. B*, 51:15723, (1995).

[128] T. Huang and A.L. Ruoff. *Phys. Rev. B*, 31:5976, (1985).

[129] J. Mei and J. Lemos. *Soldi State Commun.*, 52, (1984).

[130] A.N. Chantis, van S.M., and T. Kotani. *Phys. Rev. Lett.*, 96:086405, (2006).

[131] E. Ahlswede R. Wuerz C. D.Wessendorf M. Powalla, S. Paetel and T. Magorian Friedlmeier. *App. Phy. Rev.*, 5, (2018).

[132] R. Weil, R. Nkum, E. Muranevich, and L. Benguigui. *Phys. Rev. Lett.*, 62:2744, (1989).

[133] Y. Pei, A.D LaLonde, N.A Heinz, and G.J Snyder. *Adv. Energy Mater*, 2, (2012).

[134] S.M. Reimann and M. Manninen. *Rev. Mod. Phys.*, 74, (2002).

[135] R.J. Nelmes, M.I. McMahon, N.G. Wright, and D.R. Allan. *J. Phys. Chem. Solids*, 56:545, (1995).

[136] Y. Yan, S. Zhang, Y. Wang, G. Yang, and Y. Ma. *RSC advances*, 5:104426, (2015).

[137] S. Biering and P. Schwerdtfeger. *J. Chem. Phys.*, 136:034504, (2012).

[138] A.O. Adeniyi, M. Kunz, E. Stavrou, and Y. Yao. *Phys. Rev. Res.*, 2:033072, (2020).

[139] R. Ahuja, P. James, O. Eriksson, J.M. Wills, and B. Johansson. *physica status solidi (b)*, 199:75, (1997).

[140] Z. Li, H. Wang, Y. Li, Y. Ma, T. Cui, and G. Zou. *New Journal of Physics*, 12:043058, (2010).

[141] R.J. Nelmes and M.I. McMahon. *Semiconductors and semimetals*, 54:145, (1998).

[142] T. Kenichi. *Phys. Rev. B*, 56:5170, (1997).

[143] G. Parthasarathy and W.B. Holzapfel. *Phys. Rev. B*, 37:8499, (1988).

[144] P. Loubeyre, M. Jean-Louis, R. LeToullec, and L. Charon-Gérard. *Phys. Rev. Lett.*, 70:178, (1993).

[145] C. Cazorla and D. Errandonea. *Phys. Rev. B*, 81:104108, (2010).

[146] S.B. David and J.S. Gary. *J. Am. Chem. Soc.*, 133, (2011).

[147] W.W. Ming. *J. Am. Chem. Soc.*, 122, (2000).

[148] C. J. Pickard G. Zou L. Zhu, H. Liu and Y. Ma. *Nat. Chem.*, 6, (2014).

[149] H. Gao, J. Sun, C.J. Pickard, and R.J. Needs. *Phys. Rev. Mat.*, 3:015002, (2019).

[150] J. Zhang, J. Lv, H. Li, X. Feng, C. Lu, S.A.T. Redfern, H. Liu, C. Chen, and Y. Ma. *Phys. Rev. Lett.*, 121:255703, (2018).

[151] Liu Z. Botana J. et al. Bai, Y. *Commun Chem*, 2, (2019).

[152] W.L. Vos, L.W. Finger, R.J. Hemley, J.Z. Hu, H.K. Mao, and J.A. Schouten. *Nat. (Lon)*, 365, (1992).

[153] J.J. Fortney. *Science*, 305(5689):1414, (2004).

[154] J.M. McMahon, M.A. Morales, C. Pierleoni, and D.M. Ceperley. *Rev. Mod. Phys.*, 84:1607, (2012).

[155] I. Baraffe, G. Chabrier, and T. Barman. *Rep. Prog. Phys.*, 73, (2010).

[156] J.J. Fortney and W.B. Hubbard. *Icarus*, 164:228, (2003).

[157] R. Smoluchowski. *Rep. Prog. Phys.*, 215, (1967).

[158] W.B. Hubbard, T. Guillot, M.S. Marley, A. Burrows, J.I. Lunine, and D.S. Saumon. *Planetary and Space Science*, 47:1175, (1999).

[159] J.J. Fortney and W.B. Hubbard. *Icarus*, (2003).

[160] N.W. Ashcroft. *Phys. Rev. Lett.*, 21:1748, (1968).

[161] P. Cudazzo, G. Profeta, A. Sanna, A. Floris, A. Continenza, S. Massidda, and E. K.U. Gross. *Phys. Rev. Lett.*, 100:257001, (2008).

[162] J.M. McMahon and D.M. Ceperley. *Phys. Rev. B*, 85:219902, (2012).

[163] A. Majumdar, J.S. Tse, M. Wu, and Y. Yao. *Phys. Rev. B*, 96:201107, (2017).

[164] H. Liu J.S. Tse Y. Wang Y. Li, J. Hao and Y. Ma. *Sci Rep*, 5, (2015).

[165] H. Wang, J.S. Tse, K. Tanaka, T. Iitaka, and Y. Ma. *Proceedings of the National Academy of Sciences*, 109:6463, (2012).

[166] I.A. Troyan V. Ksenofontov P. Drozdov, M.I. Eremets and S.I. Shylin. *Nature Phys*, 525, (2015).

[167] J. Vorberger, I. Tamblyn, B. Militzer, and S.A. Bonev. *Phys. Rev. B*, 75:024206, (2007).

[168] J. Lim, M. Kim, S. Duwal, S. Kawaguchi, Y. Ohishi, H. Liermann, R. Hrubiak, J.S. Tse, and C. Yoo. *Phys. Rev. B*, 101:224103, (2020).

[169] M.A. Morales, S. Hamel, K. Caspersen, and E. Schwegler. *Phys. Rev. B*, 87:174105, (2013).

[170] W. Lorenzen, B. Holst, and R. Redmer. *Phys. Rev. Lett.*, 102:115701, (2009).

[171] M. Schöttler and R. Redmer. *Phys. Rev. Lett*, 120:115703, 2018.

[172] P. Teeratchanan and A. Hermann. *J. Chem. Phys.*, 143:154507, (2015).

[173] J. Lim and C. Yoo. *Phys. Rev. Lett.*, 120(16):165301, (2018).

[174] R. Turnbull, M. Donnelly, M. Wang, M. Peña-Alvarez, C. Ji, P. Dalladay-Simpson, H. Mao, E. Gregoryanz, and R.T. Howie. *Phys. Rev. Lett.*, 121:195702, (2018).

[175] D. Londono, J.L. Finney, and W.F. Kuhs. *J. Chem. Phys.*, 97(1):547, (1992).

[176] K. Lee, É.D. Murray, L. Kong, B.I. Lundqvist, and D.C. Langreth. *Phys. Rev. B*, 82:081101, (2010).

[177] S. Ehrlich S. Grimme, J. Antony and S. Krieg. *J. Chem. Phys.*, 132, (2010).

[178] U. Koch and P.L.A. Popelier. *J. Phys. Chem.*, 99, (1995).

[179] C. Pickard and R. Needs. *Nature Phys*, 3, (2007).

[180] A.O. Adeniyi, A.A. Adeleke, X. Li, H. Liu, and Y. Yao. *Phys. Rev. B*, 104:024101, (2021).

[181] H. Margenau. *Reviews of Modern Physics*, 11:1, 1939.

[182] J.N. John. https://www.chem.purdue.edu/gchelp/vibs/help.html.

[183] Y. Yao, X. Yong, J.S. Tse, and M.J. Greschner. *J. Phys. Chem. C*, 118(51):29591, (2014).

[184] H. Liu, Y. Yao, and D.D. Klug. *Phys. Rev. B*, 91:014102, (2015).

[185] Z. Liu, J. Botana, A. Hermann, S. Valdez, E. Zurek, D. Yan, H. Lin, and M. Miao. *Nat. Commun.*, 9:1, (2018).

[186] I. Errea, M. Calandra, C.J. Pickard, J. Nelson, R.J Needs, Y. Li, H. Liu, Y. Zhang, Y. Ma, and F. Mauri. *Phys. Rev. Lett.*, 114:157004, (2015).

[187] J. Bardeen. *J. Chem. Phys.*, 6:372, (1938).

[188] M. Hanfland, I. Loa, and K. Syassen. *Phys. Rev. B.*, 65:184109, (2002).

[189] M. Hanfland, K. Syassen, N.E. Christensen, and D.L. Novikov. *Nature*, 408:174, (2000).

[190] M.I. McMahon, S. Rekhi, and R.J. Nelmes. *Phys. Rev. Lett.*, 87:055501, (2001).

[191] U. Schwarz, A. Grzechnik, K. Syassen, I. Loa, and M. Hanfland. *Phys. Rev. Lett.*, 83:4085, (1999).

[192] E. Gregoryanz, O. Degtyareva, M. Somayazulu, R.J. Hemley, and H. Mao. *Phys. Rev. Lett.*, 94(18):185502, (2005).

[193] E. Gregoryanz, L.F. Lundegaard, M. I. McMahon, C. Guillaume, R.J. Nelmes, and M. Mezouar. *Science*, 320:1054, (2008).

[194] J.B. Neaton and N.W. Ashcroft. *Phys. Rev. Lett.*, 86:2830, (2001).

[195] N.E. Christensen and D.L. Novikov. *Solid State Commun.*, 119:477, (2001).

[196] Y. Ma, M. Eremets, A.R. Oganov, Y. Xie, I. Trojan, S. Medvedev, A.O. Lyakhov, M. Valle, and V. Prakapenka. *Nature*, 458:182, (2009).

[197] R. Berliner, H.G. Smith, J.R.D. Copley, and J. Trivisonno. *Phys. Rev. B*, 46:14436, (1992).

[198] W. Schwarz, O. Blaschko, and I. Gorgas. *Phys. Rev. B*, 46:14448, (1992).

[199] M.I. McMahon, E. Gregoryanz, L.F. Lundegaard, I. Loa, C. Guillaume, R.J. Nelmes, A.K. Kleppe, M. Amboage, H. Wilhelm, and A.P. Jephcoat. *Proceedings of the National Academy of Sciences*, 104:17297, (2007).

[200] J. Raty, E. Schwegler, and S.A. Bonev. *Nature*, 449:448, (2007).

[201] D. Zahn and S. Leoni. *Phys. Rev. Lett.*, 92:250201, (2004).

[202] R.Z. Khaliullin, H. Eshet, T.D. Kühne, J. Behler, and M. Parrinello. *Nat. Mat.*, 10:693, (2011).

[203] L.F. Magana and G.J. Vazquez. *J. Phys.: Condens. Matter*, 2:4807, (1990).

[204] P.S. Ho. *Phys. Rev. B*, 3:4035, (1971).

[205] A.M. Guellil and J.B. Adams. *J. Mat. Res.*, 7:639, (1992).

[206] S. Chantasiriwan and F. Milstein. *Phys. Rev. B.*, 53:14080, (1996).

[207] J. Behler and M. Parrinello. *Phys. Rev. Lett.*, 98:146401, (2007).

[208] J. Behler. *J. Phys.: Condens. Matter*, 26:183001, (2014).

[209] J. Behler. *International Journal of Quantum Chemistry*, 115:1032, (2015).

[210] A.P. Bartók, M.C. Payne, R. Kondor, and G. Csányi. *Phys. Rev. Lett.*, 104:136403, (2010).

[211] V.L. Deringer and G. Csányi. *Phys. Rev. B*, 95:094203, (2017).

[212] Z. Li, J.R. Kermode, and A. De Vita. *Phys. Rev. Lett.*, 114:096405, (2015).

[213] R.M. Balabin and E.I. Lomakina. *Phys. Chem. Chem. Phys.*, 13:11710, (2011).

[214] V. Botu, R. Batra, J. Chapman, and R. Ramprasad. *J. Phys. Chem. C*, 121:511, (2017).

[215] T.L. Jacobsen, M.S. Jørgensen, and B. Hammer. *Phys. Rev. Lett.*, 120:026102, (2018).

[216] J. Behler. *J. Chem. Phys.*, 145:170901, (2016).

[217] Q. Tong, L. Xue, J. Lv, Y. Wang, and Y. Ma. *Faraday discussions*, 211:31, (2018).

[218] H. Gao, J. Wang, and J. Sun. *J. Chem. Phys.*, 150:244110, (2019).

[219] Y. Zuo, C. Chen, X. Li, Z. Deng, Y. Chen, J. Behler, G. Csányi, A.V. Shapeev, A.P. Thompson, M.A. Wood, et al. *J. Phys. Chem. A*, 124:731, (2020).

[220] Q. Tong, P. Gao, H. Liu, Y. Xie, J. Lv, Y. Wang, and J. Zhao. *J. Phys. Chem. Lett.*, 11:8710, (2020).

[221] L. Bonati and M. Parrinello. *Phys. Rev. Lett.*, 121:265701, (2018).

[222] H. Niu, L. Bonati, P.M. Piaggi, and M. Parrinello. *Nat. Commun.*, 11:1, (2020).

[223] H. Eshet, R.Z. Khaliullin, T.D. Kühne, J. Behler, and M. Parrinello. *Phys. Rev. Lett*, 108:115701, (2012).

[224] J. Behler. *J. Chem. Phys.*, 134:074106, (2011).

[225] A.P. Bartók, R. Kondor, and G. Csányi. *Phys. Rev. B*, 87:184115, (2013).

[226] J. Behler. *Angewandte Chemie International Edition*, 56:12828, (2017).

[227] M. Gastegger, L. Schwiedrzik, M. Bittermann, F. Berzsenyi, and P. Marquetand. *J. Chem. Phys.*, 148:241709, (2018).

[228] Q. Tong, X. Luo, A.A. Adeleke, P. Gao, Y. Xie, H. Liu, Q. Li, Y. Wang, J. Lv, Y. Yao, et al. *Phys. Rev. B*, 103:054107, (2021).

[229] A.H. Larsen, J.J. Mortensen, J. Blomqvist, I.E. Castelli, R. Christensen, M. Dułak, J. Friis, M.N. Groves, B. Hammer, C. Hargus, et al. *J. Phys.: Condens. Matter*, 29:273002, (2017).

Appendix A

To further establish the theoretical computation performed in chapter 3, the enthalpy of the $He(H_2)_3$ was also compared with that of HCP He and HCP hydrogen in the pressure range of interest as shown in Figure A.1. A comparison of the enthalpies for HCP hydrogen and the employed hexagonal $P6_3/m$ structure indicates that the $P6_3/m$ is favoured in our pressure range of interest. (See Figure A.2)

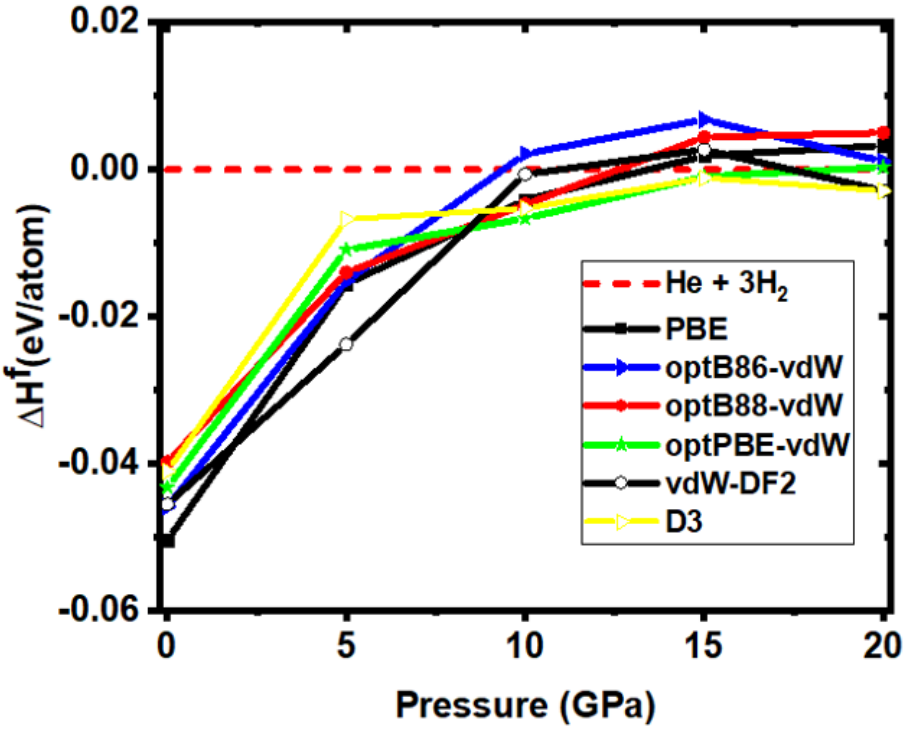

Figure A.1: Formation enthalpy of the P-1 structure with respect to the hcp He and hcp hydrogen computed with PBE potential and then with optPBE-vdW, optB86-vdW, optB88-vdW, D3 and vdW-D2 functionals

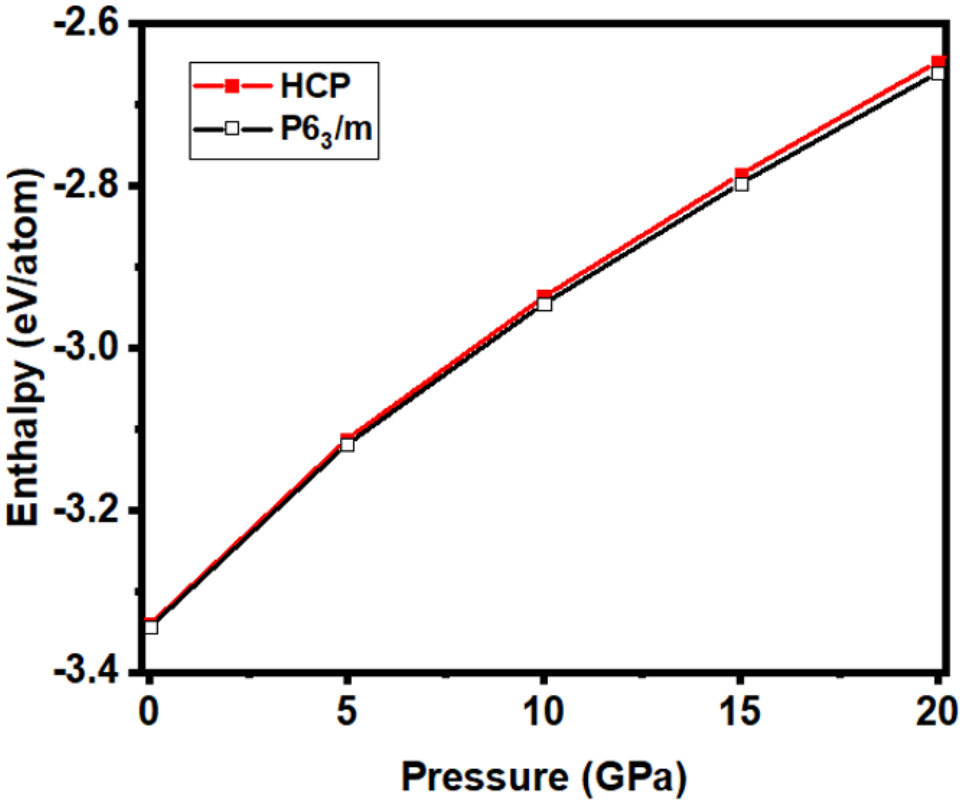

Figure A.2: Comparison of the enthalpy for $P6_3/m$ and hcp hydrogen structures

Appendix B

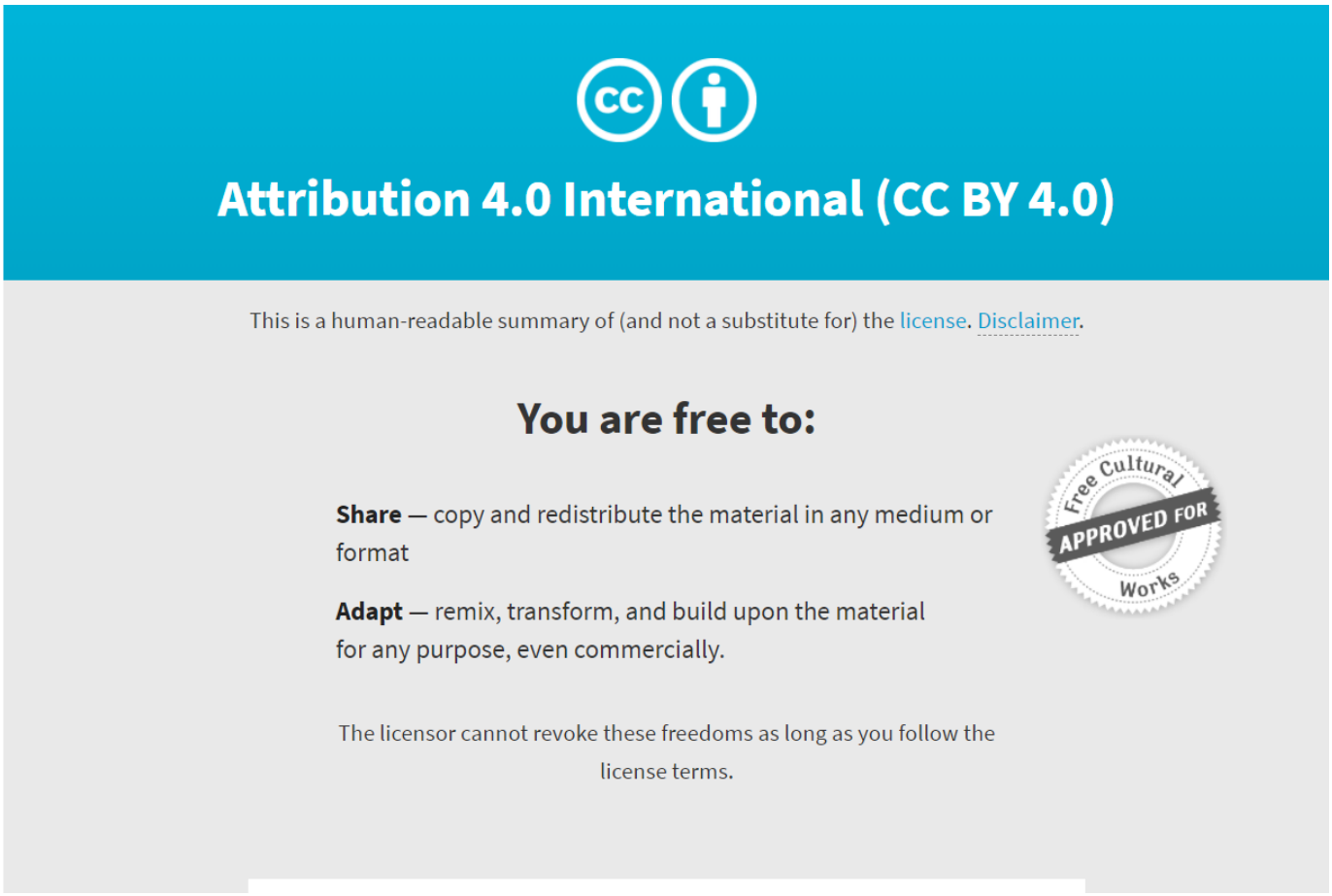

Attribution 4.0 International (CC BY 4.0)

This is a human-readable summary of (and not a substitute for) the license. Disclaimer.

You are free to:

Share — copy and redistribute the material in any medium or format

Adapt — remix, transform, and build upon the material for any purpose, even commercially.

The licensor cannot revoke these freedoms as long as you follow the license terms.

American Physical Society Reuse and Permissions License

14-Jul-2021

This license agreement between the American Physical Society ("APS") and Adebayo Adeniyi ("You") consists of your license details and the terms and conditions provided by the American Physical Society and SciPris.

Licensed Content Information

License Number:	**RNP/21/JUL/042241**
License date:	14-Jul-2021
DOI:	10.1103/PhysRevB.104.024101
Title:	Prediction of a stable helium-hydrogen compound: First-principles simulations
Author:	Adebayo O. Adeniyi et al.
Publication:	Physical Review B
Publisher:	American Physical Society
Cost:	USD $ 0.00

Request Details

Does your reuse require significant modifications: No

Specify intended distribution locations:	United States,Canada
Reuse Category:	Reuse in a thesis/dissertation
Requestor Type:	Student
Items for Reuse:	Figures/Tables
Number of Figure/Tables:	1
Figure/Tables Details:	Fig 4
Format for Reuse:	Electronic

Information about New Publication:

University/Publisher:	Student
Title of dissertation/thesis:	First Principles Investigations of Novel Materials
Author(s):	Adebayo Adeniyi
Expected completion date:	Aug. 2021

License Requestor Information

Name:	Adebayo Adeniyi
Affiliation:	Individual
Email Id:	aadeniyi@aust.edu.ng
Country:	Canada

American Physical Society Reuse and Permissions License

TERMS AND CONDITIONS

The American Physical Society (APS) is pleased to grant the Requestor of this license a non-exclusive, non-transferable permission, limited to Electronic format, provided all criteria outlined below are followed.

1. You must also obtain permission from at least one of the lead authors for each separate work, if you haven't done so already. The author's name and affiliation can be found on the first page of the published Article.
2. For electronic format permissions, Requestor agrees to provide a hyperlink from the reprinted APS material using the source material's DOI on the web page where the work appears. The hyperlink should use the standard DOI resolution URL, http://dx.doi.org/{DOI}. The hyperlink may be embedded in the copyright credit line.
3. For print format permissions, Requestor agrees to print the required copyright credit line on the first page where the material appears: "Reprinted (abstract/excerpt/figure) with permission from [(FULL REFERENCE CITATION) as follows: Author's Names, APS Journal Title, Volume Number, Page Number and Year of Publication.] Copyright (YEAR) by the American Physical Society."
4. Permission granted in this license is for a one-time use and does not include permission for any future editions, updates, databases, formats or other matters. Permission must be sought for any additional use.
5. Use of the material does not and must not imply any endorsement by APS.
6. APS does not imply, purport or intend to grant permission to reuse materials to which it does not hold copyright. It is the requestor's sole responsibility to ensure the licensed material is original to APS and does not contain the copyright of another entity, and that the copyright notice of the figure, photograph, cover or table does not indicate it was reprinted by APS with permission from another source.
7. The permission granted herein is personal to the Requestor for the use specified and is not transferable or assignable without express written permission of APS. This license may not be amended except in writing by APS.
8. You may not alter, edit or modify the material in any manner.
9. You may translate the materials only when translation rights have been granted.
10. APS is not responsible for any errors or omissions due to translation.
11. You may not use the material for promotional, sales, advertising or marketing purposes.
12. The foregoing license shall not take effect unless and until APS or its agent, Aptara, receives payment in full in accordance with Aptara Billing and Payment Terms and Conditions, which are incorporated herein by reference.
13. Should the terms of this license be violated at any time, APS or Aptara may revoke the license with no refund to you and seek relief to the fullest extent of the laws of the USA. Official written notice will be made using the contact information provided with the permission request. Failure to receive such notice will not nullify revocation of the permission.
14. APS reserves all rights not specifically granted herein.
15. This document, including the Aptara Billing and Payment Terms and Conditions, shall be the entire agreement between the parties relating to the subject matter hereof.

American Physical Society Reuse and Permissions License

14-Jul-2021

This license agreement between the American Physical Society ("APS") and Adebayo Adeniyi ("You") consists of your license details and the terms and conditions provided by the American Physical Society and SciPris.

Licensed Content Information

License Number:	**RNP/21/JUL/042242**
License date:	14-Jul-2021
DOI:	10.1103/PhysRevB.102.134120
Title:	Two good metals make a semiconductor: A potassium-nickel compound under pressure
Author:	Adebayo A. Adeleke et al.
Publication:	Physical Review B
Publisher:	American Physical Society
Cost:	USD $ 0.00

Request Details

Does your reuse require significant modifications: No

Specify intended distribution locations:	United States,Canada
Reuse Category:	Reuse in a thesis/dissertation
Requestor Type:	Student
Items for Reuse:	Figures/Tables
Number of Figure/Tables:	1
Figure/Tables Details:	Figure 1
Format for Reuse:	Electronic

Information about New Publication:

University/Publisher:	Student
Title of dissertation/thesis:	First Principles Investigations of Novel Materials
Author(s):	ADEBAYO ADENIYI
Expected completion date:	Aug. 2021

License Requestor Information

Name:	Adebayo Adeniyi
Affiliation:	Individual
Email Id:	aadeniyi@aust.edu.ng
Country:	Canada

CCC | Marketplace™

Order Number: 1133134
Order Date: 14 Jul 2021

Payment Information

Adebayo Adeniyi
aadeniyi@aust.edu.ng
Payment method: Invoice

Billing Address:
Mr. Adebayo Adeniyi
Student
1016 Temperance St
Saskatoon, SK S7N 0N6
Canada

+1 (306) 261-1567
aadeniyi@aust.edu.ng

Customer Location:
Mr. Adebayo Adeniyi
Student
1016 Temperance St
Saskatoon, SK S7N 0N6
Canada

Order Details

1. Journal of Physics : Condensed Matter

Billing Status: Open

Order License ID	1133134-1
Order detail status	Completed
ISSN	0953-8984
Type of use	Republish in a thesis/dissertation
Publisher	IOP Publishing
Portion	Image/photo/illustration

0.00 CAD
Republication Permission

LICENSED CONTENT

CCC Marketplace™

This is a License Agreement between ADEBAYO ADENIYI ("User") and Copyright Clearance Center, Inc. ("CCC") on behalf of the Rightsholder identified in the order details below. The license consists of the order details, the CCC Terms and Conditions below, and any Rightsholder Terms and Conditions which are included below.

All payments must be made in full to CCC in accordance with the CCC Terms and Conditions below.

Order Date	14-Jul-2021	**Type of Use**	Republish in a thesis/dissertation
Order License ID	1133142-1	**Publisher**	ROYAL SOCIETY OF CHEMISTRY
ISSN	1463-9076	**Portion**	Chart/graph/table/figure

LICENSED CONTENT

Publication Title	Physical chemistry chemical physics : PCCP	**Rightsholder**	Royal Society of Chemistry
Article Title	Pressure-induced structural transformations and new polymorphs in BiVO4.	**Publication Type**	Journal
		Start Page	10238
		End Page	10246
Author/Editor	Royal Society of Chemistry (Great Britain), Deutsche Bunsen-Gesellschaft für Physikalische Chemie., Koninklijke Nederlandse Chemische Vereniging., Società chimica italiana.	**Issue**	18
		Volume	22
Date	12/31/1998		
Language	English		
Country	United Kingdom of Great Britain and Northern Ireland		

REQUEST DETAILS

Portion Type	Chart/graph/table/figure	**Distribution**	Canada
Number of charts / graphs / tables / figures requested	1	**Translation**	Original language of publication
		Copies for the disabled?	No
Format (select all that apply)	Electronic	**Minor editing privileges?**	No
Who will republish the content?	Academic institution	**Incidental promotional use?**	No
Duration of Use	Current edition and up to 5 years	**Currency**	CAD
Lifetime Unit Quantity	Up to 499		
Rights Requested	Main product		